THE GEODESY OF THE MAIN SATURNIAN SATELLITES

Author:

Marco Ducci

Advisor:

Prof. Luciano Iess

Acknowledgments

Table of Contents

List of Figures

List of Tables

Introduction

Before the advent of telescopes in the XVII century nothing was known about the Saturn system apart from the presence of the planet itself. Galileo first observed Saturn's rings but he thought they were two moons orbiting the planet. The main satellites of Saturn were later discovered by Christian Huygens and Giovanni Domenico Cassini who respectively observed Titan and the other moons Iapetus, Rhea, Tethys and Dione. Since then the knowledge of the Saturn system structure and dynamics improved and new questions rose about the internal structure and composition of Saturn's main satellites. The observations made by the NASA probes Pioneer 11 and Voyager 1 and 2 brought the first close images of Saturn and most of its satellites demonstrating the complexity of the Saturn's world.

The arrival of Cassini-Huygens mission in the Saturn system in 2004 marked the beginning of an extensive period of observations that helped in answering questions about the dynamics and structure of Saturn and its main satellites. In this context radio science observations played a crucial role providing fundamental information about the structure and composition of Saturn's rings, its atmosphere and ionosphere and the gravity fields of Saturn and its main satellites.

The determination of the gravity field of the main satellites of Saturn relies on the analysis of the accelerations induced on Cassini as it flies by the selected body. These velocity variations can be detected thanks to a state-of-the-art instrumentation on board, that can provide range-rate data accurate up to 12 μ/s at 60 s integration time under favorable geometric conditions. Although Cassini performed more than 80 flybys of Saturn's major moon Titan and several flybys of the other moons, mainly Enceladus, Rhea and Dione, only a small number of them were devoted to gravity science. This limitation was due to the lack of a scan platform for optical remote sensing instruments that prevented simultaneous gravity and remote sensing observations. In fact, radio science observations requires Cassini High Gain Antenna to be precisely pointed towards the Earth at all times.

From July 2004 to December 2011 Cassini performed six flybys of Titan, three of Enceladus and one of Rhea and Dione dedicated to gravity science. The analysis of the data acquired during these close flybys allowed the first determination of the quadrupole gravity fields of Titan, Rhea, Dione and Enceladus. For Titan and Enceladus, the only Saturn's moons that have been visited more than once for gravity investigations, it was also possible to estimate the degree-3 harmonics. All the information collected were then used to constraint the internal structure and derive models of evolution and composition of these bodies. The work presented in this thesis is focused on the analysis of Cassini tracking data for the determination of the gravity field of Titan, Enceladus and Dione.

Titan is Saturn's largest moon and hosts a variety of peculiar features such as dune fields, hydrocarbon lakes and a dense atmosphere. The latter prevents the optical instruments to directly probe the surface of the satellite which is accessible only through radar observations. These observations have revealed the presence of a complex topography which may be the indication of endogenic processes active in Titan's interior. The first determinations of Titan's gravity field (Iess et al., 2010) and rotational state (Stiles et al., 2008) were used to infer the axial Moment of Inertia (MOI). The strong disagreement between the MOI values, determined in these two analyses, is an indication that Titan's interior is somehow decoupled from the surface crust. To confirm this hypothesis it was crucial to determine the tidal deformations of Titan. The estimate of the tidal Love number k_2 can give an indication of how the mass redistribute in Titan's interior in response to the forcing potential exerted by Saturn which varies along the orbit due to a non-negligible eccentricity. By combining data from the six Titan gravity flybys completed so far we determined the Love number with a 10% relative accuracy (Iess et al., 2012). The large estimated value is consistent with the presence of a global ocean under the surface of the satellite.

Enceladus is instead one of the smallest satellites of Saturn but it is one of the most intriguing objects in the Saturn system as well. The discovery of active resurfacing processes at the South Pole (Porco et al., 2006) made the determination of Enceladus' gravity an important objective of the Cassini mission extensions that started in 2008. The two dedicated gravity flybys of April and November 2010 allowed to infer the presence of a gravity anomaly (a negative J_3) at the South Pole. The analysis carried out in this thesis contributed to this result which is consistent with the presence of a subsurface concentration of liquid water at the South Pole that can be the source of the active geysers observed by Cassini.

The determination of Dione's gravity field was instead crucial to complete the characterization of the internal structures of the main Saturnian satellites. Data acquired during the gravity flyby of December 2011 were used to determine for the first time Dione's quadrupole gravity field. A single flyby with tracking at closest approach does not allow an independent measurement of J_2 and C_{22} and in order to infer the Moment of Inertia Factor the hydrostatic equilibrium hypothesis has to be made. Despite these limitations, data from the only Dione's flyby dedicated to gravity have demonstrated that it is a differentiated body. The exact degree of differentiation and the composition of the different layers cannot be assessed with the available data but an important constraint has been derived anyway.

The work is organized as follows: Chapter 1 presents an overview of the Cassini mission with particular focus on the Radio Science instrumentation and describes the current knowledge of the main satellites of Saturn whose gravity was analyzed in this work. Chapter 2 reviews the basic concepts of planetary geodesy and all the geophysical models used in the analysis. Chapter 3 is dedicated to the description of the mathematical formulation of the orbit determination problem. It includes a detailed description of the approach used and the data on which the analysis is based. Chapter 4 describes with more details the general characteristics of the analysis methods used to derive the geodesy of the main Saturnian satellites and includes the description of the dynamical model and all the key points of the analysis. Chapter 5 reports the results of the data analysis process with possible interpretations. Finally, Chapter 6 gives conclusions and future work perspectives.

Chapter 1

Cassini-Huygens unveils Saturn's system

The Cassini-Huygens mission is probably the most ambitious project ever attempted in the history of space exploration. Named after both the Italian-French astronomer Giovanni Domenico Cassini (1625-1712) and the Dutch scientist, discoverer of the moon Titan, Christiaan Huygens (1629 - 1695), it was conceived in the early eighties as a joint mission between NASA and ESA. After a seven-years tour begun on 15 October 1997 the spacecraft reached the Saturn system. Since then, during the 4 years nominal mission and the following solstice and equinox extended phases, Cassini-Huygens has unveiled hundreds of Saturn mysteries shining a new light on fundamental questions about the development of planetary systems as well as the entire Solar System.

This chapter is organized as follows: section 1 gives an overview of the Cassini-Hyugens mission. Sections 2, 3 and 4 are dedicated to the main satellite of Saturn and describe their main physical characteristics as well as the improvements brought by Cassini observations to a more complete knowledge of their composition and evolution. Section 4 describes with more detail the radio science instrumentation used for gravity analyses.

1.1   Cassini mission

Cassini-Huygens was lunched on October 15, 1997 from Cape Canaveral with a Titan IV-B Centaur rocket. During its seven years cruise to Saturn, four gravity assists were employed to increase the spacecraft velocity and allow reaching Saturn.

They included two Venus flybys (26 April 1998 and 24 June 1999), an Earth flyby (18 August 1999) and a Jupiter flyby (30 December 2000). The 627 m/s SOI (Saturn Orbit Insertion) maneuver of July 1, 2004 marked the beginning of the tour phase that was scheduled to last for four years. The exceptional results obtained during these four years granted Cassini two further mission extensions that should carry the mission up to 2017.
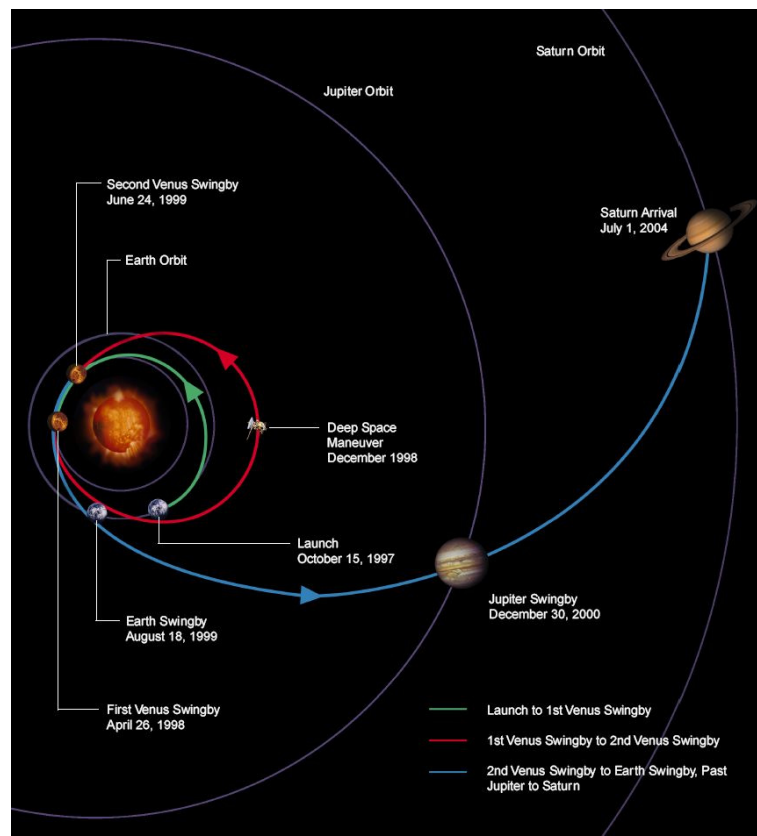
Figure 1.1: Cassini interplanetary trajectory

The spacecraft was designed and equipped to study several aspects of the Saturn system. The main scientific mission objectives included the study of Titan, the rings dynamics and composition, the icy satellites, Saturn itself and its magnetosphere. In particular some of the main scientific objectives related to Titan and the icy satellites are related to the study of their internal structure and composition. The determination of the mass and the gravity fields of Titan and the main icy satellites (Enceladus, Dione and Rhea) is then a crucial element to address these objectives. To reach all these objectives Cassini/Huygens is equipped with eighteen instru-

ments, twelve on the Orbiter and six on the Huygens Probe. Tables 1.1, 1.2 and 1.3 list the instruments and the associated mission objectives.

The remote-sensing pallet and the particles and field pallet are the two body-fixed platforms that host most of the scientific instruments. Magnetometers sensors are installed on the 11 meters long boom while the Radio and Plasma Wave Science experiment uses the three thin electrical antennae that point in orthogonal directions. Atop the spacecraft there is the 4-meter-diameter High Gain Antenna used by RSS (for further discussions about RSS see section 1.6). Two smaller low-gain antennae are used as backup and are located at the top of the HGA and near the bottom of the spacecraft. The Deep Space Network provides the communication with Cassini by means of a multiple frequency link which is received by the High Gain Antenna or by one of the low gain antennae.

Instrument	Technique	Scientific Objective
Cassini Plasma Spectrometer (CAPS)	Particle detection and spectroscopy. Electron spectrometer; Ion mass spectrometer; Ion beam spectrometer	In situ study of plasma within and near Saturn's magnetic field
Cosmic Dust Analyzer (CDA)	Impact induced currents	In situ study of ice and dust grains in the Saturn system
Dual Technique Magnetometer (MAG)	Magnetic field measurement. Flux gate magnetometer; Vector/scalar magnetometer	Study of Saturn's magnetic field and interactions with the solar wind
Ion and Neutral Mass Spectrometer (INMS)	Mass spectrometry	In situ compositions of neutral and charged particles within the Saturn magnetosphere
Radio and Plasma Wave Science (RPWS)	Radio frequency receivers. 3 electric dipole antennas; 3 magnetic search coils; Langmuir Probe current	Measure the electric and magnetic fields and electron density and temperature in the interplanetary medium and within the Saturn magnetosphere
Magnetospheric Imaging Instrument (MIMI)	Charge-energy-mass spectrometer	Global magnetospheric imaging and in situ measurements of Saturn's magnetosphere and solar wind interactions

Table 1.1: Cassini orbiter instruments for in situ measurements (Matson et al., 2002)

Instrument	Technique	Scientific Objective
RADAR	Synthetic aperture radar; radiometry with a microwave receiver	Radar imaging, altimetry, and passive radiometry of Titan's surface
Radio Science Subsystem (RSS)	X- and Ka-band transmissions to Cassini; Ka-, S- and X-band transmissions to the Earth	Study of atmospheric and ring structure, gravity fields, and gravitational waves

Table 1.2: Cassini orbiter radio remote sensing instruments (Matson et al., 2002)

Instrument	Technique	Scientific Objective
Composite Infrared Spectrometer (CIRS)	Spectroscopy using 3 interferometric spectrometers	Temperature and composition of surfaces, atmospheres, and rings within the Saturn system
Imaging Science Subsystem (ISS)	Imaging with CCD detectors; 1 wide angle camera (61.2 mr fov); 1 narrow angle camera (6.1 mr fov)	Multispectral imaging of Saturn, Titan, rings, and the icy satellites to observe their properties
Ultraviolet Imaging Spectrograph (UVIS)	Imaging spectroscopy, 2 spectrometers	Spectra and low resolution imaging of atmospheres and rings for structure, chemistry, and composition
Visible and Infrared Mapping Spectrometer (VIMS)	Imaging spectroscopy, 2 spectrometers	Spectral mapping to study composition and structure of surfaces, atmospheres, and rings

Table 1.3: Cassini orbiter optical remote-sensing instruments (Matson et al., 2002)

With a mass of 5636 kg at the time of launch and a height of 6.8 meters Cassini is the biggest spacecraft ever built by NASA (Henry, 2002). The dry mass is about 2523 kg and 3132 kg were propellant at launch. The spacecraft is made of several sections (see Fig. 1.2). Starting at the top of the spacecraft and moving downwards there is the High Gain Antenna (HGA), the twelve-bay electronics compartment, the upper equipment module, the propellant tanks with the engines and the lower equipment module. Until its release in December 2004 attached on one side there was the three-meter diameter Huygens probe.

Cassini is a three-axis stabilized spacecraft with the origin of the coordinate system located at the center of the plane which divides the principal electronic bus from the surrounding structure. The remote sensing platform is mounted on the +X side of the probe, the magnetometer boom extends in the +Y direction and the +Z axis completes the orthogonal triad by pointing in the direction of the main engine. Attitude control is performed either through three reaction wheels or by a set of 0.5 N thrusters. The instruments are body-fixed, therefore, in order to point them, attitude changes are often required. As a consequence real-time communication with the Earth is rarely possible and most of the observations have to be recorded and later sent to Earth. For the same reason, gravity observations that require the antenna to be pointed towards the Earth are usually incompatible with

other kind of observations.
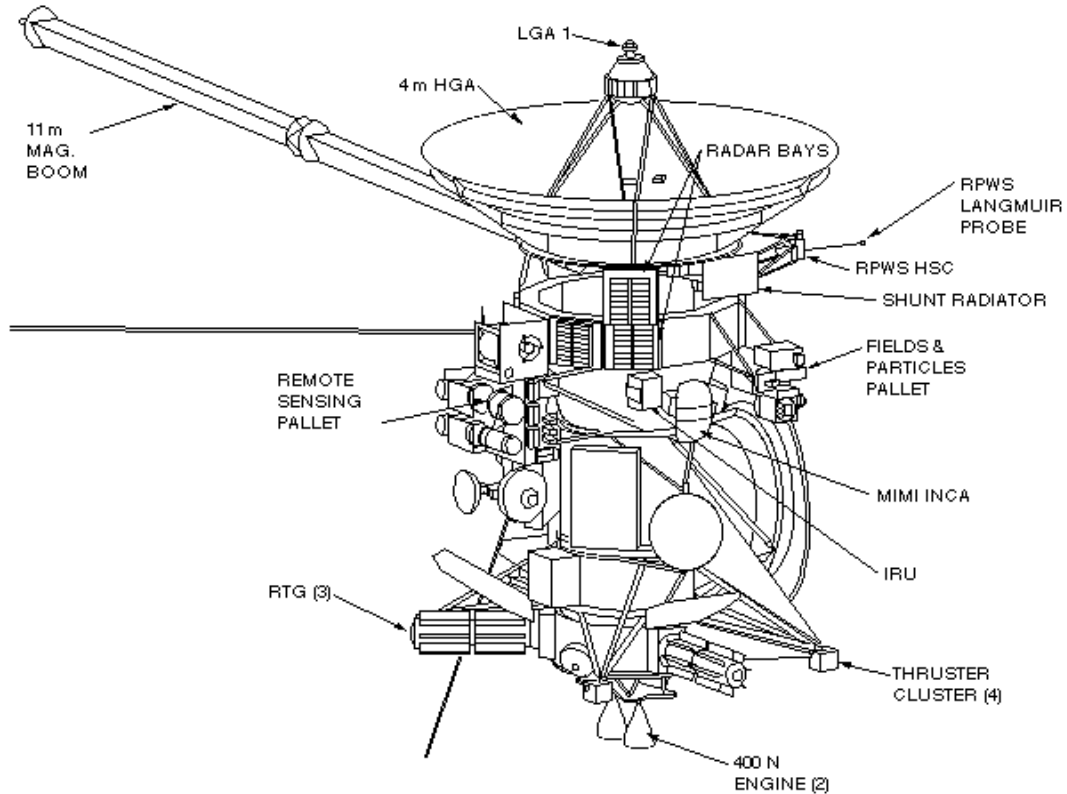
Figure 1.2: The Cassini spacecraft

Three Radioisotope Thermoelectric Generators (RTG) provide electrical power for the Cassini spacecraft and instruments. RTGs are electrical generators that convert the heat generated by the decay of a suitable radioactive material into electricity by means of solid-state thermoelectric converters. On Cassini RTGs power comes from the decay of plutonium (Pu-238, a non-weapons-grade isotope).

The spacecraft temperature is controlled by several means:

- multilayer thermal blankets that can provide also protection from micrometeoroids.

- reflective coatings like the HGA painted surface that has an allowable temperature range of about -200 to +125 degrees Celsius.

- electrical heaters

- small radioisotope heater units

- waste heat produced by some device operation

- surfaces used to shade other parts of the spacecraft. The HGA is the most important one and was used to shade the spacecraft from the Sun during the cruise phase.

1.2   Cassini Tour in the Saturn System

Cassini-Huygens entered the Saturnian system on 1 July 2004 when, after the SOI (Saturn Orbit Insertion) maneuver, it was inserted on a highly eccentric orbit around Saturn. This event marked the beginning of the 4 years nominal mission. Six months later, on 25 December 2004, Cassini orbiter released the Huygens probe into Titan's atmosphere where it entered 20 days later and landed on the surface after a two hour parachute descent.

The nominal mission included 75 orbits of Saturn, 44 targeted Titan flybys and several encounters with the other icy satellites. In order to save propellant targeted flybys of Titan have been used to change the orbiter trajectory throughout the mission. A single Titan flyby can in fact change the Saturn relative velocity by up to 850 m/s (Wolf, 2002). To understand the propulsive power of Titan this value can be compared to the 627 m/s ΔV of the SOI maneuver and the 500 m/s ΔV available for the entire tour. Therefore, by properly selecting the flyby geometry, Cassini tour designers were able to build an extraordinary complex tour that allowed countless observations and produced a wealth of scientific discoveries.

The first mission extension, called "Cassini Equinox Mission" began in July 2008 and ran until October 2010. The name of this extended phase refers to the fact that during the mission period the Sun passed the equatorial plane for the Saturn equinox. This extended mission tour was designed to answer the open questions that the Primary Mission had left either in terms of scientific investigations or in missing geometric conditions. During this phase Cassini performed an additional 27 Titan flybys and other icy moons flybys. In particular, after observations in the Primary Mission have revealed the presence of active cryovolcanism, seven flybys of Enceladus were scheduled to study in depth the phenomenon.

To date Cassini is in its second mission extension called the "Cassini Solstice Mission" that will run until the Saturnian Summer Solstice. In May 2017 the Sun will reach its highest elevation on the northern hemisphere. The Solstice mission will focus on the study of seasonal effects in the Saturnian system. Being the most
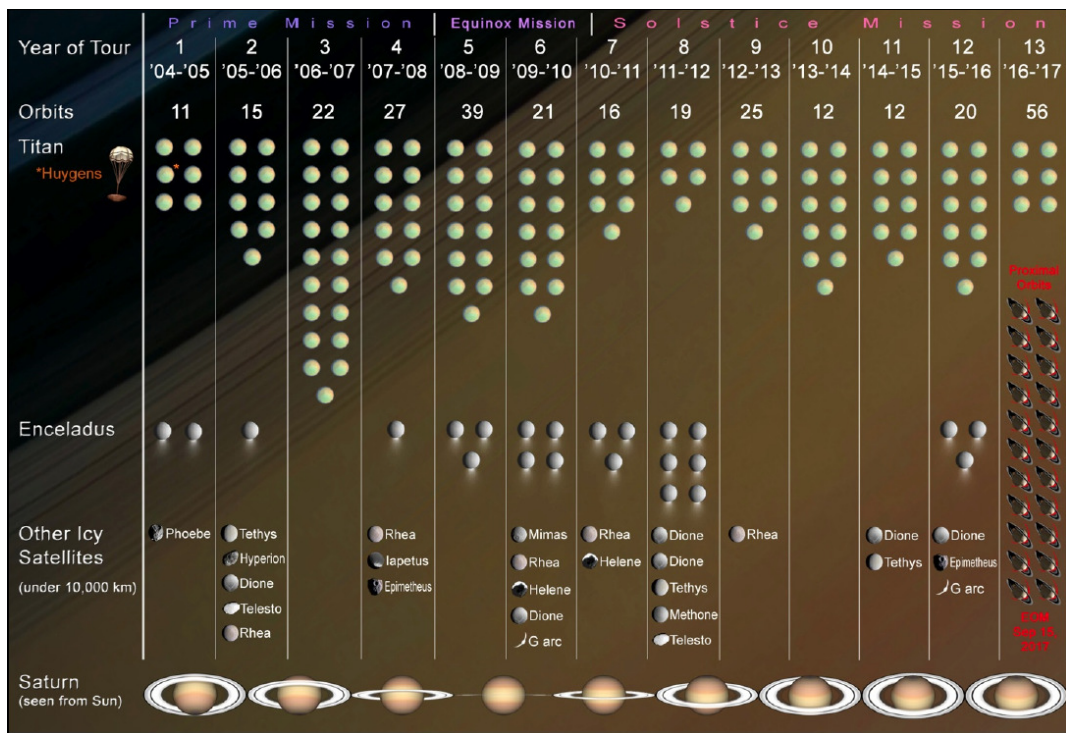
Figure 1.3: Overview of the Cassini tour from 2004 to 2017 with all the flybys performed in each mission phase (David Seal, NASA)

intriguing objects, Titan and Enceladus will be the most visited moons with 56 and 12 targeted flybys respectively.

The thirteen-year tour can be split into phases based upon the inclination of Cassini's orbit with respect to Saturn. The low inclination orbits, near the ring plane, permitted Cassini to have close encounters with icy moons while high inclination orbits resulted in fewer moon flybys. The high inclination orbits allow instead to look onto the rings and atmosphere and permit the in-situ instruments to explore all parts of the magnetic field and the energetic particle environment. Of course, Titan is always used to change the orbit of Cassini in every phase.

The Cassini mission is scheduled to end in September 2017 when the spacecraft will vaporize into Saturn's atmosphere. Before that, from April 2017 the spacecraft will be injected into the so-called "proximal orbits" with a periapsis between Saturn cloud top and the innermost D ring. These final 42 orbits are similar in many ways to the Juno mission at Jupiter and will enable unique science such as the determination of Saturn's internal structure from gravity measurements.

1.3 Titan

With a mean radius of 2574 km Titan is Saturn's biggest moon and the second in size, after Ganymede, among the satellites of the Solar System. It was discovered in 1655 by the Dutch scientist Christiaan Huygens and has always been one of the most studied objects among scientists. In 1908 a Catalan astronomer made the first observations of Titan atmosphere (Solá, 1908). In 1944 Gerald Kuiper confirmed previous observations using a spectroscopic technique (Kuiper, 1944). Only in 1980, when Voyager 1 visited Titan, the atmosphere composition was determined. It turned out that it is composed primarily by nitrogen with the presence of methane, many complex hydrocarbons and nitriles. However, the complex organic chemical activity produce an orange-colored haze which is opaque in the optical range and prevents direct observation of the surface. For this reason, prior to Cassini radar observations, only large surface features were observed such as North-South atmospheric asymmetries and cloud systems. Data acquired during the single Voyager 1 encounter with Titan were crucial to answer some of the questions about Titan's origin, evolution and present structure. Moreover they contributed to increase the level of interest in Titan and posed new questions to be answered by the Cassini-Huygens mission.

Titan likely formed from a disk of material around Saturn, probably less massive

than the one that led to the formation of the Galilean satellites, given their higher density with respect to Titan. Cassini measurements have not detected a magnetic field on Titan yet, thus its interior is constrained only through gravity measurements (Iess et al., 2010). These measurements have allowed the construction of new models of Titan's interior structure that suggest the presence of a silicate core with a partially differentiated structure made of a water-rich mantle and an internal ocean a few tens of kilometers below the surface.

Titan has a complex morphology with many features resembling to an Earth-world like. Some features are similar to the other icy satellites while others are present only on Titan. Observations made by VIMS, ISS and the RADAR showed that Titan's surface is extremely young and dynamically active with tectonic, pluvial, fluvial, lacustrine, aeolian and cryovolcanic processes that result in a very complex surface morphology and composition. Titan's surface is fairly smooth with reliefs ranging from a few tens to a couple of hundred meters and depressions that were interpreted as old lakebeds (Langhans et al., 2012). Titan also hosts vast erosional and depositional features. There are dunes, especially in the equatorial regions, vast channel systems that cross big areas. Some of these channels are dry (resulting in brighter radar images) while other may contain small amounts of liquid. Lakes, probably composed of liquid methane, ethane and other simple hydrocarbons have been observed near Titan's north pole. There are evidences suggesting that these lakes are at least partially seasonal. Their changes are caused by volatile transport between polar regions and this is the reason why at least one lake, called Ontario Lacus and made only by ethane, has been observed in the south-polar region. Titan's surface hosts a small number of impact craters and only a few have been successfully identified. The lack of small craters can be explained because the small impactors may have been burned in Titan's thick atmosphere. However, the lack of bigger craters can only be explained by erosional and relaxation processes.

Titan has a dense, nitrogen-rich atmosphere with some other minor constituents. It is the only moon in the Solar System to have more than a trace of atmosphere since it extends more than the Earth's atmosphere. Methane is the second most abundant molecule with a relative presence of 5% near the surface and 1.4% in the stratosphere. Data from the Huygens Atmospheric Structure Instrument (HASI) provided evidences that Titan's atmosphere is essentially isothermal from 500 to 1100 km with a temperature of ~ 170 K (Lorenz et al., 2006). The troposphere is also fairly stable with a well defined tropopause at around 44 km of altitude. Zonal winds have been observed to be mostly in the sense of Titan's rotation. The winter

circumpolar vortex can have winds of up to 190 m/s at 300 km of altitude. Titan has also an ionosphere that starts at altitudes below 1000 km. Solar ultraviolet, x-rays and magnetospheric electrons produce a variety of ion species that have an important effect on Titan's lower atmosphere. The majority of ion species is constituted by nitrogen and methane but other molecules such as hydrogen and other organic molecules have been identified.

1.3.1   Physical characteristics and interior structure

Titan is the largest satellite of Saturn (2575.5 ± 0.2 km[1]) and intermediate in size between the Galilean satellites Callisto (241032 ± 1.5 km[1]) and Ganymede(2631.2 ± 1.7 km[1]). Its mean density is 1.882 ± 0.001 g/cm^3 and the gravitational parameter GM $8.978.19 \pm 0.06$ km^3/s^2 (for a complete list of physical and orbital characteristics see table 1.4). Titan is in synchronous rotation around Saturn, which means that its orbital period is equal to the rotation period, and therefore tidally-locked. The rotation axis is inclined with respect to the normal to the orbital plane of $0.3°$ (Stiles et al., 2008).

Semi-major axis[1]	1221865	km
Orbital Period[1]	15.95	d
Rotation Period	$Synchronous$	
Eccentricity[1]	0.0288	
Inclination[1]	0.306°	
Mean Radius[2]	2574.73 ± 0.09	km
GM[2]	8978.1382 ± 0.0020	km^3/s^2
Mean Density[2]	1.882 ± 0.001	g/cm^3
Albedo[1]	0.2	

Table 1.4: Orbital and physical characteristics of Titan

The observations used to constrain the interior structure come essentially from gravity measurements and orbital data such as the eccentricity, obliquity and rotation rate. The main question about Titan's interior is about its degree of differentiation and whether there is a liquid layer under the surface. While the study of Titan's dense atmosphere is crucial to provide important constraints on its origin and evolution, geophysical observations are severely limited since the surface cannot be observed in the visible light spectra. Therefore information about the interior

---

[1]from Solar System Dynamics website: http://ssd.jpl.nasa.gov
[2]from Jacobson et al. (2006)

structure come mainly from gravity field measurements. But again, the atmosphere of Titan prevents flybys at low altitudes thus limiting the sensitivity to the gravity signal (since it decrease inversely with the square of the distance). Nonetheless Cassini data provided valuable constraints to build up geophysical models of Titan's interior structure.

An icy satellite is supposed to be composed by several layers which could be a a core surrounded by a silicate shell, a high-pressure ice-shell, an ocean and a low-pressure surface ice layer. However not all these layers may be present and they can have different densities and composition. The mean density is derived from measurements of the GM and the shape. The observed value of 1881 kg/m^3 probably means that Titan's interior is roughly made by 60% rock by mass with the remaining being water ice (Grasset et al., 2000). The degree of differentiation can instead be inferred by determining the moment of inertia factor (MoIF) C/MR^2. If there is no differentiation and the satellite has only one layer the moment of inertia factor is 0.4. The moment of inertia can be obtained from the degree-2 gravity coefficients (see Chapter 2). Iess et al. (2010) determined a MoIF of about 0.34 which, combined with the mean density of Titan indicates that the satellite is partially differentiated and the density of its core is low. Castillo-Rogez and Lunine (2010) and Fortes (2011) explained it with the presence of highly hydrated silicate minerals while Iess et al. (2010) postulated an incomplete separation of rock from ice. The low internal temperatures required to maintain the hydrated silicate or the ice-rock mixture interiors are not fully compatible with the presence of a small iron core even though it cannot be completely ruled out.

In summary the most likely present-day structures are either a low density rock core consisting mainly, but not entirely, of hydrated silicate minerals surrounded by H_2O or a pure rock core, mostly anhydrous, surrounded by a mixture of ice and rock, surrounded by pure water ice. Both these structures are compatible with the presence of a liquid water layer between a high-pressure ice mantle and an outer ice shell (Fig. 1.4)

The MoIF can also be retrieved from orbital characteristics. A measurement of Titan's obliquity can in fact be directly related to its MoIF. By analyzing three years of Cassini SAR images of Titan, Stiles et al. (2008) provided a value of Titan's obliquity of 0.3. Bills and Nimmo (2008) showed that the MoIF inferred from this value (see figure 1.5) is not compatible with the gravity measurements. However they suggested that this can be an indication of the presence of a liquid layer that decouples the interior from the outer shell thus leading to this apparent inconsistency.
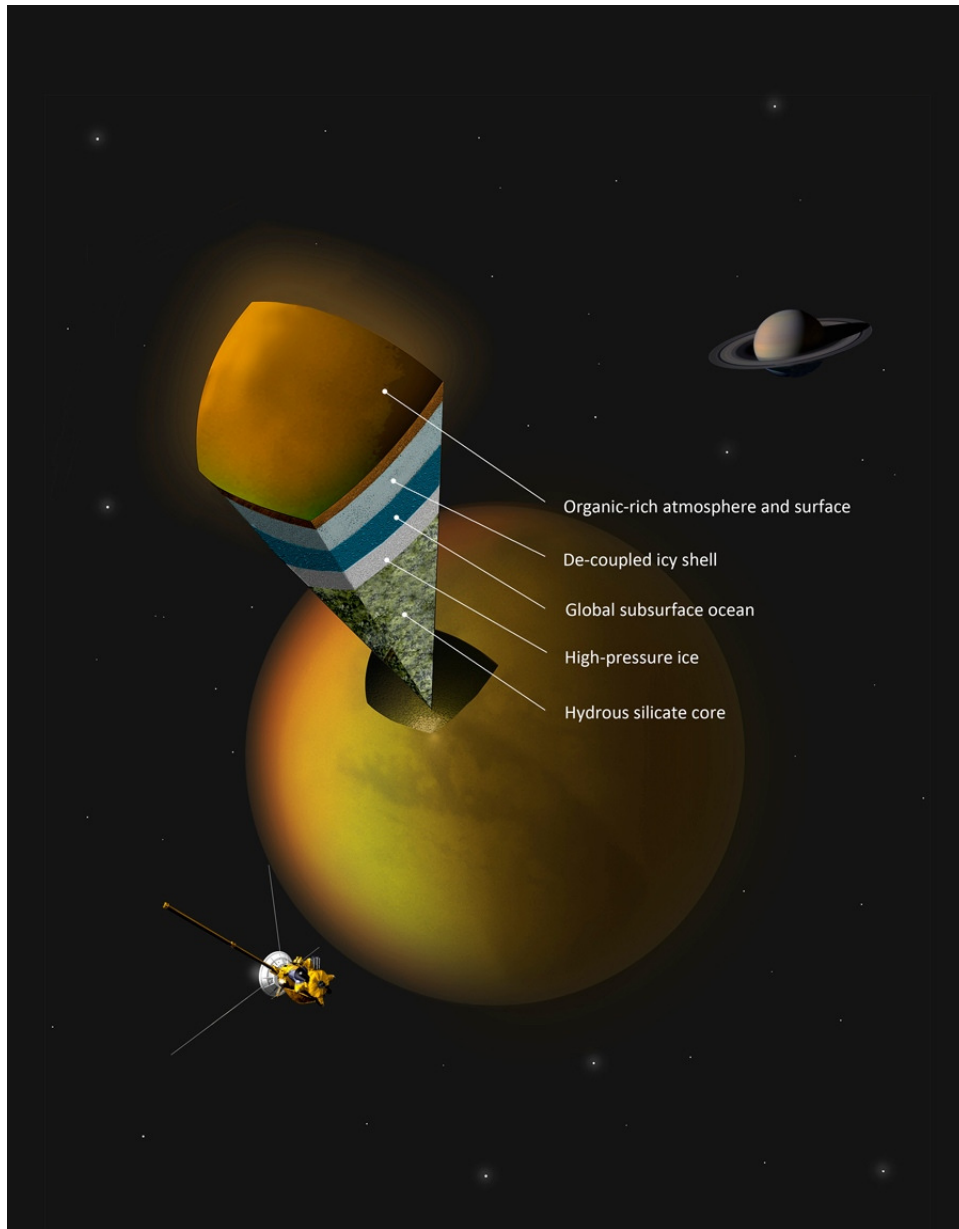
Figure 1.4: Internal structure of Titan (Credits: A. Tavani)
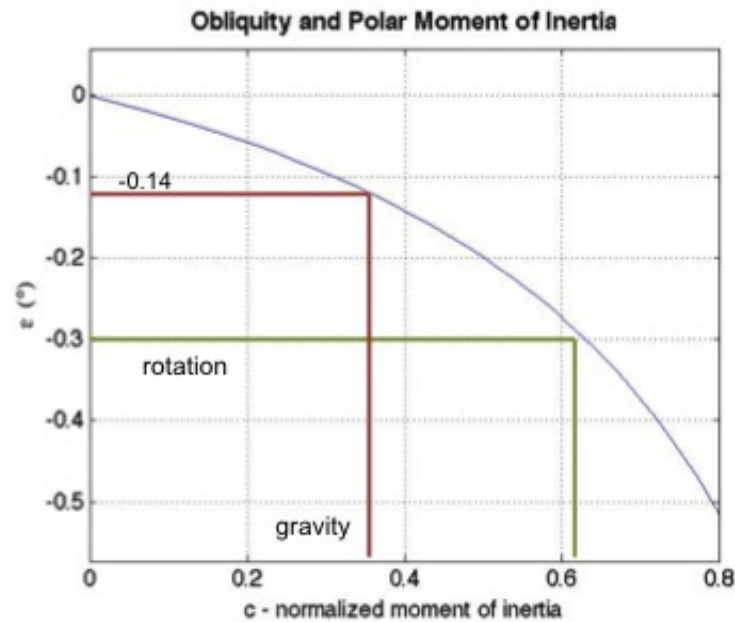
Figure 1.5: Titan's MoIF inferred from gravity and rotation

The last constraint on the internal structure comes from the high value of Titan's eccentricity. With a value of 2.9%[3] it is much larger than those of Ganymede (0.15%) and Europa (1%). However, while for Europa and Ganymede there is a Laplace resonance with Io that maintains their eccentricity, no such resonance exists for Titan and the eccentricity should be reduced by internal dissipation over time. Tobie et al. (2005) showed that if Titan's interior were dissipative the orbit would became circular in less than 300 Myr. This suggests that Titan's interior is not dissipative thanks to the presence of ammonia in the ocean that would lower the temperature of the ice crust reducing the dissipation rate by increasing the viscosities. Figure 1.4 shows a possible internal structure for Titan that take into account all the constraints previously described.

---

[3]from Solar System Dynamics website: http://ssd.jpl.nasa.gov

1.4 Enceladus

Despite its small size of only about 505 km in diameter, Enceladus is one of the most intriguing objects in the Saturn system and probably in the whole Solar system. It has been known to have unusual features since it was first visited by the Voyager probes in 1980 and 1981. They revealed an exceptionally high albedo and a surface with craters and fractures (Smith, 1982). In 1981, from ground-based observations, Baum et al. (1981) observed that the E-ring was located around the orbit of Enceladus. A geyser-like activity was suggested as a continuous source of supply for the E-ring particles. Subsequently, further observations from the Hubble Space Telescope confirmed that Enceladus appeared to be the source of the E-ring. The Cassini mission was therefore planned to study in depth this moon with three targeted flybys in the nominal mission and more than fifteen in the extended phases.

Enceladus orbits around Saturn at about 238000 km from the planet's center in an almost circular orbit. Like the other main satellites of Saturn it is tidally-locked with its rotation period of about 32 hours equal to the orbital period. Enceladus is the only icy satellite on which geological activity has been observed. It is probably caused by the tidal heating induced by the 2:1 mean motion resonance with Dione which also helps in maintaining Enceladus' orbital eccentricity (~ 0.0047).

Semi-major axis[4]	238042	km
Orbital Period[4]	1.370	d
Rotation Period	$Synchronous$	
Eccentricity[4]	0.0047	
Obliquity[4]	0.3°	
Mean Radius[5]	252.10 ± 0.10	km
GM[5]	7.2027 ± 0.0125	km^3/s^2
Mean Density[5]	1.608 ± 0.003	g/cm^3
Albedo[4]	1.375 ± 0.008	

Table 1.5: Orbital and physical characteristics of Enceladus

The mean density of Enceladus means that there is a significant fraction of silicates in its interior. So far, there are not direct evidences of differentiation but the presence of a core surrounded by a liquid layer (globally distributed or concentrated at the South Pole) and a thick ice shell has been postulated. The resolution of

---

[4]from Solar System Dynamics website: http://ssd.jpl.nasa.gov
[5]from Jacobson et al. (2006)

this issue is one of the objectives of this thesis and will be discussed in section 5.2.

Enceladus' surface is very heterogeneous with cratered terrains in the northern hemisphere and relatively smooth regions in the south polar region. This region is tectonically active and covered by fractures and ridges. The geyser activity is concentrated along four fractures called "tiger stripes". The plumes eject up to 200 kg/s of water vapor along with significant amounts of N_2, CO_2, CH_4, NH_3 and other minor components at a temperature of at least 167 K. It is not yet clear how the plumes are powered and if there is a liquid water deposit under the South Pole which provides the required amount of water. The presence of water along with a complex organics chemistry makes Enceladus a promising potential habitat for life in the outer solar system.
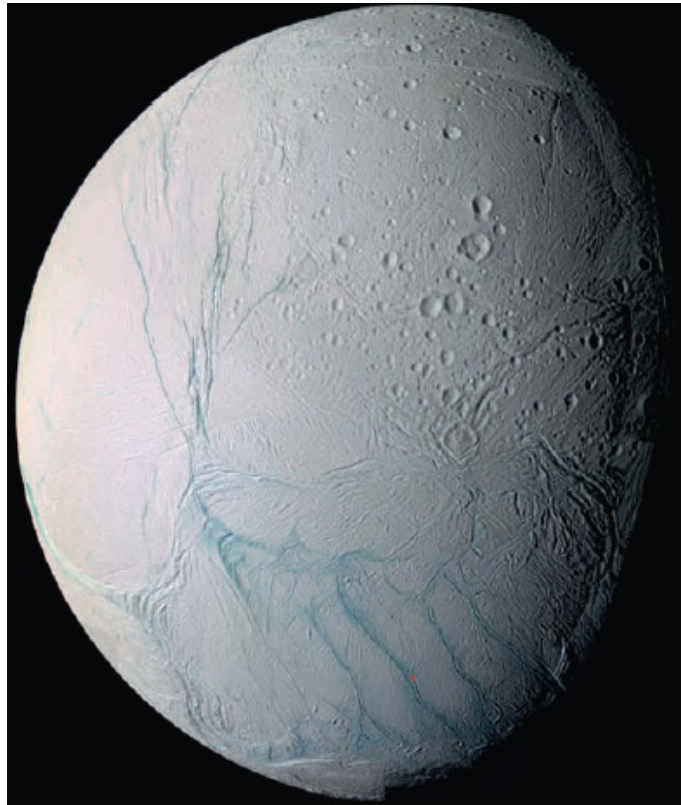
Figure 1.6: False-color view of Enceladus taken by ISS on July 2005 flyby. From Cassini Press Release PIA06254

1.4.1 Enceladus' plume

In 2005, during an Enceladus' flyby, Cassini magnetometer detected a tenuous atmosphere that was distorting the magnetic field of Saturn. The discovery of an atmosphere composed of water group molecules and ions suggested Cassini project to lower the closest approach altitude of the third flyby from 1000 km to 168 km to better investigate the south polar region. This flyby, which took place on 14 July 2005 confirmed with certainty the active nature of Enceladus. Multiple Cassini instruments contributed in the various aspects of this discovery. Images taken by Cassini ISS revealed the presence of jets of tiny icy particles and water vapor (Porco et al., 2006). The CIRS instrument detected 3 to 7 GW of thermal emission coming from the south polar trough the so called "tiger stripes" (Spencer et al., 2006). Also UVIS, by observing a stellar occultation, detected water vapor over the South Pole (Hansen et al., 2006). After subsequent observations by INMS and CDA, the presence of erupting plumes at the South Pole of Enceladus was clear.

In order to understand the phenomenon of the south polar plumes, different observations were used trying to answer several questions about the plumes' origin and composition. By measuring the speed, size and composition of the gas and of the particles ejected, the rate of vapor and particle loss, it can be inferred at what depth and how the plumes are generated. Moreover, the composition of the plumes can also tell if liquid water is involved in the process. The analysis of the correlations between the plumes location and the surface features can help in understanding how deep are the surface cracks and how long is the active period of the plumes.

On the basis of Cassini observations plausible models of the mechanisms that originate the plumes have been proposed. The main question is whether a liquid water source is required to generate the plume and how close it must be to the surface in order to avoid freezing. The observed heat on the surface can in fact be transported by water vapor that condensates in some subsurface location due to the high pressures or by a flow of liquid water. However, in order to maintain the warm surface temperatures ($\sim$ 180 K), the liquid water deposit would have to be very close to the surface if the thermal conduction is the only heat loss mechanism. In this case the ice would melt at only 4 m depth (Spencer et al., 2006). Moreover the latent heat lost by evaporation of the water at the surface cannot be replenished quickly enough by the heat transported upwards through the water by conduction or convection (Postberg et al., 2009). The water column would in fact rapidly freeze

at the surface.

Another way to bring heat to the surface is through water vapor transport that travels up from vertical fractures in the tiger stripes (Nimmo et al., 2007). The shape of the thermal emission measured by CIRS (see figure 1.7) is consistent with these fractures delivering heat to the tiger stripes' walls. The vapor transport mechanism would not require the presence of liquid water near the surface. The most likely plumes origin is then from vapor-filled chambers that overlay relatively large liquid water deposits from which the vapor reaches the surface through narrow fractures.
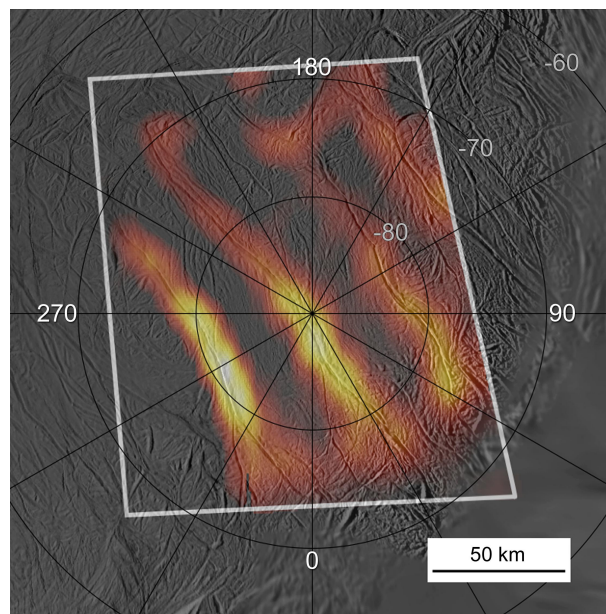
Figure 1.7: Thermal map of cracks near South Pole of Enceladus (NASA)

The speed of the ejected gases was inferred from the observations of its shape made by UVIS. The estimated velocity of ~ 600 m/s is higher than the thermal speed $(RT)^{1/2}$ but lower than its maximum theoretical value of ~ 816 m/s at 180 K surface temperature (if the gases initial enthalpy is entirely converted in kinetic energy). This implies the presence of a significant thermal gradient along the fractures (Spencer et al., 2009). The plume composition is dominated by water vapor and water ice particles which form by direct condensation of the water vapor before it is ejected on the surface (Schmidt et al., 2008). However it includes also numerous gas species and salts, mainly CO_2 and CH_4, which are in a $\sim$1:10 molar ratio with the water vapor (Waite et al., 2009).

1.5 Dione

Discovered by Cassini in 1684 Dione is the fifteenth largest moon in the solar system. It was imaged for the first time by the Voyager probes in 1981. Cassini spacecraft visited Dione for the first time on October 11, 2005, allowing the determination of its mass (Jacobson et al., 2006). Using data from the Cassini Imaging Science Subsystem (ISS), Thomas et al. (2007) determined Dione's shape and inferred its mean radius (561.7 ± 0.9 km) and density (1476 ± 7 kg/m^3). It turned out that Dione has the highest bulk density among the airless icy satellites. Since the largest mass fraction can be attributed to water ice the high density can be explained by the presence of a silicate rocky core. However, more detailed information about its internal structure, such as core dimensions and composition require the knowledge of at least the degree-2 gravity field. This issue has been addressed in this thesis and the results are discussed is section 5.3.

Figure 1.8: Image of Dione taken by Cassini during the April 2010 flyby (NASA-JPL)

The surface of Dione has very different regions in terms of crater density and surface features. There are highly cratered areas mainly in the trailing hemisphere and smooth plains on the leading one. This indicates that after the end of the accretion period, a significant geological activity endured the early bombardment. On the trailing hemisphere there is a surface structure that has been observed only on Dione. It is a pattern of high albedo fractures called "wispy terrain". Images taken by Cassini in the 2005 flyby (see figure 1.8) revealed that the "wisps" are bright ice cliffs created by tectonic fractures.

Semi-major axis[5]	377415	km
Orbital Period[5]	2.737	d
Rotation Period	$Synchronous$	
Eccentricity[5]	0.0022	
Inclination[5]	$0.028°$	
Mean Radius[6]	561.4 ± 0.4	km
GM[6]	73.1146 ± 0.0015	km^3/s^2
Mean Density[6]	1.478 ± 0.003	g/cm^3
Albedo[5]	0.998 ± 0.004	

Table 1.6: Orbital and physical characteristics of Dione

---

[5]from Solar System Dynamics website: http://ssd.jpl.nasa.gov
[6]from Jacobson et al. (2006)

1.6   Radioscience instrumentation

The radio science instrument is the ensemble of several subsystems distributed between the spacecraft and the ground stations that allow to obtain the required measurements for gravity observations. The complete description of the instrument and the experiments it carried out during the Cassini mission is given in Kliore et al. (2004). A functional block diagram of the complete instrumentation architecture is shown in figure 1.9.
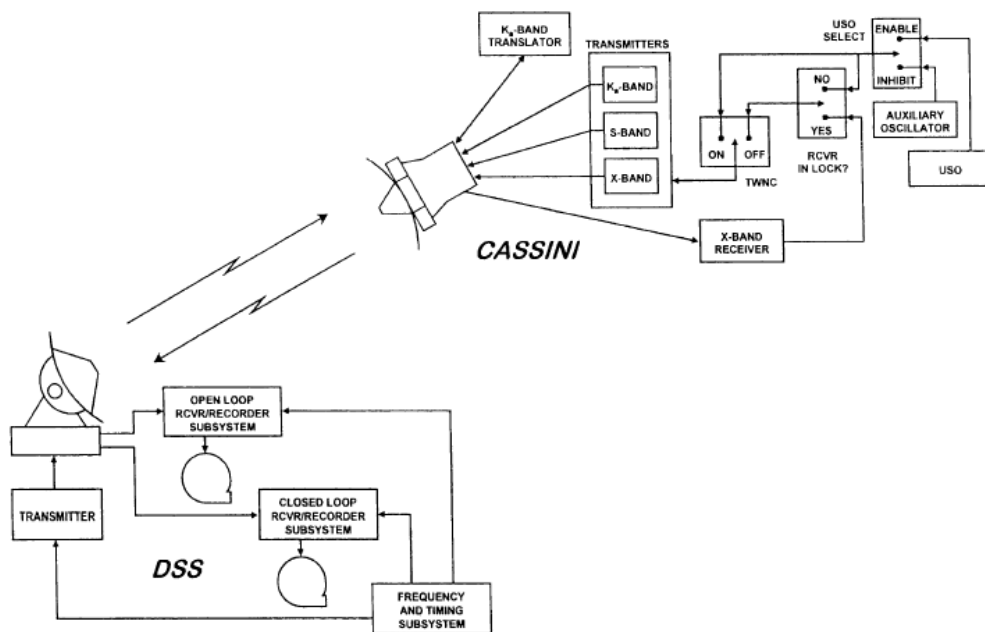
Figure 1.9: Overview of the radio science instrument (Kliore et al., 2004)

1.6.1   System overview

The instrument can operate in two-way and one-way mode. In the first configuration the uplink signal at X-band ($\sim 7.2\,\mathrm{GHz}$) and Ka-band ($\sim 34\,\mathrm{GHz}$) is generated by the station frequency standard which is given by a Hydrogen Maser. In actual operation mode the transmission frequencies are usually adjusted to compensate for the main part of the Doppler effect due to the relative motion between Cassini and the Earth. The spacecraft receiver collects the carrier signal with the High Gain Antenna (HGA), amplify and coherently transmits it back to Earth at one or more

downlink frequencies (see table 1.7 for the commonly used frequencies). The signal is received by the ground receiving equipment and recorded for later analysis. When the downlink is received at a different ground station the measurement technique is called three-way. One-way measurements are instead obtained by producing the signal source on board Cassini using the ultrastable oscillator (USO) and sending it to the ground station at S-band, X-band, or Ka-band. This technique is used essentially for atmospheric and rings occultation in which, especially for the egress phase, it is not possible to lock to an uplink signal.

Band	Uplink Frequency (MHz)	Downlink Frequency (MHz)
S	2110-2120	2290-2300
X	7145-7190	8400-8450
Ka	34200-34700	31800-32300

Table 1.7: Uplink and downlink frequencies used for deep-space communications

For gravity observations two-way transmission can provide the most accurate data thanks to the use of a very stable frequency standard at the ground station to reference the frequency measurements. Beside this, three-way data are also widely used when the geometric configuration do not allow continuous tracking from the same antenna.

1.6.2 Spacecraft segment

The radio science subsystem (RSS) is the spacecraft subsystem that performs the operations required for data acquisition. It is composed of three elements, two of which are not exclusively used for radio science: the Antenna subsystem, the Radio Frequency Instrument Subsystem (RFIS) and the Radio Frequency Subsystem (RFS).

The Antenna Subsystem

The antenna subsystem consists of one high-gain antenna (HGA) and two low-gain antennas (LGA). All the antennas can operate at X-band, but only the HGA can transmit all the radio science frequencies. The HGA is used for every communication with Earth as well as for radio science purposes. Moreover the HGA also transmits and receives data for the Cassini Radar. Funded by the Italian Space Agency and built by Thales Alenia Space, Cassini HGA is probably one of the most

complex antenna ever flown on a deep-space probe. It is capable of functioning at S-band, X-band, Ka-band, and Ku-band. All signals received and transmitted are circularly polarized. Cassini is able to receive and send both Right Hand and Left Hand Circulary Polarized Signals (RHCP and LHCP). Table 1.8 summarizes the main antenna subsystem functions and operational modes.

Antenna	Mode	Polarization	Frequency (MHz)	Function
HGA X-band	Transmit	RHCP	7175	Telecom
HGA X-band	Receive	RHCP	8425	Telecom
HGA Ka-band	Transmit	RHCP	32028	Science
HGA Ka-band	Receive	RHCP	34316	Science

Table 1.8: Cassini antenna subsystem operational modes

The Radio Frequency Subsystem

The Radio Frequency Subsystem (RFS) is primarily used to support spacecraft telecommunications and it is therefore a redundant subsystem to avoid any critical failure that could prevent sending commands to the probe. Commands and telemetry are received and transmitted at X-band whose carrier is also used to generate radio science signals. The main components of the RFS used for radio science experiments are: the two deep space transponders (DST), the X-band traveling wave tube amplifiers (X-TWTA) and the USO. The USO is the only non-redundant component since it is used only for radio science purposes.

During tow-way mode operations a 7.2 GHz uplink signal from the HGA or one of the two low gain antennas (LGAs) is received by the operating DST (the other one is used as backup if the first fails), amplified and multiplied by the turn around ratio of 880/749 to generate an 8.4 GHz downlink. The DSTs have a receiving band of about 50 MHz and are capable of locking onto signals as low as -155.8 dBm (Kliore et al., 2004). However, since the received frequency depends on the Doppler shift experienced by the signal during its transit from the Earth, the frequency of the uplink signal must be ramped accordingly to the predicted Doppler shift in such a way that the signal frequency received from the spacecraft is inside the 50 MHz bandwidth. The DST is also responsible for the generation of input signals for the S-band transmitter (SBT) and the Ka-band exciter (KEX) in the RFIS. The X-TWTA amplifies the X-band downlink from the DST to 15.8 W. Then the signal is sent to Earth through the HGA or one of the two LGAs. The beam width of the HGA is

approximately ~ 0.5 degrees at X-band and ~ 0.16 degrees at Ka-band. Therefore, when the spacecraft is not precisely Earth pointed it cannot use the HGA. In this configuration, when communication is provided through one of the LGAs, X-band is the only frequency available for radio science experiments.

The Radio Frequency Instrument Subsystem

The RFIS is the key subsystem for radio science experiments. The elements in the RFIS are devoted exclusively to radio science. The main elements of the RFIS are:

- the S-band transmitter (SBT)

- the Ka-band exciter (KEX)

- the Ka-band translator (KAT)

- the Ka-band travelling wave tube amplifier (K-TWTA)

The SBT and the KEX are used almost exclusively in one-way mode operations even if the KEX can also work in two-way (X-up, Ka-down) mode. The KAT was instead designed for two-way mode operations and its task was to enable the Ka-up Ka-down radio link by turning the 34 GHz uplink signal from the HGA into a coherent 32-GHz downlink. During Cassini cruise to the Saturn system the KAT proved to be capable of generating downlink signals with an Allan standard deviation (see section 3.2.3) of 3×10^{-15} @ 1000 s. The K-TWTA provided the required amplification for the output signals from both the KEX and the KAT. When the input is only one carrier the amplifier produces a total output power of 7.2 W, while when operating in dual-carrier mode an output power of 5.7W can be attained.

On Cassini, the combined capabilities of RFS and RFIS allowed the establishment of a triple link with ground: X-up X-down, X-up Ka-down, Ka-up Ka down. The simultaneous use of these three links allows the complete cancellation of solar plasma noise (Bertotti et al., 1993). During the cruise phase Cassini radio science experiments exploited the full system capabilities but in 2003 an unrecoverable failure on the KAT caused the loss of the Ka-up Ka-down link. The attainable accuracy achieved by Doppler data during Saturn tour was then reduced significantly.

1.6.3 Ground segment

The ground segment is a fundamental part of the radio science instrument as the accuracy of acquired data is directly related to the optimal performances and calibrations of the ground stations. Spacecraft tracking is accomplished by the Deep Space Network (DSN), a worldwide network of large antennas and communication facilities. It comprises three complexes located near Canberra, Australia, Madrid, Spain and Goldstone in the Mojave desert, South California evenly distributed around the globe with a longitude of approximately 120 degrees between each other. Each complex is equipped with several antennas, among which there are one 70 m diameter station, at least one 34 m beam-wave-guide (BWG) station and one 34 m high-efficiency (HEF) station. Table 1.9 reports the DSN station that are more often used for radio science experiments.

Location	Type	Name
Goldstone	70 m	DSS 14
	34 m BWG	DSS 25, DSS 26
Madrid	70 m	DSS 63
	34 m BWG	DSS 54, DSS 55
Canberra	70 m	DSS 43
	34 m BWG	DSS 34

Table 1.9: DSN antennas

Transmitting and receiving facilities

The 70 meters diameter stations are equipped for transmission and reception at S- and X-band frequencies and allows the reception of both right circular and left circular polarized signals. These tracking stations are not used for tracking Cassini throughout the closest approach of a gravity flyby because Ka-band reception is not available. Nonetheless, 70 meters antennas are often used for X-band tracking passes before and after closest approach. The 34-meters diameter BWG stations have the full operating capabilities for radio science gravity experiments. The transmitting and receiving facilities can operate at X- and Ka-band. Moreover, the 34-meters BWG antennas in Goldstone and Madrid are equipped with advanced systems for tropospheric path delay calibration.

The transmitted signal is generated using a reference frequency, ramped to account for the Doppler shift on the uplink and then translated to the requested chan-

nel frequency for the selected spacecraft. The transmitted frequencies are recorded for later processing of two-way Doppler data. After the signal has been sent back to the Earth from the spacecraft two types of receivers are available at the DSN tracking stations to process the acquired data:

- The open-loop receivers that record directly the received signal in a selected bandwidth around the carrier signal using a tunable local oscillator whose frequency is selected according to the predicted downlink frequency. The advantage of open-loop receivers is the flexibility provided by the possibility of non-real time data processing.

- The closed-loop receivers that are the most used at the DSN stations for receiving telemetry and tracking data. They estimates the signal phase and amplitude in real time by locking to the signal carrier through a Phase Locked Loop (PLL). On the basis of the closed-loop receiver output the tracking subsystem provide the measurements of Doppler shifts and ranging.

Time and frequency standards

The accuracy of radio science data is highly dependent on frequency and timing metrology. Tracking signals must in fact be generated by very stable, accurate and precise clocks as well as all received signals must be referenced against the same high performance clocks. The frequency stability is granted at each Deep Space Complex by a complement of two hydrogen masers and two cesium-beam clocks. The H-masers along with a clean-up oscillator are used as the reference timing source to drive the local oscillators throughout the complex. For typical tracking times of deep space probes ($\sim$ 8 hours) H-masers provide their best stability (Allan deviation of $\sim 10^{-15}$ for integration times between 1000 and 10000 seconds). To achieve short-term stability the H-masers are usually cleaned up with the best available quartz oscillators. Moreover, when available, a Cryogenic Sapphire Oscillator (CSO) is used for phase noise cleanup during radio science activities with Cassini. Cesium beam clocks are instead used as backup to support basic communication with the tracked spacecraft when there is a failure on the H-masers. However, their frequency stability is not adequate to be used for radio science activities (Fig. 1.10).
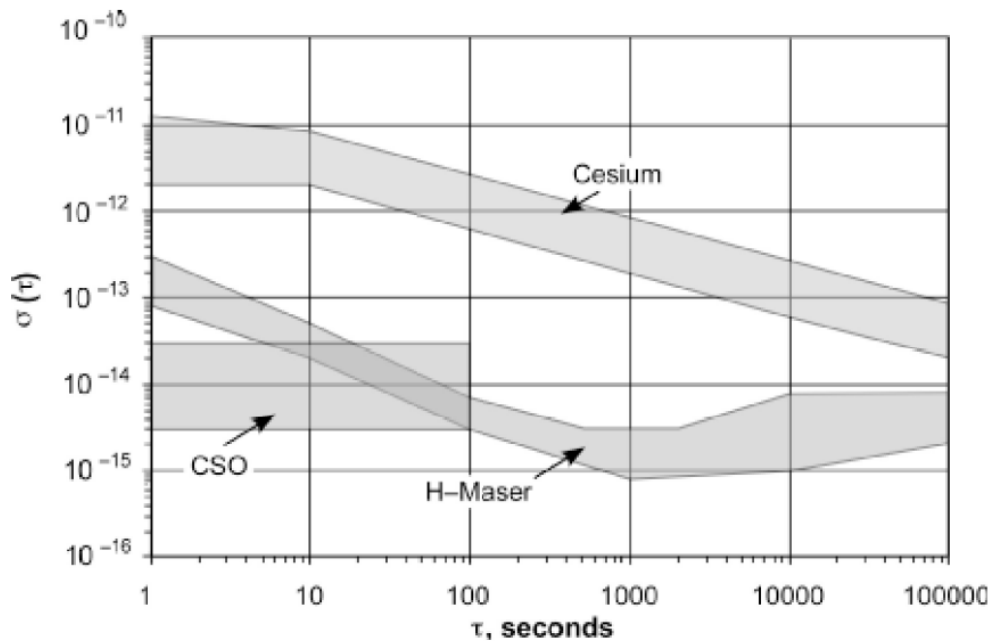
Figure 1.10: Allan deviation of DSN frequency standards (Tjoelker, 2010)

Media Calibration System

The Earth's troposphere is a major source of noise on phase and amplitude of the radio signal received from the spacecraft (see section 3.2.3). Doppler measurements are significantly affected by path delay variations due to the water vapor, especially at low elevation angles. The Tracking System Analytical Calibration (TSAC) allows a good calibration of the dry component of the tropospheric delay by using a combination of multidirectional, dual frequency GPS measurements and weather data at each station complex. However it cannot detect accurately the wet component of the tropospheric path delay associated with short-term variations of the columnar water vapor content. For this reason a new media calibration system was implemented starting from Cassini radio science cruise experiments (Resch, 2002). The Advanced Media Calibration (AMC) system was installed near the 34 m BWG antennas DSS 25 in Goldstone and DSS 55 in Madrid and comprises for each unit a water vapor radiometer, a digital pressure sensor and microwave temperature profiles. This system improve the accuracy of the path delay induced by the wet part of the troposphere providing an improvement in the final data quality.

Chapter 2

From gravity to interior structure

In this chapter is given the description of the theoretical background and analysis methods used to retrieve information about the interior structure of the main saturnian satellites. The determination of the interior structure of a celestial body relies mainly on two different methods. The first one is through the analysis of the deviations of the gravitational field from the monopole term GM/r, while the second one is based on the analysis of the rotation of the body. None of these methods can provide complete information about the interior but nonetheless they can put important constraints thus giving the possibility to infer the origin and evolution of a celestial body. Here we focus on how retrieving information about the interior structure from the gravity field.

2.1 The gravity field of an isolated body

The gravitational potential energy outside an isolated body of any internal structure can be described by the full Poisson's integral:

$$U(\mathbf{r}') = -G \int \frac{1}{|\mathbf{r} - \mathbf{r}'|} \rho(\mathbf{r}') dV \qquad (2.1)$$

The most used mathematical tool to solve this integral and to express the gravitational field of any non-spherical body is by using a multiple series of spherical harmonic functions (Bertotti et al., 2003). For an isolated body, supposing the center of mass coinciding with the center of the reference system, we have (Kaula, 1966):

$$U(r, \theta, \phi) = \frac{GM}{r} \left[1 + \sum_{l=2}^{\infty} \sum_{m=0}^{n} \left(\frac{R}{r} \right)^n \left(C_{lm} \cos(m\phi) + S_{lm} \sin(m\phi) \right) P_{lm}(\cos(\theta)) \right] \qquad (2.2)$$

Where M is the body mass, G is the gravitational constant. With respect to the center of mass the spherical coordinates r, θ, ϕ are respectively the radial distance, latitude and longitude on the equator. P_{lm} is the associated Legendre polynomial of degree l and order m; and C_{lm} and S_{lm} are the corresponding harmonic coefficients.

The quadrupole term (l=2) gives the first deviation from spherical symmetry. The five quadrupole gravity coefficients can be easily related to the inertia tensor I. In fact it is defined as:

$$\mathsf{I} = \int [\mathbf{1} r'^2 - (\mathbf{r'r'})]\rho(\mathbf{r'})dV \tag{2.3}$$

On the other hand the quadrupole term of the Poisson's integral in equation 2.1 is given by:

$$\mathsf{Q} = -G \int [3(\mathbf{r'r'}) - \mathbf{1} r'^2]\rho(\mathbf{r'})dV \tag{2.4}$$

By comparing equations 2.3 and 2.4 we can derive the MacCullagh formula:

$$\mathsf{Q} = \frac{1}{3} Tr\mathsf{I} - \mathsf{I} \tag{2.5}$$

If we express both the quadrupole tensor and the inertia tensor in the same reference frame and at the same time the following relations can be derived (Milani and Gronchi, 2010):

$$
\begin{aligned}
C_{20} &= \frac{1}{MR^2}\left(\frac{I_{11}+I_{22}}{2} - I_{33}\right), \qquad C_{22} = \frac{1}{4MR^2}(I_{22}-I_{11}), \\
C_{21} &= -\frac{1}{MR^2}I_{13}, \quad S_{21} = -\frac{1}{MR^2}I_{23}, \quad S_{21} = -\frac{1}{2MR^2}I_{12}
\end{aligned}
\tag{2.6}
$$

Given that we have five equations and six unknowns is clear that, using gravity, we can determine only the difference between the moments of inertia (i.e. the mass unbalance) but not their single value. However quadrupole gravity can provide the principal axes of inertia. In fact, the linear relationship between I and Q (equation 2.5) means that they share the same eigenvectors. Therefore the principal axis of inertia can be retrieved by diagonalizing the quadrupole tensor Q which has the following expression:

$$\mathsf{Q} = \frac{\sqrt{5}}{3}MR^2 \begin{pmatrix} -(C_{20}-\sqrt{3}C_{22}) & \sqrt{3}S_{22} & \sqrt{3}C_{21} \\ \sqrt{3}S_{22} & -(C_{20}+\sqrt{3}C_{22}) & \sqrt{3}S_{21} \\ \sqrt{3}C_{21} & \sqrt{3}S_{21} & 2C_{20} \end{pmatrix} \tag{2.7}$$

2.2   The degree-2 gravity potential for synchronous rotating bodies

In the case at hand, in which we deal with the main satellites of Saturn, some simplifications can be made due to the particular dynamical configuration of the problem. In fact all the major satellites of Saturn are in synchronous rotation around the central body and they move on nearly circular orbits that lie in the orbital plane of Saturn ($i = 0$). Moreover their rotation axis is almost coinciding with the normal to the orbital plane. In this configuration, if we add the hypothesis that the body in exam is in hydrostatic equilibrium, it is possible to assume that the deviations from the spherical symmetry (the quadrupole gravity) are only due to rotation and tides. The centrifugal potential energy of a body rotating with a constant angular velocity ω is (Kaula, 1966):

$$U_r = -\frac{1}{2}\omega^2 r^2 \sin\theta = -\frac{1}{3}\omega^2 r^2 (1 - P_{20}(\cos\theta)) \tag{2.8}$$

Where r is the radial distance from the center of the satellites and θ is the colatitude. The constant term is absorbed in the total GM and can thus be neglected.

The degree-2 potential due to the central body is:

$$U_{2t} = -\frac{1}{2}\frac{GM}{a^3}r^2[P_{20}(\cos\psi) - \frac{1}{2}P_{22}(\cos\psi)\cos 2\phi] \tag{2.9}$$

where a is the semimajor axis of the satellite's orbit, M is the mass of the primary body (Saturn in our case) and ψ is the angle from the direction connecting the satellite and the primary body. For a synchronous rotating satellite rotational and orbital period can be related using Kepler's III law:

$$\omega = \sqrt{\frac{GM}{r^3}} \tag{2.10}$$

In order to characterize the effect of the tidal and rotational field the following parameters can be defined:

$$q_t = -3\frac{M}{m}\left(\frac{R}{a}\right)^3 \qquad q_r = \frac{\omega^2 R^3}{GM}$$

where m and R are respectively the mass and the mean radius of the satellite. The tidal parameter q_t represents the ratio between Saturn tidal field and the satellite surface gravity. The rotational parameter q_r is instead the ratio between the cen-

trifugal acceleration at the equator and surface gravity acceleration. For a synchronous rotating body where the mean motion is equal to the angular velocity (equation 2.10) there is a linear relationship between the two parameters: $q_t = -3q_r$. The total perturbing potential at the surface of the satellite can then be expressed as the sum of tidal and rotational potentials (eqs 2.8 and 2.15). If we assume that the reference frame has the x axis pointed along the direction of the central body barycenter and it is coinciding with the principal axes of inertia, only J_2 and C_{22} are not equal to zero. A further hypothesis is that the rotational axis of the satellite is coinciding with the normal to the orbital plane (i.e. $i = 0$) which is a valid approximation for the main satellites of Saturn. Therefore, given that $\cos \psi = \sin \theta \cos \phi$, the total perturbing potential is given by:

$$U_2 = U_{2r} + U_{2t} = \frac{GM}{R} \left(\frac{r}{R} \right)^2 \left[\frac{(2q_r - q_t)}{6} P_{20}(\sin \theta) + \frac{q_t}{12} P_{22}(\sin \theta) \cos 2\phi \right] \quad (2.11)$$

The static part U_{2s} causes a permanent deformation of the planet which is proportional to the perturbing potential. The proportional coefficient that gives the induced potential is the fluid Love number k_f. This number reaches its theoretical upper limit of 3/2 for a fluid body but can be significantly smaller in case of differentiated bodies. By comparing eqs. 2.11 and 2.2 the degree-2 gravity coefficients J_2 and C_{22} of the induced potential assume the following expression:

$$J_2 = \frac{1}{6} k_f (2q_r - q_t) = \frac{5}{6} k_f q_r$$
$$C_{22} = -\frac{1}{12} k_f q_t = \frac{1}{4} k_f q_r \quad (2.12)$$

Therefore, for a synchronous rotating satellite in hydrostatic equilibrium, in a reference frame coinciding with the principal axes of inertia, the following relationship holds:

$$\frac{J_2}{C_{22}} = \frac{10}{3} \quad (2.13)$$

2.3 The Radau-Darwin equation

To infer information about the interior structure of a synchronous rotating satellite we make use of the Radau-Darwin equation. This equation allows to relate the moment of inertia factor of a body (C/MR^2) to the quadrupole gravity coefficients J_2 or C_{22}. On the basis of the work done by Clairaut (Clairaut, 1743), this relation was first derived by Radau (Radau, 1885) and some years later Darwin (Darwin,

1899) gave also his contribution. The Radau-Darwin relation is an approximation which is valid only for bodies in hydrostatic equilibrium. There are several form of this equation but here is reported the one in terms of the fluid Love number k_f (Jeffreys, 1962):

$$\frac{C}{MR^2} = \frac{2}{3}\left[1 - \frac{2}{5}\sqrt{\frac{4 - k_f}{1 + k_f}}\right] \tag{2.14}$$

The first step is to measure J_2 and C_{22}. The best way would be to obtain an independent estimation of the two parameters and then verify if their ratio satisfy the hydrostatic equilibrium hypothesis (eq. 2.13). If this is the case, the fluid Love number k_f can be computed either from J_2 or C_{22} (eq. 2.12) and used to determine the Moment Of Inertia Factor using 2.14. The inferred MoiF can be be used to give a first estimation of the interior structure of the body. Given that a MoiF of 0.4 indicates a uniform density body, if a lower value is found it possible to infer the presence of a certain degree of differentiation in the interior. This information along with the knowledge of the mean density (retrieved from the estimation of the satellite's GM) and shape can be used to infer the composition and the stratification of the interior structure.

2.4 Satellite tides

If the satellite orbit has a non-negligible eccentricity the tidal perturbing potential has also a periodic term that has to be added to the total perturbing potential (Rappaport et al., 1997):

$$U_p = \frac{GM}{R}\left(\frac{r}{R}\right)^2\left[-\frac{-q_t}{2}P_{20}(\sin\theta) + \frac{q_t}{4}P_{22}(\sin\theta)\cos 2\phi\right]e\cos f \tag{2.15}$$

where f is the true anomaly of the satellite with respect to the central body. The proportionality coefficient between U_p and the induced periodic potential of degree-2 is the tidal Love number k_2 (Love, 1906.). Therefore the quadrupole coefficients J_2 and C_{22} vary along the orbit and a periodic term has to be added to the static values in eq. 2.12:

$$J_{2p} = -\frac{1}{2}k_2 q_t e \cos f$$
$$C_{22p} = -\frac{1}{4}k_2 q_t e \cos f \tag{2.16}$$

In case of an elastic response to the tidal perturbation the Love number k_2 is a real number. If there is a phase lag δ between the perturbing force and the resulting displacement, k_2 is a complex number. In general the periodic part of the quadrupole gravity coefficients assumes the following expression (Rappaport et al., 2008):

$$J_{2p} = -\frac{1}{2}k_2 q_t e \cos\left(M - \delta\right) = -\frac{1}{2}\Re(k_2)q_t e \cos M + \frac{1}{2}\Im(k_2)q_t e \sin M$$

$$C_{22p} = -\frac{1}{4}k_2 q_t e \cos\left(M - \delta\right) = -\frac{1}{4}\Re(k_2)q_t e \cos M + \frac{1}{4}\Im(k_2)q_t e \sin M \qquad (2.17)$$

$$S_{22p} = -\frac{1}{6}k_2 q_t e \sin\left(M - \delta\right) = -\frac{1}{4}\Re(k_2)q_t e \sin M + \frac{1}{4}\Im(k_2)q_t e \cos M$$

Where the complex Love number is:

$$k_2 = \Re(k_2) + i\Im(k_2), \text{ with } \begin{array}{l} \Re(k_2) = k_2\cos\delta \\ \Im(k_2) = -k_2\sin\delta \end{array} \qquad (2.18)$$

2.5   Gravity from topography

The gravity field cannot be always measured with the required accuracy due to the limited number of flybys devoted to gravity science. At the same time the inversion problem can be degenerative thus preventing to retrieve a unique gravity solution. Therefore it can be useful to constraint the estimate of the gravity field coefficients by using a different kind of information such as topography. In fact, supposing that the only non-uniformity in the body is given by topography, an exact relationship between the spherical harmonics expansion of gravity and topography can be retrieved. The approach presented here was derived by Wieczorek (Wieczorek and Phillips, 1998).

The Poisson's integral in equation 2.1 can be expressed in terms of Legendre polynomials by using the identity:

$$\frac{1}{|\mathbf{r} - \mathbf{r}'|} = \frac{1}{r}\sum_{l=0}^{\infty}\left(\frac{r'}{r}\right)^l P_l(\cos\psi) \qquad (2.19)$$

The Legendre polynomials can be expressed by means of the addition theorem (Arfken, 1985):

$$P_l(\cos\psi)\frac{1}{2l+1}\sum_{m=0}^{l}Y_{lm}(\theta, \phi)Y_{lm}(\theta', \phi') \qquad (2.20)$$

Y_{lm} is the spherical harmonic function of degree l and order m normalized to

4π:

$$\int_\Omega Y_{lm}(\theta, \phi)Y'_{lm}(\theta, \phi)d\Omega = \delta_{ll'}\delta_{mm'}4\pi \tag{2.21}$$

where $\delta_{ll'}$ is the Kronecker delta, $d\Omega = \sin\theta d\theta d\phi$ is the infinitesimal volume element and θ and ϕ are colatitude and longitude.

Suppose to have a topography $H(\theta, \phi)$ in the crust with density ρ_c, referenced to a radius D. Substituting eqs. 2.19 and 2.20 in the general expression of the Poisson's integral (eq. 2.1) yields:

$$U(r, \theta, \phi) = \frac{G\rho_c}{r} \sum_{lm} \frac{Y_{lm}(\theta, \phi)}{r^l(2l+1)(l+3)} \int_{\Omega'} Y_{lm}(\theta', \phi')r^{l+3} \Big|_D^{D+H(\theta', \phi')} d\Omega' \tag{2.22}$$

The last term can be expanded using the binomial theorem

$$[D + H(\theta', \phi')]^{l+3} = D^{l+3} \left[\sum_{n=1}^{l+3} \frac{H^n(\theta', \phi')}{D^n n!} \prod_{j=1}^{n}(l+4-j) \right] \tag{2.23}$$

where powers of topography have the following expression:

$$H^n(\theta', \phi') = \sum_{l'm'} h^n_{l'm'} Y_{l'm'}(\theta', \phi') \tag{2.24}$$

By inserting equations 2.23 and 2.24 into 2.22, using the orthogonal properties of the spherical harmonics functions and simplifying we obtain an exact relation between the gravity coefficients C_{lm} and the topography coefficients h_{lm}:

$$C_{lm} = \frac{4\pi\rho_c D^3}{M(2l+1)} \sum_{n=1}^{l+3} \frac{h^n_{lm}}{D^n n!} \frac{\prod_{j=1}^{n}(l+4-j)}{(l+3)} \tag{2.25}$$

It can be easily shown that the magnitude of each successive term in the above sum is decreasing. For this reason it can be truncated after the needed precision has been achieved. In the case at hand we only need to constraint the low degree harmonics of the gravity field by using the corresponding long wavelength topography. For this kind of problem the first term of equation 2.25 is enough. The simplified relation is then:

$$C_{lm} = C\frac{3\rho_c}{\bar{\rho}(2l+1)} h_{lm} \tag{2.26}$$

where $\bar{\rho}$ is the mean density of the body. The proportionality coefficient C takes

into account the possible presence of compensated topography. If the topography is fully compensated, any mass increase due to a relief on the surface is balanced by a decrease in the density of the underlying material at some depth in such a way that there is no gravity anomaly associated with that relief. On the other hand, if there is no compensation, the topographic relief directly produces a gravity anomaly. The degree of compensation is a crucial parameter to put constraints on the internal structure of a planetary body or to infer the presence of density anomalies (e.g. water deposits) under the surface.

Chapter 3

Mathematical formulation

This chapter describes the mathematical formulation used to model the problem of estimating the geodesy of the Saturnian satellites. The analysis of Cassini tracking data is accomplished through an orbit determination process that allows to estimate the unknown model parameters. When more flybys of a satellite are available they can be combined into a multi arc fit to retrieve a global and coherent solution that is based on the whole data set. Observables play a crucial role in this process since their accuracy is directly related to the uncertainties in the estimated parameters. A description of the kind of observables used in this work and the main error sources that affect them is given is section 3.2.

3.1   The orbit determination problem

The gravity field estimation of the main satellites of the Saturnian system is part of a more complex orbit determination problem. With this name we mean the process that allows the estimate of the relative motion of a space probe in a given reference frame starting from a set of so called observables. In the general case, in order to correctly solve this problem, you have to take into account all the dynamical effects that act on the spacecraft (both of gravitational and non-gravitational origin), and consider all the error sources in the observables and dynamical models.

The dynamical model includes at least the six elements of the position and velocity vectors at a given epoch but is usually expanded with dynamic and measurements parameters to improve the model accuracy and thus the estimate of the spacecraft trajectory. In this context the main problem is that the estimation of the spacecraft initial state has to be computed using a dynamical model which

is not fully correct, and a set of observations affected by measurement and systematic errors. Therefore, even though the number of observations is greater then the unknown model parameters, orbit determination problems have usually more unknowns (observational and model errors) than observations thus requiring a statistical approach to obtain a solution. This is done by using an iterative least square approach that allows obtaining the "best" solution which will be the solution that minimize a given cost function.

The orbit determination problem can be carried out by processing the observational data sequentially or by doing the analysis once all data have been collected. The sequential processing algorithm (usually called Kalman filter (Kalman, 1960)) is useful when real time knowledge of the spacecraft state is needed. In our case the long transmitting time (around 1.5 hours) from Saturn to Earth will prevent in any case a real time estimation. For this reason we always process data with a batch algorithm after all measurements have been collected.

3.1.1 The orbit determination process

The orbit determination process involves two main elements: the spacecraft trajectory and the observations (Milani and Gronchi, 2010). The trajectory can be defined as the solution of the following non-linear differential equation (Tapley et al., 2004):

$$\dot{\mathbf{X}} = F(\mathbf{X}, t) \tag{3.1}$$

with the initial condition $\mathbf{X}(t_k) = \mathbf{X}_k$. $\mathbf{X}$ is the m-dimensional state vector which includes the spacecraft position and velocity vectors along with all the model parameters to estimate and $\mathbf{X}_k$ is the state vector at the time t_k. The observation equation which relates the l-dimensional vector of the observations $\mathbf{Y}_i$ to the model parameters has a non-linear expression as well:

$$\mathbf{Y}_i = G(\mathbf{X}_i, t_i) + \epsilon_{\mathbf{i}} \qquad i = 1, \ldots n \tag{3.2}$$

where $\epsilon_{\mathbf{i}}$ are the observation errors. Generally at each time the number of observations is less than the unknown parameters to estimate ($l < m$) and therefore it is necessary to have observations at different times so that $l \times n >> m$.

The orbit determination problem can be simplified by linearizing the dynamic and observational equations. A Taylor series expansion truncated at first order can be used if a reference trajectory $\mathbf{X}^*$ is available and sufficiently close to the true

trajectory $\mathbf{X}$ in the time interval of interest. The non-linear problem expressed in equations 3.1 and 3.2 can then be described by a set of linear equations:

$$\dot{\mathbf{x}}(t) = A(t)\mathbf{x}(t) \tag{3.3}$$

$$\mathbf{y_i} = \tilde{H}_i\mathbf{x_i} + \epsilon_\mathbf{i} \qquad i = 1,\ldots,n \tag{3.4}$$

where $A(t) = \left[\frac{\partial F(t)}{\partial \mathbf{X}(t)}\right]^*$ and $\tilde{H}_i = \left[\frac{\partial G(t)}{\partial \mathbf{X}(t)}\right]^*_i$ are the partial derivatives matrices of the model and observation equations with respect to the estimated parameters computed on the reference trajectory $\mathbf{X}^*$.

$\mathbf{x}(t) = \mathbf{X}(t) - \mathbf{X}^*(t)$ is the m-dimensional vector that describes the deviation of the state from the reference trajectory and

$\mathbf{y_i}(t) = \mathbf{Y_i}(t) - \mathbf{Y_i^*}(t)$ is the n-dimensional observation deviation vector also called residual vector and representing the difference between the observed observables (actual data) and the computed observables calculated on the basis of the reference trajectory.

The general solution of equation 3.3 can be expressed as:

$$\mathbf{x}(t) = \Phi(t, t_k)\mathbf{x}(t_k) \tag{3.5}$$

$\Phi(t, t_k)$ is the state transition matrix and allows mapping the state vector at any time t with respect to a reference state at time t_k. It can be determined by solving the differential equation

$$\dot{\Phi}(t, t_k) = A(t)\Phi(t, t_k) \tag{3.6}$$

with the initial condition $\Phi(t_k, t_k) = I$ (Tapley et al., 2004).

Using equation 3.5 the residuals $\mathbf{y_i}(t)$ that are generally computed at different times can be all expressed in terms of the deviation of the state $\mathbf{x}_i$ computed at the same time thus reducing the number of unknowns from $m \times n$ to m:

$$\begin{aligned} \mathbf{y}_1 &= \tilde{H}_1\Phi(t_1, t_k)\mathbf{x}_k + \epsilon_1 \\ \mathbf{y}_2 &= \tilde{H}_2\Phi(t_2, t_k)\mathbf{x}_k + \epsilon_2 \\ &\vdots \\ \mathbf{y}_n &= \tilde{H}_n\Phi(t_n, t_k)\mathbf{x}_k + \epsilon_n \end{aligned} \tag{3.7}$$

The observation equation assumes then the following simplified expression:

$$\mathbf{y} = H\mathbf{x} + \epsilon \qquad (3.8)$$

where

$$\mathbf{y} \equiv \begin{bmatrix} \begin{bmatrix} y_{11} \\ \vdots \\ y_{1l} \end{bmatrix} \\ \vdots \\ \begin{bmatrix} y_{n1} \\ \vdots \\ y_{nl} \end{bmatrix} \end{bmatrix} \quad ; \quad H \equiv \begin{bmatrix} \tilde{H}_1 \Phi(t_1, t_k) \\ \vdots \\ \tilde{H}_n \Phi(t_n, t_k) \end{bmatrix} \quad ; \quad \epsilon \equiv \begin{bmatrix} \begin{bmatrix} \epsilon_{11} \\ \vdots \\ \epsilon_{1l} \end{bmatrix} \\ \vdots \\ \begin{bmatrix} \epsilon_{n1} \\ \vdots \\ \epsilon_{nl} \end{bmatrix} \end{bmatrix} \qquad (3.9)$$

The problem is however still undetermined because there are $p = l \times n$ observables and $p + m$ unknowns that are the m components of the state vector and the p components of the error vector ϵ. A possible solution comes from the least square method that provides us with conditions on the p observation errors allowing a solution for the m state variables x at the time t_k. Due to the fact that we are dealing with a linearized problem, the least square method will have to be applied recursively in order to reach convergence.

The least square method was first proposed by Gauss (1809) and is based on the estimation of the state $\mathbf{x}$ that minimizes a given cost index. The most logical choice for the cost index is the sum of the squares of the residuals. This prevents the possibility that contribution with opposite signs will cancel out since it can vanish only if all the elements of the residuals vector are identically zero. We also define a weighting matrix W that accounts for the different accuracy of each observation. It has usually the form of a diagonal matrix which means that the observations are

not time-correlated but this is not a necessary condition:

$$W = \begin{bmatrix} \begin{bmatrix} w_{11} & & \\ & \ddots & \\ & & w_{1l} \end{bmatrix} & & \\ & \ddots & \\ & & \begin{bmatrix} w_{n1} & & \\ & \ddots & \\ & & w_{nl} \end{bmatrix} \end{bmatrix} \tag{3.10}$$

The weighting matrix is computed by inverting the covariance matrix of the observations: $W = P^{-1}$. Therefore a higher weight reflects a better measurement confidence and make the solution more sensitive to the information content of that data.

The cost function to minimize is then:

$$J(\mathbf{x}) = \frac{1}{2}\epsilon^{\mathbf{T}}W\epsilon \tag{3.11}$$

By substituting the expression of the residuals in eq. 3.8 into 3.11 yields:

$$J(\mathbf{x}) = \frac{1}{2}(\mathbf{y} - H\mathbf{x_k})^T W(\mathbf{y} - H\mathbf{x}) \tag{3.12}$$

To minimize the cost function we impose that its first derivative with respect to $\mathbf{x}$ is null:

$$\frac{\partial J}{\partial \mathbf{x}} = 0 = -(\mathbf{y} - H\mathbf{x})^T H = -H^T(\mathbf{y} - H\mathbf{x}) \tag{3.13}$$

By rearranging eq. 3.13 we obtain:

$$(H^T W H)\hat{\mathbf{x}} = H^T W\mathbf{y} \tag{3.14}$$

If $(H^T W H)$ is positive definite the best estimate of $\mathbf{x}$ is then:

$$\hat{\mathbf{x}} = (H^T W H)^{-1} H^T W\mathbf{y} \tag{3.15}$$

The above formulation does not take into account any available a priori information on the estimated parameters. For common orbit determination problems an a priori knowledge of the model parameters is always present. It may come from

physical constraints, as the results of other experiments, or from previous solutions. If we indicate with an overbar the a priori information, eq. 3.15 become:

$$\hat{\mathbf{x}} = \Gamma_x^0 (H^T W \mathbf{y} + \bar{W}_x \bar{\mathbf{x}}) \tag{3.16}$$

where

$$\Gamma_x^0 = \Lambda^{-1} = (H^T W H + \bar{W}_x)^{-1} \tag{3.17}$$

Matrix Λ is called the information matrix. Matrix Γ_x^0 is related to the accuracy in the estimate of $\hat{\mathbf{x}}$ and represents the estimated parameters covariance matrix if W is properly selected. In fact overestimating the accuracy of the observations can result in a too optimistic estimate of the parameters in terms of their associated covariance. However in the case of white gaussian noise the observations can be weighted by taking the variance of the post fit residuals which should represent their actual accuracy thus avoiding any bias in the solution. $\bar{W}_x = \bar{P}_x^{-1}$ is the weighting matrix of the a priori information that are considered as additional observations. If the parameters are excessively constrained by too small uncertainties associated with the a priori information the resulting solution may be driven too much by them without representing the real data information content. The form in equation 3.16 is usually referred to as the normal equation and the matrix $H^T W H$ in eq. 3.17 is called the normal matrix.

One of the advantages of using a priori information is that the inclusion of $\bar{P}_x$ in the information matrix can reduce its ill-conditioning thus improving the inversion process. Moreover the constraints posed by a priori information can prevent the solution from walking away during the iteration process. At the beginning of the orbit determination process the initial conditions $\mathbf{X}^*(t_0)$ are set such that $\bar{P}_0$ reflects their accuracy and $\bar{\mathbf{x}}_0 = 0$. In the subsequent iterations $\bar{\mathbf{x}}_0$ is selected to maintain the sum $\mathbf{X}_0^* + \bar{\mathbf{x}}_0$ constant. At each iteration the estimated state deviation is added to the initial condition vector:

$$(\mathbf{X}_0^*)_n = (\mathbf{X}_0^*)_{n-1} + \hat{\mathbf{x}}_{\mathbf{n-1}} \tag{3.18}$$

Using 3.18 it is possible to determine $\bar{\mathbf{x}}_0$ at each iteration in such a way that the a priori values of the state parameters are kept constant:

$$(\bar{\mathbf{x}}_0)_n = (\bar{\mathbf{x}}_0)_{n-1} - \hat{\mathbf{x}}_{\mathbf{n-1}} \tag{3.19}$$

The Square-root formulation

The inversion of the information matrix in the normal formulation (eq 3.14) can pose numerical problems if it is ill-conditioned. The condition number C of a matrix A can be defined as follows (Lawson and Hanson, 1974):

$$C(A) = \gamma_{max}/\gamma_{min} \tag{3.20}$$

where γ_{max} is the maximum eigenvalue of A and γ_{min} is the minimum eigenvalue. In base 10 arithmetic with l significant digits, numerical difficulties with matrix inversion may arise when $C(A) \rightarrow 10^l$. Unfortunately, in the orbit determination problems at hand, this is often the case. For this reason a numerically superior method, the square-root formulation, has been implemented in the orbit determination software to overcame problems due to the inversion of the information matrix. This formulation, described by Moyer (1971) utilizes the Householder transformations to convert the matrix $H^T W H + \bar{P}^{-1}$ into the triangular matrix R whose order is the same of $H^T W H + \bar{P}^{-1}$. The parameters estimates will then require the inversion of R instead of $H^T W H + \bar{P}^{-1}$. The condition number of R is exactly the square root of that of $H^T W H + \bar{P}^{-1}$ thus giving less numerical error in the inversion process.

The QR factorization of the information matrix allows obtaining the solution in terms of the square-root of the information matrix with the advantage of inverting an upper triangular matrix. The QR decomposition uses a series of Householder orthogonal transformations to decompose a $m \times n$ matrix into an an orthogonal matrix Q and an upper triangular matrix R. The latter can be easily inverted by using backward substitution or singular value decomposition methods. Given that the square root of a matrix A is defined as $A = A^{\frac{T}{2}} A^{\frac{1}{2}}$, the square root of the information matrix can be written in terms of the matrices Q and R as follows:

$$\Lambda^{\frac{1}{2}} = \left[\begin{array}{c} W^{\frac{1}{2}} H \\ \hline \bar{W}_x^{\frac{1}{2}} \end{array} \right] = Q_x R_x \tag{3.21}$$

To obtain the Least-Squares solution the residuals **y** and the a-priori solution $\bar{\text{x}}$

must be transformed accordingly pre-multiplying by Q_x^T, obtaining:

$$R_z = Q_x^T \left[\frac{W^{\frac{1}{2}}\mathbf{y}}{\bar{W}_x^{\frac{1}{2}}\bar{\mathbf{x}}} \right] \tag{3.22}$$

The solution vector and the covariance matrix will then be simply given by:

$$\hat{\mathbf{x}} = R_x^{-1} R_z \quad \Gamma_x^0 = \Lambda^{-1} = R_x^{-1} R_x^{-T} \tag{3.23}$$

Consider parameters

The constant parameters on which the dynamical model is based are not always accurately known. However, the error associated with their values used in the model can be taken into account. Consider parameters are used to accomplish this job. To take into account also the consider parameters they are included in the generalized state vector. The state transition matrix will also include the partial derivatives of the observables with respect to the consider parameters. Let us suppose to have an a priori estimate of the state vector $\bar{\mathbf{x}}$ and the consider parameters vector $\bar{\mathbf{c}}$.

$$\mathbf{z} = \begin{bmatrix} \mathbf{x} \\ \mathbf{c} \end{bmatrix} \quad \tilde{\mathbf{y}} = \begin{bmatrix} y \\ \bar{\mathbf{x}} \\ \bar{\mathbf{c}} \end{bmatrix} \quad H_z = \begin{bmatrix} H_x & H_c \\ I & 0 \\ 0 & I \end{bmatrix} \quad \tilde{\epsilon} = \begin{bmatrix} \epsilon \\ \eta \\ \beta \end{bmatrix} \tag{3.24}$$

where H_c is the consider parameters mapping matrix. η and β are the error associated with the a priori values of the state vector $\bar{\mathbf{x}}$ and consider parameters $\bar{c}$

and have the following properties (Tapley et al., 2004):

$$E[\eta] = E[\beta] = 0$$

$$E[\eta\eta^{\mathbf{T}}] = \bar{P}_x$$

$$E[\beta\beta^{\mathbf{T}}] = \bar{P}_{cc} \tag{3.25}$$

$$E[\eta\epsilon^{\mathbf{T}}] = E[\beta\epsilon^{\mathbf{T}}] = 0$$

$$E[\eta\beta^{\mathbf{T}}] = \bar{P}_{xc}$$

The cost index to minimize is then:

$$J = \frac{1}{2}\tilde{\epsilon}\tilde{R}^{-1}\tilde{\epsilon}^T \tag{3.26}$$

where

$$\tilde{R} = \begin{bmatrix} R & 0 & 0 \\ 0 & \bar{P}_x & \bar{P}_{xc} \\ 0 & \bar{P}_{cx} & \bar{P}_{cc} \end{bmatrix} \qquad \tilde{R}^{-1} = \begin{bmatrix} R^{-1} & 0 & 0 \\ 0 & \bar{M}_x & \bar{M}_{xc} \\ 0 & \bar{M}_{cx} & \bar{M}_{cc} \end{bmatrix} \tag{3.27}$$

is the extended a priori observation error covariance matrix and the corresponding weighting matrix.

The corresponding solution is then:

$$\begin{bmatrix} (H_x^T R^{-1} H_x + \bar{M}_x) & (H_x^T R^{-1} H_c + \bar{M}_{xc}) \\ (H_c^T R^{-1} H_x + \bar{M}_{cx}) & (H_c^T R^{-1} H_c + \bar{M}_{cc}) \end{bmatrix} \begin{bmatrix} \hat{\mathbf{x}} \\ \hat{\mathbf{c}} \end{bmatrix} = \begin{bmatrix} H_x^T R^{-1} y + \bar{M}_x\bar{x} + \bar{M}_{xc}\bar{c} \\ H_c^T R^{-1} y + \bar{M}_{cx}\bar{x} + \bar{M}_{cc}\bar{c} \end{bmatrix}$$

or, in a more compact form:

$$\begin{bmatrix} M_{xx} & M_{xc} \\ M_{cx} & M_{cc} \end{bmatrix} \begin{bmatrix} \hat{\mathbf{x}} \\ \hat{\mathbf{c}} \end{bmatrix} = \begin{bmatrix} N_x \\ N_c \end{bmatrix} \tag{3.28}$$

The estimate of the state vector $\hat{x}$ is obtained by choosing not to compute $\hat{\mathbf{c}}$ and P_{cc} but to fix them at their a priori value $\bar{\mathbf{c}}$ and $\bar{P}_{cc}$ respectively. The final solution is then:

$$\hat{\mathbf{x}} = P_x N_x + S_{xc}\bar{\mathbf{c}} \tag{3.29}$$

with the associated covariance matrix

$$\begin{bmatrix} P_{xx} & P_{xc} \\ P_{cx} & P_{cc} \end{bmatrix} \tag{3.30}$$

where:

- $P_x = M_{xx}^{-1}$

- $S_{xc} = -M_{xx}^{-1}M_{xc}$

- $P_{xx} = P_x + S_{xc}\bar{P}_{cc}S_{xc}^T$

- $P_{xc} = S_{xc}\bar{P}_{cc}$

- $P_{cx} = P_{xc}^T$

- $P_{cc} = \bar{P}_{cc}$

The matrix S_{xc} is the sensitivity matrix and describes how the best estimate of the state variables vector is affected by the consider parameters.

3.1.2   The multi arc approach

The determination of the gravity field of the Saturnian satellites is usually carried out using data from multiple flybys. In principle, it would be possible to consider the spacecraft trajectory between these flybys as a single orbit, thus estimating only one spacecraft state vector. However, two consecutive flybys are usually months apart in the most favorable condition. The spacecraft dynamics during this period cannot be determined with the required accuracy mainly due to difficulties in modeling complex non-gravitational interactions (solar radiation pressure, maneuvers) (Milani and Gronchi, 2010). In essence there is no single deterministic model able to reliably capture the entire complexity of the phenomenon of non gravitational perturbations (Somenzi, 2006).

The multi arc approach allows overcoming this problem by dividing the space-craft orbit into different arcs of non-overlapping time intervals. This approach results in an over-parameterization of the problem with six additional parameters (the spacecraft initial conditions) for each arc. In this way each arc is independent from the others because the spacecraft orbit propagation depends only on its own initial conditions. However model parameters which do not vary with time and are common to all arcs can be estimated more accurately by using data from different arcs. The estimated parameters vector is then divided into a vector of local parameters and a vector of global parameters. The first one includes the spacecraft state vector and other dynamical model parameters peculiar of a particular arc (e.g. atmospheric drag for a low altitude flyby). The second one is the vector of the parameters common to all arcs such as the mass and the gravitational harmonics of the body under investigation.

The implementation of the multi arc method relies essentially on the correct construction of the design and weight matrices. Once accomplished this task, the least square filtering is performed using the same method described in section 3.1.1. Four groups of parameters can be generally defined:

- $\mathbf{x}^k = \begin{bmatrix} x_1^k & \cdots & x_{n_k}^k \end{bmatrix}^T$ is the vector of the n_k local parameters in the k-th arc

- $\mathbf{g} = \begin{bmatrix} g_1 & \cdots & g_n \end{bmatrix}^T$ is the vector of the n_g global parameters

- $\mathbf{c}^k = \begin{bmatrix} c_1^k & \cdots & c_{m_k}^k \end{bmatrix}^T$ is the vector of the m_k local consider parameters in the k-th arc

- $\mathbf{c} = \begin{bmatrix} c_1 & \cdots & c_m \end{bmatrix}^T$ is the vector of the m_c global consider parameters

In general n_k and m_k are different for each arc. The vector of solve-for paramters

x and the vector of consider parameters **z** have n and m elements respectively:

$$
\mathbf{x} = \begin{bmatrix} \mathbf{x}^1 \\ \vdots \\ \mathbf{x}^N \\ \mathbf{g} \end{bmatrix} \qquad \mathbf{z} = \begin{bmatrix} \mathbf{c}^1 \\ \vdots \\ \mathbf{c}^N \\ \mathbf{c} \end{bmatrix}
\tag{3.31}
$$

$$
n = n_g + \sum_{k=1}^{N} n_k \qquad m = m_c + \sum_{k=1}^{N} m_k
$$

By defining as y_i^k the i-th residual in the k-th arc and l_k the total number of observables in that arc, the residuals vector **y** has l elements:

$$
\mathbf{y} = \begin{bmatrix} \mathbf{y}^{(1)} \\ \vdots \\ \mathbf{y}^{(N)} \end{bmatrix}
\tag{3.32}
$$

$$
l = \sum_{k=1}^{N} l_k
$$

where $\mathbf{y}^k = \begin{bmatrix} y_1^k & \cdots & y_{l_k}^k \end{bmatrix}^T$

The partial derivatives of one arc with respect to local parameters of the other arcs are zero by definition. Thus the mapping matrices of solve-for and consider parameters H_x and H_c assume the following V-like block structure:

$$
H_x = \begin{bmatrix} H_{\mathbf{x}}^{(\mathbf{l}_1)} & \cdots & \mathbf{0} & H_{\mathbf{x}}^{(\mathbf{g}_1)} \\ \vdots & \ddots & \vdots & \vdots \\ \mathbf{0} & \cdots & H_{\mathbf{x}}^{(\mathbf{l}_N)} & H_{\mathbf{x}}^{(\mathbf{g}_N)} \end{bmatrix}
\tag{3.33}
$$

$$H_c = \begin{bmatrix} H_{\mathbf{c}}^{(\mathbf{l}_1)} & \cdots & \mathbf{0} & H_{\mathbf{c}}^{(\mathbf{g}_1)} \\ \vdots & \ddots & \vdots & \vdots \\ \mathbf{0} & \cdots & H_{\mathbf{c}}^{(\mathbf{l}_N)} & H_{\mathbf{c}}^{(\mathbf{g}_N)} \end{bmatrix} \tag{3.34}$$

where the matrices that appear in the above expressions are respectively:

- $H_{\mathbf{x}}^{(\mathbf{l}_k)}$ is the $l_k \times n_k$ mapping matrix of k-th arc observables with respect to local parameters.

- $H_{\mathbf{x}}^{(\mathbf{g}_k)}$ is the $l_k \times n_g$ mapping matrix of k-th arc observables with respect to global parameters.

- $H_{\mathbf{c}}^{(\mathbf{l}_k)}$ is the $l_k \times m_k$ mapping matrix of k-th arc observables with respect to local consider parameters.

- $H_{\mathbf{c}}^{(\mathbf{g}_k)}$ is the $l_k \times m_g$ mapping matrix of k-th arc observables with respect to global consider parameters.

The weighting matrix of the k-th arc assume the following expression:

$$W^k = \begin{bmatrix} w_1^k & \cdots & 0 \\ \vdots & \ddots & \vdots \\ 0 & \cdots & w_{l_k}^k \end{bmatrix} = \begin{bmatrix} \frac{1}{(\sigma_1^k)^2} & \cdots & 0 \\ \vdots & \ddots & \vdots \\ 0 & \cdots & \frac{1}{(\sigma_{l_k}^k)^2} \end{bmatrix} \tag{3.35}$$

$w_i^k = \frac{1}{(\sigma_j^k)^2}$ is the weight associated to the i-th observable in the k-th arc and σ_i^k is the standard deviation of the observable. Since the observations in one arc are assumed to be independent from those of the other arcs the weighting matrix has a block-diagonal structure:

$$W = \begin{bmatrix} W^1 & \cdots & 0 \\ \vdots & \ddots & \vdots \\ 0 & \cdots & W^{(N)} \end{bmatrix} \tag{3.36}$$

A priori values and their covariances can be included in the multiarc formulation. In principle it would be possible to consider cross-correlations between local parameters of different arcs. However since the multiarc approach is used to try to absorb un-modeled phenomena by over-parameterizing the problem the inclusion of cross-correlation between different arcs would invalidate this purpose. Therefore a priori covariance matrices are defined on an arc-by-arc basis. The a priori covariance of each arc $\tilde{\Gamma}^k_{x|c}$ can be a full symmetric matrix. Global and local parameters can have an a priori correlation while local parameters of different arcs are always uncorrelated from an a-priori point of view.

3.2 Observables

The most commonly used methods for high precision orbit determination are based on the transmission of radio signals. Radio tracking systems can provide information about distance, velocity and angular position of a spacecraft. Cassini navigation is accomplished mainly using range and range rate measurements while during a target approach phase, onboard optical images may be used to provide a direct measurement of the spacecraft position relative to the target body. The range observables are essentially a measurement of the signal one way or two-way light time. According to the notation in figure 3.1 the spacecraft topocentric slant range can be approximately expressed in terms of the one-way light time τ as $\rho = \tau c$ with c being the speed of light. The time derivative of the range is the range rate, often referred to as Doppler, which can be expressed approximately as $\dot{\rho} = c\left(1 - f_R/f_T\right)$ where f_R and f_T are respectively the received and transmitted frequency (Thornton and Border, 2000).

The following sections will give an overview of range and Doppler characteristics along with a description of the main error sources affecting this type of data.

3.2.1 Range observables

Range observables are based on the measurement of the propagation time of an electromagnetic wave traveling at the speed of light. To avoid clock synchronization issues the most used type of range measurement is the two-way coherent ranging. The uplink carrier phase is modulated by a ranging signal consisting of a series of discrete sines or square tones. A phase locked loop within the space-
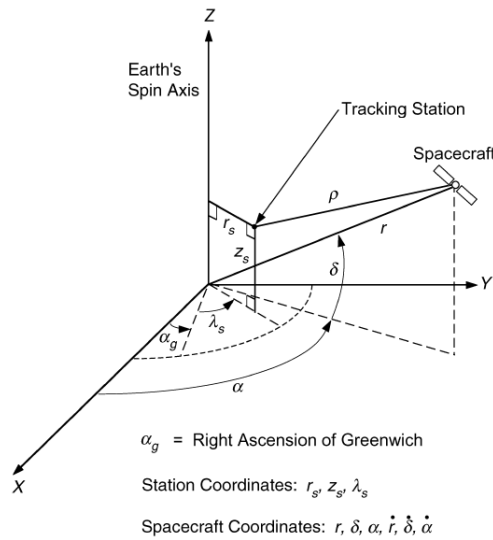
Figure 3.1: Spacecraft and station coordinates (Thornton and Border, 2000)

craft transponder locks on the uplink signal and coherently transmits back a phase modulated downlink carrier. The word coherent means that the downlink signal is coherent in phase with the uplink but translated in frequency of a given ratio (see table 3.1). Two-way ranging is preferred over one-way ranging because the latter relies on the synchronization between the station and the spacecraft clock whose lack directly translates into an error on the measured delay.

Uplink Band	Downlink Band	Transponding Ratio
S	S	240/221
S	X	880/221
X	X	880/749
X	Ka	3344/749

Table 3.1: Spacecraft Turnaround Ratio

The actual measurement is obtained by sending a ranging signal to the spacecraft and measuring the phase difference between the transmitted and received signals that gives information about the Round Trip Light Time. This difference is

measured in units of phase called range units (RUs). Their value depends on the highest ranging signal frequency and is currently about 28 cm (Thornton and Border, 2000).

Let us consider a modulation $A\cos\omega t$. The modulation received at time t will be:

$$B\cos\omega\left(t - \frac{\rho_u + \rho_d}{v_g}\right) \tag{3.37}$$

where ρ_u and ρ_d are respectively the distances travelled by the signal on the uplink and downlink paths. v_g is the group velocity of the propagating wave that depends on the transmission media. By cross-correlating the uplink and downlink signal we get:

$$\eta = \frac{1}{T}\int_{t_0}^{t_0+T} A\cos\omega t B\cos\omega\left(t - \frac{\rho_u + \rho_d}{v_g}\right)dt \approx$$

$$\approx \frac{AB}{2}\cos\frac{\omega}{v_g}(\rho_u + \rho_d) \quad \text{if} \quad T >> \frac{1}{\omega} \tag{3.38}$$

$$\rho_u + \rho_d = \frac{v_g}{\omega}\left[\arccos\frac{2\eta}{AB} + 2\pi N\right] = \frac{\lambda}{2\pi}\arccos\frac{2\eta}{AB} + N\lambda \tag{3.39}$$

The determination of the ranging measurement has an ambiguity of an integer number of wavelengths $\lambda = 2\pi v_g/\omega$. Each ranging system uses a different technique to solve the phase ambiguity. The available methods are:

- Tone ranging system that employs a series of tones

- Code ranging system that employs Pseudo-Random codes

- Hybrid ranging system that combines both tone and code ranging properties

Here we give a brief description of the ranging system used by Cassini which is based on a series of tones that modulate the carrier. The highest frequency of the ranging signal is called range clock and is proportional to the carrier frequency by a rational number $\beta = \frac{221}{749}\cdot 2^{-7-R}$ at X-band. R is an integer number called the component number of the range clock. The other components of the ranging signal have a frequency half of its predecessor. The a priori knowledge of the delay (i.e. the a priori estimate of spacecraft trajectory) determines the lowest frequency component. For example, if the spacecraft position is known within 1000 km, a lower frequency component of about 100 KHz (λ = 300000 km) will be enough to resolve the ambiguity being its wavelength greater than the uncertainty in the position of the spacecraft. The higher frequency components set the maximum accuracy attainable by the ranging system. Typically a clock frequency of about 1 MHz is used

for deep-space navigation and has an average accuracy of ~ 3 m (typically, $1/100$ of the tone period).

One of the problems affecting every ranging system is the motion of the spacecraft during the integration. For a deep space probe the integration may last several minutes given the low SNR and during this time the distance travelled by the spacecraft can amount to thousands of kilometers. At the DSN stations the problem is solved with the Doppler rate aiding method. On ground, the spacecraft range rate is continuously measured. Therefore the phase of the replica of the transmitted tone stored on ground is advanced by an amount dictated by the measured range rate to take into account the spacecraft motion. The ranging system described above is known as sequential ranging and is currently used for Cassini navigation and radio science experiments.

3.2.2 Range-rate observables

The rate-of-change of range, or range-rate is obtained by measuring the Doppler frequency which is the frequency difference between the transmitted and received signals:

$$\dot{\rho} = \frac{f_R - f_T}{f_T}c = \frac{\Delta f}{f_T}c \tag{3.40}$$

Doppler measurements provide information on the spacecraft topocentric range rate. The measurement is obtained by mixing a replica of the uplink signal with the received downlink signal. A low-pass filter gives the difference between the uplink and downlink frequencies that is called the Doppler tone. The Doppler counter measures the integrated Doppler that represents the change in range of a spacecraft over a count time T_c. This is done by monitoring the phase change due to the spacecraft radial motion. The acquisition process is schematically displayed in figure 3.2.

The 1-way integrated Doppler can be expressed as:

$$\Delta\rho(T_c) = \int_t^{t+T_c} v_R dt = \mp\frac{c}{f_T}\int_t^{t+T_c} f_D dt \tag{3.41}$$

where v_R is the spacecraft radial velocity and f_D is the frequency of the Doppler tone. The last integral term represents the Doppler cycle count which is accumulated every count time T_c at the ground station. The count time can vary from 0.1 s to about half a day but typical count times have durations of 10-1000 s (Moyer, 2000). For interplanetary cruise phases longer count times are used while for en-
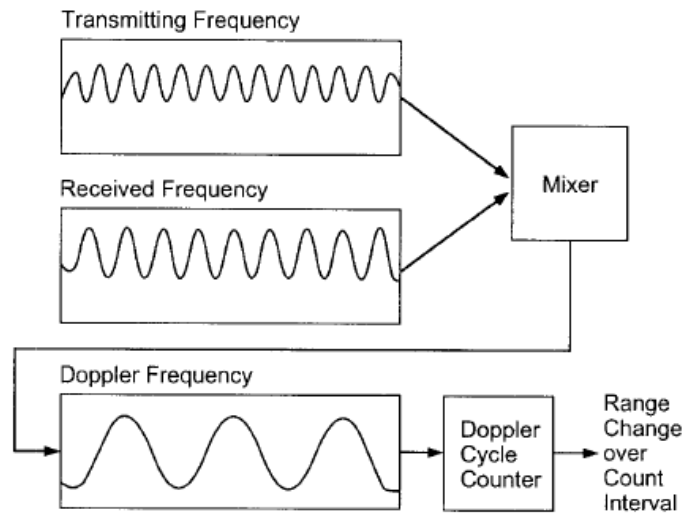
Figure 3.2: Doppler acquisition process (Thornton and Border, 2000)

counters with celestial bodies, like Saturn satellites flybys, count times of about 10-60 s are more often used. The time tag T of a Doppler observable is the midpoint of the interval count time T_c.

3.2.3   Error sources

The attainable accuracy of range and Doppler measurements is highly dependent on several error sources. There are delays introduced by the electronic instrumentation and errors due to the frequency instability of local oscillators. Moreover the signal propagation is affected by the transmission medias that introduce delays and dispersions. Finally, the non perfect knowledge of the tracking system geometry, which involves errors in the station location or in the Earth orientation have to be considered.

A widely used figure of merit to evaluate the stability of frequency standards in the time domain is the Allan deviation σ_y (Barnes et al., 1971):

$$\sigma_y^2(\tau) = \frac{1}{2}\langle(\hat{y}(t+\tau) - \hat{y}(t))^2\rangle \qquad (3.42)$$

where $\langle\rangle$ denotes an infinite time average and $\hat{y}$ is the average of the relative frequency shift $\Delta f/f$ over an integration time τ. This quantity is unaffected by linear frequency drifts and is thus particularly suitable to characterize the frequency sta-

bility of oscillators and radio systems. An overview of the main effects that can degrade Doppler measurement is given in table 3.2 for a Cassini-like transmission system in terms of Allan deviation.

Error source	Doppler (σ_y @ 1000s)
Frequency standard	$\sim 8 \times 10^{-16}$
Antenna mechanical	$\sim 2 \times 10^{-15}$
Ground electronics	$\sim 2 \times 10^{-16}$
Plasma phase scintillation	up to 8.1×10^{-14} at SEP=30°
Stochastic spacecraft motion	$\sim 2 \times 10^{-16}$
Receiver thermal noise	few $\times 10^{-16}$
Spacecraft transponder noise	10^{-16}
Tropospheric scintillation (calibrated)	$< 1.5 \times 10^{-15}$ to 3×10^{-15}

Table 3.2: Error sources in Cassini tracking system

Instrumental effects

The instrumental effects are due to several factors related to the particular instrumentation used for the measurement. The main effects are due to:

- **Thermal noise** which is due to the finite SNR on the radio link that causes phase fluctuations. This white phase noise depends on the lowest SNR element in the link that, in current two-way measurements, is the downlink path. This contribution, in terms of Allan deviation, can be written as:

$$\sigma_y = \frac{1}{2\pi f_0 \tau} \sqrt{\frac{3B}{(S/N_0)_{UL} + (S/N_0)_{DL}}} \tag{3.43}$$

  for 2-way Doppler measurements where B is the signal loop bandwidth, f_0 the carrier frequency and τ the integration time. A similar expression holds for the error on range measurements due to thermal noise but for the Cassini

telecommunication system they both have a negligible contribution to the overall noise budget.

- **Ground electronics** that is specifically designed to minimize the instabilities on the frequency and phase of the signal. In the current-era observations it is not a dominant noise source.

- **Spacecraft transponder noise** which is also a negligible contribution for Cassini transponders KEX and KAT. Their frequency stability in terms of Allan deviation was tested both on ground and in flight and resulted as low as 10^{-15} at 1000 s integration time.

- **Un-modeled spacecraft motion** that can directly introduce Doppler noise. These un-modeled motion can arise from different causes but can be independently determined by monitoring Cassini attitude and control system. For $f > 0.0001$ Hz the measured spectra show that Cassini motion has a negligible contribution to the overall Doppler data accuracy.

- **Antenna mechanical noise** causes a Doppler effect due to a time-dependent, un-modeled motion of the ground antenna's phase center, resulting in a change of the signal path length and, therefore, in an error in the signal phase estimation. It is mainly generated by the ground antenna's structure deformations under the effects of gravity, winds and temperature gradients. These kind of loads have to be estimated by means of experimental test campaigns or numerical analyses, and then compensated when possible.

Transmission media

The propagation of the signal through solar coronal plasma, and planetary atmospheres and ionospheres produces variations in its amplitude, phase and frequency. These variations can be frequency dependent (dispersive media) or independent (non-dispersive media). For interplanetary missions, effects on the signal amplitude are usually negligible in every condition thanks to the large SNR. The effects of the propagation media are thus a shift of the carrier frequency for Doppler measurements and a time varying group delay for range measurements.

The main non-dispersive effect is due to the Earth troposphere. In fact this medium is frequency independent up to 15 GHz. Therefore increasing the frequency of the signal does not increase the information about the delay or the possibility to calibrate it. The effect of the troposphere can result in a signal-path delay

of about 2 m at zenith and 20 m at 6° elevation angle (Thornton and Border, 2000). The tropospheric delay can be written as (Tapley et al., 2004):

$$\delta t = 10^{-6} \int N ds \tag{3.44}$$

where N is the refractivity:

$$N = (n-1)10^6 \tag{3.45}$$

with n being the refractive index. Refractivity is usually considered as the sum of a dry component N_d and a wet component N_w. About 95% of the total effect is made up by the dry component which can be modeled by assuming that the atmosphere is an ideal gas in hydrostatic equilibrium, thus requiring only the knowledge of the surface pressure. The dry component can be calculated to an accuracy of a few millimeters from measurements of surface barometric pressure (Thornton and Border, 2000). The wet component, on the other hand, is more difficult to model due to the instability of the water vapor density along the signal path. Local meteorogical data are able to provide an accuracy on the wet component of about 4 cm in the zenith direction (Elgered, 1992). The tropospheric delay is also dependent on the elevation angle of the viewing direction. Mapping functions are thus used to map the zenith effect at any elevation angle E. Using a simple mapping function, zenith delay measurement errors are magnified by approximately a factor $1/\sin E$, thus giving accuracies at 10° of elevation of about 6 cm. In order to obtain better accuracies, the total zenith delays have to be computed by means of other systems like the GPS calibration system or the Advanced Media Calibration System (AMC).

The GPS calibration system uses GPS data and the JPL GIPSY-OASIS II software to produce calibrations of the zenith troposphere delay at the DSN tracking stations. Users can then map the zenith calibrations to their lines of sight using appropriate elevation mapping functions. The accuracy of this calibration system depends strongly on the accuracy of the GPS orbit and clock parameters, which in turn depends on the quality and global distribution of the available GPS data from the ground tracking network (Bar-Sever et al., 2007).

The AMC system was developed specifically for Cassini radio science experiments. To this end an advanced water vapor radiometer (AWVR) was developed by JPL. AWVRs measure the thermal radio emissions of water vapor near a resonance at 22 GHz. The radio path delay is then inferred from these data using models and estimates of the atmospheric temperature and pressure. These are provided by a microwave temperature profiler that retrieves the vertical distribution

of atmospheric temperature along with surface sensors for temperature, pressure, and relative humidity, which add further constraints to the path delay retrieval processing. The ensemble of these sensors and models constitute the Advanced Media Calibration System which is able to provide improved calibrations of the wet tropospheric path delay.

The main dispersive media is the Earth's ionosphere, the portion of the Earth's atmosphere characterized by the presence of charged particles. The interplanetary plasma is also cause of dispersive propagation delays. Th ionosphere effect has a seasonal and diurnal modulation while the effect due to interplanetary plasma depends on the solar cycle and the Sun-Earth-Probe (SEP) angle. In fact the effect is greater near solar conjunction when the signal path is closer to the Sun. The effect of these dispersive media is dependent on the frequency and the total electron content along the signal path (Tapley et al., 2004):

$$\delta t = \frac{\alpha}{f^2} \tag{3.46}$$

where α is proportional to the TEC (total electron content) per unit area along the signal path. α is a positive term for group delays so a ranging code modulated on the carrier signal will experience a delay. It is instead negative for carrier phase.

Since the effect is frequency dependent, the use of a dual-frequency radio link, allow the complete cancellation of the induced delays. On Cassini it was originally implemented a multi-frequency system enabling simultaneous communication at X/X, X/Ka and Ka/Ka bands. This configuration allowed an almost complete cancellation of ionospheric and plasma noise (Tortora et al., 2004). However, in 2003, the KaT transponder suffered an unrecoverable malfunction that causes the loss of the Ka/Ka link. For this reason the accuracy achieved by Doppler data during the cruise was not available during the Saturnian tour.

Numerical noise

The numerical error affects the calculation of computed observables. It is caused by the fact that the JPL's OD software use the floating point arithmetic representation of numbers which means that numbers are represented with a finite number of digits. Every real number used in the process is thus affected by this kind of error which propagates when mathematical operations are applied to those numbers. The use of quadrupole precision representation of numbers can decrease this effect

but never cancel it. In the OD process the total numerical error in the computation of radiometric observables is mainly the sum of the effects of the rounding errors in the representation of times and distances.

Numerical noise is dependent upon the integration time and the epoch (being related to time representation used in OD codes). On range rate measurements it is inversely proportional to the Doppler count time T_c because the actual measurement is essentially computed as a range difference over a given count time T_c. The average numerical noise on Cassini Doppler X-band data at 60 s integration time in terms of Allan deviation amounts to about 3×10^{-14} which is a significant error source which put a lower limit in the achievable Doppler measurements accuracy (Zannoni and Tortora, 2012).

Chapter 4

Analysis methods

4.1 Dynamical model

The dynamical model used in our analyses accounts for several forces acting on the spacecraft. The gravitational forces act indifferently on all the bodies in the solar system and on the spacecraft. Forces of non-gravitational origin affect, instead, only the spacecraft motion. In this section we give a brief description of all the forces models used in the integration of Cassini trajectory during the flybys of Saturn system satellites. Mathematical details of the implementation of these models in the Orbit Determination Program (ODP) can be found in Ekelund et al. (1996) and Moyer (1971).

4.1.1 Gravitational forces

The gravitational perturbations include a variety of acceleration models to take into account all the possible dynamical effects acting on the spacecraft. The main contribution is the Newtonian n-body point mass acceleration from planets, Sun, and Moon whose orbital elements are retrieved from JPL's planetary ephemerides DE419. The gravitational acceleration acting on the center of mass of the spacecraft (p) is written with respect to the origin of the Solar System Barycenter reference frame (b):

$$\ddot{\vec{r}}_{bp}^{N} = -\frac{\mu_c}{r_{cp}^3}\vec{r}_{cp} - \sum_{i \neq PCB} \mu_i \left(\frac{\vec{r}_{ip}}{|r_{ip}|^3} + \frac{\vec{r}_{bi}}{r_{bi}^3} \right) \tag{4.1}$$

where c is the center of the i-th planet that is considered as a point mass.

Relativistic accelerations only caused by the Sun, Jupiter and Saturn are also taken into account and computed in the Solar System Barycenter reference frame.

The accelerations of the n-bodies are related to the relativistic parameters β and γ ($\beta = \gamma = 1$ in general relativity).

Of course, we also consider the Saturnian satellites Newtonian point mass accelerations and the accelerations caused by tides and Saturn rings. Gravity anomalies of any of the n-bodies due to the oblateness are modeled through the spherical harmonics representation of the gravity field. Finally, mass concentrations (mascons) can be added to the dynamical model and represented as flat disks or as points.

4.1.2 Tides

The JPL's Orbit Determination Program (ODP) allows the estimation of a variable gravity field only for planets but not for satellites. Therefore, in order to estimate a variable gravity field and the related degree-2 Love number (see section 2.4), a dedicated procedure was developed. Actually, the last version of the ODP incorporated the tides model but the dedicated code is still in use because it allows a better control of the mathematical model and the partial derivatives computation.

This procedure entails two fundamental steps. The first step is to compute the partial derivatives of the observables with respect to k_2. This can be accomplished by using quantities already computed in the ODP when only a static gravity field is used. Since the harmonic coefficients vary linearly with respect to the Love number k_2 (see equation 2.17), the partial derivative of the observable z with respect to k_2 can be easily expressed by applying the chain rule (see SOM Iess et al. (2012)):

$$\frac{\partial z}{\partial k_2} = \sum_m \frac{\partial z}{\partial C_{2m}} \frac{\partial C_{2m}}{\partial k_2} \tag{4.2}$$

The first term on the right side of the above equation is the partial derivative of the observable with respect to the gravity coefficient that includes both static and tidal contribution. It can be directly retrieved from the ODP provided that the dynamical model has been properly set-up with the coefficient total value. The remaining term can be easily computed by the model equations 2.17 and is a function of the satellite's mean anomaly at the time of the closest approach. Note that the Love model we are using assumes that the same quadrupole Love number is shared among all the coefficients. Therefore the actual partial derivative is computed as the sum of the three partials from J_2, C_{22} and S_{22} coefficients. The key point is that when the ODP integrates the variational equations to generate the spacecraft trajectory, the satellite degree-2 gravity model is represented by the total value of the coefficients

for the current arc. The gravity field is considered as constant during the time-span of integration, being its variations negligible. This is applicable in the case at hand where the duration of a typical flyby is small compared to the orbital period. Each data arc has a typical duration of about 24 hours centered on the closest approach. However data on the inbound and outbound are mainly used to better estimate the spacecraft state vector and are sensitive only to the point-mass gravity perturbations. Only data across the C/A bear information about the quadrupole coefficients.

Once the partial derivatives of the Love number are computed they must be included into the information matrix along with the partial derivatives for the static component of the gravity field coefficients. The latter are exactly equal to the partials of the total coefficients and are therefore directly available from the ODP:

$$\frac{\partial z}{\partial C_s} = \frac{\partial z}{\partial C_{tot}} \frac{\partial C_{tot}}{\partial C_s} = \frac{\partial z}{\partial C_{tot}} \tag{4.3}$$

Where C_s is the static gravity coefficient and C_{tot} is the total one. From equation 2.17 is straightforward to demonstrate that $\partial C_{tot}/\partial C_s = 1$.

Clearly, in order to successfully estimate k_2 is necessary to combine data from multiple flybys to detect a variation in the gravity field. Therefore a multi arc approach is used to combine the information matrix from each flyby. To perform this task a specific software has been developed to perform a least-square inversion with the gravity field coefficients and the Love number as global solve-for parameters. This software is written in Fortran 95/2003 and has been validated against the ODP. It allows estimating both the static part of the coefficients and the Love number in a single global fit. The filter uses an iterative weighted least-square model implemented by a batch square-root algorithm to improve the numerical stability (Racioppa, 2012).

4.1.3 Non-gravitational accelerations

Cassini spacecraft is subject to different kind of non-gravitational forces. The most important effect is due to the trajectory correction maneuvers used to variate the spacecraft orbit but our data arcs never include this kind of accelerations. Gravity flybys are also designed to avoid the presence, during the closest approach phase, of other kind of maneuvers. These include the unbalanced thrust from the attitude control system and the reaction wheels desaturation maneuvers. The main non-gravitational effects during gravity flybys are then due to the anisotropic ther-

mal emission of the RTGs, the solar radiation pressure and the atmospheric drag for Titan's flybys at altitudes lower than 1200 km.

The three on board RTG's provide power to the spacecraft through the decay of an isotope of plutonium (see section 1.1). The spacecraft bus is insulated from the RTG's thermal radiation through an insulating blanket. This produces an anisotropic thermal emission along the spacecraft +Z axis due to the radiation reflected by the blanket. Smaller but relevant accelerations are induced also along Cassini's X- and Y-axis due to the asymmetric spacing of the RTGs. In the Orbit determination software the effect of the RTG's is modeled as an exponential decaying acceleration (Ekelund et al., 1996):

$$\overrightarrow{a} = M_R(A_r\hat{\mathbf{Z}} + A_x\hat{\mathbf{X}} + A_y\hat{\mathbf{Y}})e^{-\alpha\Delta t} \tag{4.4}$$

where the exponential scale factor α is $2.5^{-10}s^{-1}$ and M_R is the ratio between the spacecraft mass at the beginning of the mission and the current mass.

The non-gravitational acceleration due to the solar radiation pressure is caused by the transfer of energy and momentum from the solar photons to the impact surface. The amount of the induced acceleration depends on what fraction of the incident radiation is absorbed or reflected. The thermo-optic coefficients of the exposed surfaces are difficult to infer and this make the acceleration due to the solar radiation pressure somewhat uncertain. However, during tracking periods, the main reflecting surface is given by the HGA which accounts for 90% of the total frontal area. HGA thermo-optical coefficients were measured during ground tests and their variations during the mission are inferred from temperature measurements from two sensors mounted on the HGA back side (Clark, 2008). The mathematical formulation of the solar radiation pressure in the orbit determination software can be found in Ekelund et al. (1996).

For Titan's flybys with a closest approach altitude as low as 1200 km the effect of the atmospheric drag cannot be neglected. Titan's atmosphere is depicted as a scale height driven exponential model. In this model the atmospheric density ρ is a function of altitude and time (Ekelund et al., 1996):

$$\rho_j = \rho_{ij}exp[(h_i - h)/H_{ij}] \tag{4.5}$$

where:

- h_i is the reference altitude (km).

- t_j is the reference epoch, either in solar local time or absolute time.

- ρ_{ij} is the atmosphere density at epoch t_j and altitude h_i (g/cm^3).

- H_{ij} is the exponential scale height at time t_j for the i-th layer of the atmosphere (km).

- h is the spacecraft altitude (km).

- t is the current epoch.

The resulting acceleration acting on the spacecraft is given by:

$$\vec{a}_{\mathbf{D}} = \frac{\rho V_b^2}{2m} C_D \left(\sum_i A_i \right) \hat{V}_b \tag{4.6}$$

where:

- ρ is the atmospheric density.

- C_D is the drag coefficient.

- A_i is the cross-sectional area of spacecraft component i in the direction of the body-fixed spacecraft velocity vector.

- m is the mass of the spacecraft.

- V_b is the magnitude of the body-fixed spacecraft velocity.

- $\hat{V}_b$ is the direction of the body-fixed spacecraft velocity.

4.1.4 Gravity from topography

As described in section 2.5 spherical harmonics expansion of topography can be used to constraint the gravity field estimate. This approach can be particularly useful when the small amount of data available prevents the estimation of the gravity coefficients with the required accuracy.

Let us consider a case in which the available data allow only a good estimation of the quadrupole field without giving access to the degree-3 harmonics. If a spherical harmonics expansion of the topography is available, it can be used to directly derive the degree-3 gravity coefficients using equation 2.26. However, in order to take into account the presence of isostatic compensation, we need to estimate the

compensation factor C. Even in this case there is an evident advantage in the use of this approach because the number of estimated parameters is reduced (from 7 degree-3 gravity coefficients to 1 compensation factor).

The estimate of the compensation factor C is carried out using an approach similar to the one described in section 4.1.2. As in that case we need to compute the partial derivatives of the observables with respect to C. This can be easily accomplished by using the chain rule:

$$\frac{\partial z}{\partial C} = \sum_{l,m} \frac{\partial z}{\partial C_{lm}} \frac{\partial C_{lm}}{\partial C} \tag{4.7}$$

where $\partial z/\partial C_{lm}$ are quantities directly available from the ODP and $\partial C_{lm}/\partial C$ can be computed from 2.26.

These partial derivatives are then included in the information matrix which is inverted using the Oracle filter (Racioppa, 2012). Once the compensation factor has been estimated, it is used to calculate the resulting gravity coefficients starting from the spherical harmonics expansion of topography. The updated trajectory of the spacecraft will be computed taking into account the full gravity model. This process is iterated until convergence is attained.

4.2   The ephemerides update process

The ephemerides of the Saturnian satellites are provided by Cassini Navigation Team in the form of a set of Chebyshev polynomials whose coefficients are given typically every 18 days. The state of the satellite relative to the Saturn system barycenter is then retrieved by interpolating the Chebyshev coefficients (Jacobson, 2003) at the required time. Satellite ephemerides are generated starting from a time history of the bodies' positions and velocities. These are obtained by numerically integrating the equations of motion of the bodies using the classical Cowell method, a special perturbations technique (Peters, 1981).

The ephemerides of the Saturnian satellites have a different level of accuracy for each body. For example, Titan ephemerides are more accurate than that of Enceladus thanks to the greater number of observations available. Moreover, the ephemerides of a certain body, are less accurate when propagated far ahead of the last observation time. For this reasons it is often necessary to update the ephemerides of a given body when a new flyby is performed, to correctly fit the data. In addition, when more flybys spanning over a quite long time (typically 3-4 years for Cassini

tour) are combined together in a multi arc solution, the ephemerides update process is required to ensure that the body under examination is on a coherent trajectory.

The ephemerides are updated by first estimating a new initial state (position, velocity and mass) at a time that is before the first flyby. On the basis of this new set of initial conditions the ephemerides of all Saturn system bodies are integrated and used to generate new satellite ephemerides files.

4.3   The estimation process

The estimate of the model parameters of interest is accomplished through a data fitting process. In this process raw data are compared to the data predicted using the initial estimated spacecraft trajectory and model parameters are estimated in order to compute a trajectory that minimize the difference between the predicted data and the realized observations. The data fitting process consists in the sequential execution of the following steps:

1. An initial trajectory is integrated on the basis of a given initial state (position, velocity and model parameters) in a time interval when real observations are available.

2. The state transition matrix is computed to relate state changes at different times to changes of the initial state or other dynamical model parameters (satellites ephemerides, gravity)

3. Predicted observables are computed at the same times of the real observations.

4. The partial derivatives of the observables with respect to the spacecraft state and model parameters are computed. These are combined with the weighting matrix and the state transition matrix to produce the information matrix (see section 3.1)

5. The real observations are corrected with proper calibrations to take into account the transmission media effects. The residuals are then computed as the difference between the calibrated observables and the computed ones.

6. A square-root filter approach is applied to retrieve the estimate of the parameters of interest that minimize the residuals.

7. The resulting initial state estimate may be used to recursively run the process from step 1 until convergence is reached when the adjustment of the trajectory (i.e the state vector) approaches zero.

4.4 Analysis setup

4.4.1 Data selection

Data used in our analyses includes 2-way and 3-way Doppler, both X/X and X/Ka and two-way X/X range data. When available, 2-way is always preferred over 3-way to reduce the errors in clock synchronization between the transmitting and receiving station. X/Ka data are preferred over X/X band due to the smaller sensitivity of Ka band downlink to plasma noise.

Range data are used only in the analysis of non-gravity flybys. In these cases range data are in fact useful to better constraint the spacecraft position and estimate the ephemerides of the Saturn system. However, the use of range data poses some problems. In fact, a range observable, being an absolute measure of distance, is sensitive to measurement biases. The accuracy of the current system is limited by the knowledge of delays through station and spacecraft electronics that can be up to 2 m (Thornton and Border, 2000). This bias is usually unknown and has to be estimated to correctly fit range data. Therefore a range bias for each pass has to be added to the list of estimated parameters. On gravity flybys this may lead to a bias in the estimated gravity coefficients if the estimated bias is absorbing other effects other than the instrumental one. Therefore, during gravity flybys, range data are neglected since Doppler data can provide all the required information content.

4.4.2 Data correction

Data corrections are applied to account for the phase and time delay due to the dispersive media and the troposphere. When available, data from the AMC (Advanced Media Calibration) system are used to best compensate for the tropospheric dry and wet delay, otherwise standard calibrations (TSAC) based on ground measurements are used.

4.4.3 Data weighting

Data weighting of Doppler measurements is performed grouping the observables on a pass-by-pass basis. In the assumption of white noise, weights are assigned to each pass through an iterative process in order to be compatible with the rms value of the post fit residuals for that pass. By defining the Sum of Square of the residuals as follows:

$$SOS = \mathbf{y}^T W \mathbf{y} = \sum_{k=1}^{N} \frac{y_k^o - y_k^c}{\sigma_k^2} \tag{4.8}$$

where $\mathbf{y}$ is the residuals vector and σ_k the observables variance, this procedure allows obtaining an SOS that is equal, or a bit less, than the number of observables. The SOS is kept lower than the number of points such that data are never over weighted. In this way the estimated uncertainties are never underestimated.

4.4.4 Data filtering

Data filtering is performed by means of the JPL's ODP software (Orbit Determination Program). The software minimize, in the least square sense, the Doppler residuals (computed observables minus observed observables) in order to solve for the model parameters of interests. The filter operates in the batch mode, and uses the square root formulation in order to minimize the bad-conditioned information matrix. Given a set of solve-for parameters, the estimation process provides central values of these quantities along with their uncertainties in the form of a full covariance matrix, obtained by inversion of the information matrix. Given the limited amount of data, not all the model parameters can be estimated. However the ODP allows putting model constants as consider parameters. This means that the uncertainties of their modeled values are taken into account in the data reduction process although the values themselves are not solved-for.

Chapter 5

Data analysis and results

This chapter presents all the analyses carried out for the estimate of the gravity fields of the main saturnian satellites. It is organized as follows: section 5.1 describes the measurement of the eccentricity tides on Titan. Part of the content of this section was published in June 2012 on the journal Science (Iess et al., 2012). Section 5.2 covers all the aspects related to the estimate of the gravity field of Enceladus and the detection of a mass anomaly at the South Pole as the origin of the observed geysers. Section 5.3 presents the first estimates of Dione's quadruple gravity field determined during the first Cassini flyby dedicated to gravity science in December 2011.

5.1   Titan

While all previous analyses were carried out assuming a purely static gravity field (Iess et al., 2010), the non-negligible eccentricity of Titan's orbit implies that the tidal stress from Saturn varies along the orbit, causing a change also in the quadrupole coefficients. Considering only the first order terms in the eccentricity, and in the hypothesis of null obliquity and synchronous rotation, the gravity field harmonics can be modeled as the sum of a static and a periodic part proportional to the orbital eccentricity and the dynamical Love number k_2 (see section 2.4). The analysis carried out in this thesis aimed to determine the tidal Love number k_2, a crucial quantity to infer the presence of a global ocean under Titan's surface. The results were published in 2012 on Science in a paper entitled "The Tides of Titan" (Iess et al., 2012).

The gravity field of Titan and its tidal variations were inferred from range-rate

measurements. These measurements were obtained during the six flybys that have been dedicated so far to gravity science. According to the numbering used by the Cassini project they were T11, T22, T33, T45, T68 and T74 (see table 5.1 for their characteristics). These flybys were favorably distributed along Titan's orbit to increase the sensitivity to the variations of the gravity field induced by Saturn tidal stresses. Two of them were near Titan pericenter (T33, T45), three of them near Titan apocenter (T11, T22, T74) and T68 was in quadrature at nearly 90° of mean anomaly (Fig. 5.1).
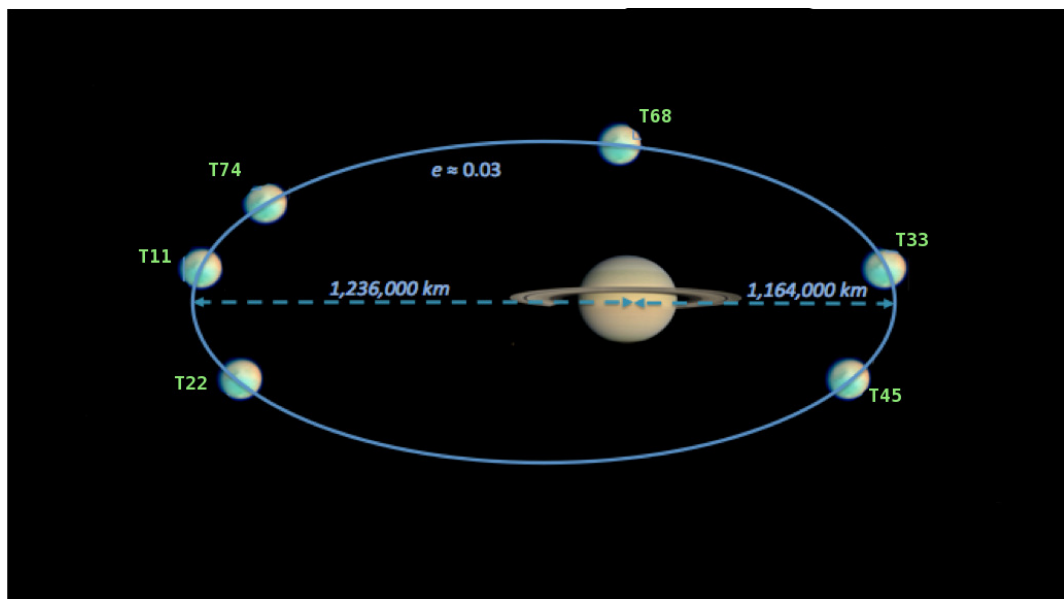
Figure 5.1: The distribution of Titan's flybys along its orbit around Saturn

	T11	T22	T33	T45	T68	T74
Date	27-FEB-2006 08:25:18 ET	28-DEC-2006 10:06:27 ET	29-JUN-2007 17:00:51 ET	31-JUL-2008 02:14:16 ET	20-MAY-2010 03:25:26 ET	18-FEB-2011 16:05:17 ET
Mean Anom.	172.7°	197.3°	15.1°	346.2°	81.8°	15.9°
SEP	147.0°	131.9°	44.6°	29.4°	118.8°	133.0°
Altitude (km)	1812	1297	1933	1614	1399	3652
Latitude	-0.2°	40.6°	8.4°	-43.5°	-49.0°	0.7°
Longitude	250.6°	0.0°	63.1°	162.7°	241.5°	113.4°
Inclination	179.7°	67.3°	8.4°	122.3°	130.9°	179.3°
N. of points	1134	1292	1435	1303	1911	1627
Noise (mm/s)	0.021	0.023	0.028	0.074	0.037	0.071

Table 5.1: Geometric and orbital parameters of the six flybys used for Titan gravity and eccentricity tides determination

5.1.1 Analysis setup

The data set included 2-way and 3-way Doppler, both X/X and X/Ka. When available, 2-way data were preferred over 3-way and X/Ka was preferred over X/X band due to the smaller sensitivity of Ka band downlink to plasma noise. Data from the Advanced Media Calibration (AMC) system were used to correct the Doppler data from the time delay due to the troposphere. Data were weighted by grouping the observables on a pass-by-pass basis according to the scheme presented in section 4.4.3.

The dynamical model included a variety of forces acting on the spacecraft. The primary forces are the gravitational accelerations due to Titan's GM and the higher degree field harmonics. The degree of the field used in the orbital solution was selected as the lowest capable of fitting the data without producing signatures at closest approach. A 3x3 field resulted adequate. However, we also produced a 4x4 field with the goal of assessing the stability of the estimated parameters to changes in the solution rank. The reference solution for Titan's static gravity uses a full 3x3 harmonic expansion, for a total of 12 coefficients (J_2, C_{21}, S_{21}, C_{22}, S_{22}, J_3, C_{31}, S_{31}, C_{32}, S_{32}, C_{33}, S_{33}).The a priori uncertainties used for the gravity coefficients were on average two orders of magnitude larger than the formal uncertainties at the end of the estimation process. Increasing by one order of magnitude the a priori uncertainties of all estimated parameters did not change the solution in any statistically significant way. Since the obliquity of Titan is well determined by SAR data, tighter constraints were used for C_{21} and S_{21} in order to allow an obliquity variation three times larger than the estimated value of 0.3° (Persi del Marmo et al., 2007). The adopted rotational model is shown in table 5.2. Nominal values of the largest gravity coefficients (J_2 and C_{22}) follow from the assumption of hydrostatic equilibrium while all the other coefficients were initially set to zero. However, the hydrostatic constraint ($J_2/C_{22} = 10/3$) was never used.

$$\alpha_0 = 38.°242151 - 0.°04229T$$

$$\delta_0 = 83.°768864 - 0.°004444T$$

$$W_0 = 189.°861726 + 22.°5769791934d$$

Table 5.2: Titan's rotational model adopted for the gravity solutions. T is given in Julian centuries (of 36525 days) past J2000 and d are days past J2000.

The variable part of the gravity field (i.e the Love number k_2) was estimated according to the model presented in section 2.4 and the procedure described in 4.1.2. For Titan, the peak-to-peak variations of the gravity coefficients J_2 and C_{22} can be respectively of 4% and 7% if k_2 is supposed to be 0.4. If its values is increased to 0.6 the relative variations are up to 6% and 10.5% respectively. Since the estimated uncertainties of the static gravity coefficients is much lower (in the order of 1% for J_2 and 0.2% for C_{22} (Iess et al., 2010)) a good sensitivity at least to the real part of the Love number was expected. Because the flybys and their geometry were selected to maximize the sensitivity to the real part of k_2, the estimate of imaginary part was more difficult and led to less stable solutions than for the real counterpart.

The dynamical model included also other forces such as the point mass accelerations due to all the other bodies of the solar system (mainly Saturn and its satellites, the Sun and Jupiter), the RTGs (Radio-isotope Thermoelectric Generators) thrust, the solar radiation pressure and relativistic effects. Moreover we had to take into account the effect of Titan's atmosphere for flybys whose altitude at closest approach was lower than 1350 km. No drag acceleration was thus accounted for in all flybys except T22. A 2-layers exponential model was used to describe the atmosphere for T22 flyby. The orbit determination software allows the estimation of the atmospheric density ρ_0 at a reference height and the scale heights H_1 and H_2 of the first and second layer. The time dependence of the density was neglected (for a detailed description of the model see section 4.1.3). Since it is not possible to estimate the density profile from the few Doppler data of a flyby, only the reference density was solved-for while the two scale heights were taken as consider parameters. The estimated density value is not absolute measurement because it is dependent on the assumed value of the Cassini drag coefficient (the drag acceleration is proportional to the ρC_D product).

The solution also included the estimate of Cassini's state vector (position and velocity) for each arc. Initial conditions for the spacecraft orbit were based on the navigation reconstruction of the Cassini trajectory during the flyby arc. A-priori constraints for the Cassini state vector were set as a diagonal covariance matrix with a 1-sigma uncertainty of 1 km in position (for each component) and 0.3 mm/s in velocity (for each component), consistent with the nominal navigation accuracy. Moreover, as the orbit of Titan is not perfectly known, the satellite state vector at a reference epoch (18-JAN-2004 00:00:00 UTC) was also estimated. The adjustment of Titan's orbit and mass required also an update of the ephemerides of the major Saturn's satellites in the same iteration.

Parameter	Value	Uncertainty
GM	$8.9781397 \times 10^3 km^3/s^2$	3.00×10^{-3}
J_2	3.33×10^{-5}	2.91×10^{-5}
C_{22}	1.00×10^{-5}	8.40×10^{-6}
S_{22}	0.00	1.50×10^{-6}
C_{21}	0.00	1.20×10^{-7}
S_{21}	0.00	7.90×10^{-7}
J_3	0.00	3.40×10^{-5}
C_{31}	0.00	1.40×10^{-5}
S_{31}	0.00	1.40×10^{-5}
C_{32}	0.00	4.40×10^{-6}
S_{32}	0.00	4.40×10^{-6}
C_{33}	0.00	1.80×10^{-6}
S_{33}	0.00	1.80×10^{-6}
$Re(k_2)$	0.5	0.5
$Im(k_2)$	0.0	1.0
ρ_0	$7.0 \times 10^{-15} g/cm^3$	$1.0 \times 10^{-12} g/cm^3$
H_1	86 km	10 km
H_2	101 km	20 km

Table 5.3: A priori values and uncertainties for Titan gravity model

Clearly, in order to maximize the sensitivity to the tidal variations of the gravity field, all data were processed in a single global fit estimating a full degree-3 static gravity field and both real and imaginary part of the Love number.

5.1.2 Results

Different solutions were produced to assess the stability of the estimated values of k_2 to variations in the solution rank. In the Science paper only two of them were presented and are also reported here along with other cases analyzed. In summary the following cases have been analyzed:

1. Sol1: Estimate of full degree-3 gravity field and $\Re(k_2)$ only

2. Sol2: Estimate of full degree-4 gravity field and $\Re(k_2)$ only

3. Sol3: Estimate of full degree-3 + J4 gravity field and $\Re(k_2)$ only

4. Sol4: Estimate of full degree-3 gravity field $\Re(k_2)$ and $\Im(k_2)$

5. Sol5: Estimate of full degree-4 gravity field $\Re(k_2)$ and $\Im(k_2)$

Convergence was always attained after three iterations but five iterations were performed to verify the stability of the solution. The resulting post-fit residuals show no signatures and a RMS value compatible with the expected noise level for each flyby. Figures 5.2 and 5.3 report the post-fit residuals only for Sol1 but for the other cases the residuals look almost the same.

(a) T11 (b) T22
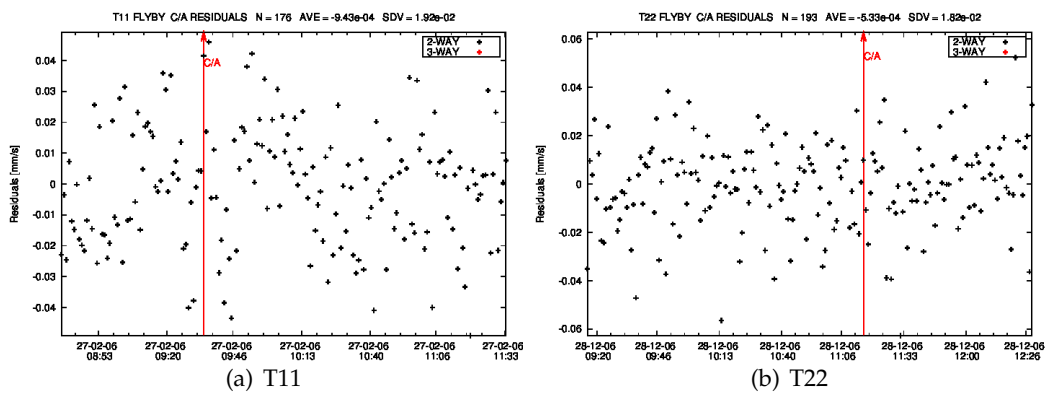
Figure 5.2: Post-fit Doppler residuals for Titan's gravity flybys T11 and T22
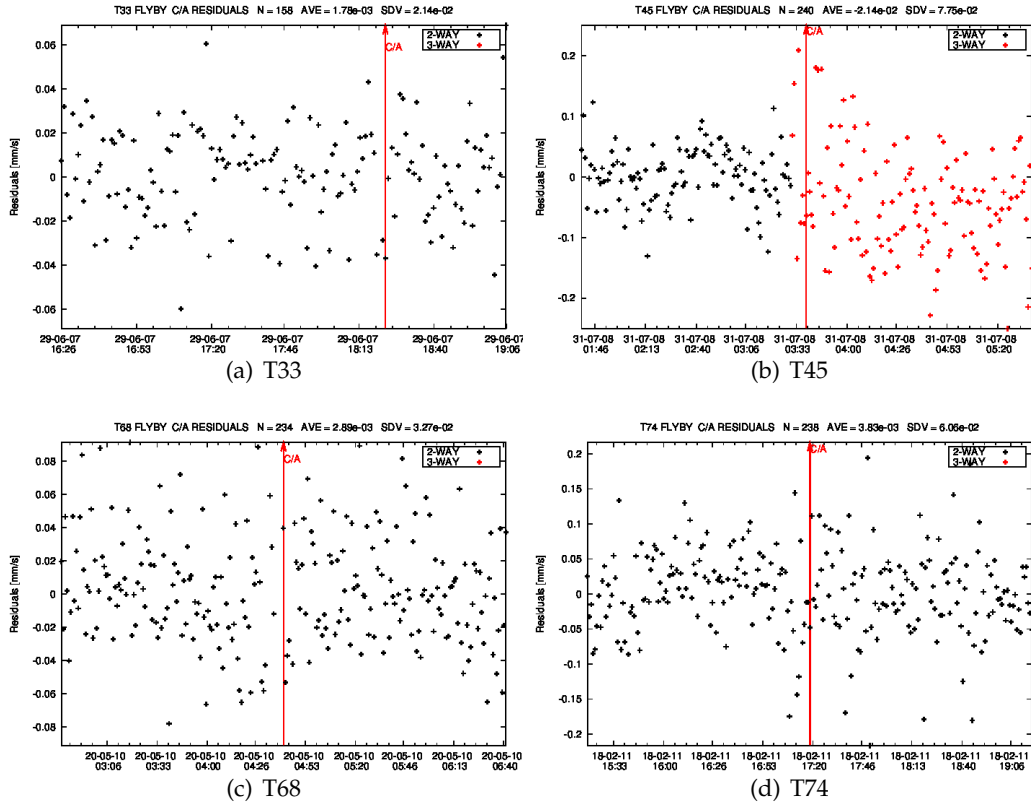
Figure 5.3: Post-fit Doppler residuals for Titan's gravity flybys T33, T45, T68 and T74

The estimates of the tidal Love number k_2 are stable despite of the variations in the dynamical model and in the solution rank. In particular all the estimated values of $\Re(k_2)$ are compatible at 1-sigma level and are determined with a good relative accuracy of about 12%. Because the flybys and their geometry were selected to maximize the sensitivity to the real part of k_2, the estimate of $\Im(k_2)$ is less stable than the real counterpart. The determination of $\Im(k_2)$ is not enough reliable given the different central values and high uncertainties even though $\Im(k_2)$ is compatible with zero at 2-sigma level (see table 5.4).

A 3x3 gravity field is adequate to correctly fit the data without producing any signature in the post-fit residuals. The inclusion of higher degree field do not modify significantly the quadrupole and the degree-3 terms. In table 5.5 are reported the estimated gravity coefficients for cases 1 to 3.

An interesting analysis was carried out to demonstrate that the inclusion of a variable gravity field improve the previous solution and is fully justified even if a

Solution	$\Re(k_2)$	$\Im(k_2)$
Sol1	0.589 ± 0.075	-
Sol2	0.670 ± 0.090	-
Sol3	0.646 ± 0.076	-
Sol4	0.596 ± 0.075	0.280 ± 0.105
Sol5	0.677 ± 0.092	-0.095 ± 0.143

Table 5.4: Titan's Love number estimates using different gravity models

solution with only a static gravity field is still possible. In the first Titan's gravity analysis (Iess et al., 2010), the even distribution of the four flybys between pericenter and apocenter of Titan's orbit averaged out the effects of eccentricity tides in the combined solution. Therefore it was estimated only a static gravity field. However we cannot exclude that the effect of variable gravity was absorbed by other parameters thus resulting in a bias of some components of the solution (e.g. the spacecraft state vector). The dynamical model adopted in the current analysis is clearly more appropriate given the strong geophysical arguments militating in favor of a significant time-dependent gravity (driven by the large eccentricity). The inclusion of k_2 in the solution does not corrupt the solution in any way and its only effect could be an increasing in the gravity field uncertainties. However, the inclusion of two new flybys compensated this effect. Table 5.6 reports the rms of the post-fit residuals around closest approaches of the gravity flybys when different constraints are applied. We analyzed the following cases:

1. Estimate of 3x3 static field (k_2=0), Titan and Cassini state vectors.

2. Estimate of 3x3 static field (k_2=0). Titan and Cassini SV constrained to the values of Sol1

3. Estimate of 3x3 static field (k_2=0) and Titan SV. Cassini SV constrained to the values of Sol1

4. Estimate of 3x3 static field (k_2=0) and Cassini SV. Titan SV constrained to the values of Sol1 If k_2 is forced to zero the residuals of most passes near closest approach have a quite significant degradation, with an increase of about 7%.

Gravity coefficients	Value $\pm 1\sigma (\times 10^6)$		
	Sol1	Sol2	Sol3
J2	33.599 ± 0.332	34.227 ± 0.477	33.726 ± 0.332
C21	0.186 ± 0.101	0.125 ± 0.111	0.089 ± 0.104
S21	0.664 ± 0.246	0.816 ± 0.351	0.522 ± 0.249
C22	10.121 ± 0.029	10.263 ± 0.069	10.137 ± 0.029
S22	0.194 ± 0.033	0.111 ± 0.055	0.159 ± 0.034
J3	-1.097 ± 0.606	-1.635 ± 0.838	-0.765 ± 0.611
C31	0.595 ± 0.174	0.681 ± 0.207	0.809 ± 0.176
S31	1.062 ± 0.286	-0.073 ± 0.475	0.110 ± 0.364
C32	0.275 ± 0.069	0.150 ± 0.125	-0.021 ± 0.098
S32	0.072 ± 0.048	0.104 ± 0.114	0.095 ± 0.048
C33	-0.222 ± 0.008	-0.221 ± 0.016	-0.211 ± 0.008
S33	-0.264 ± 0.011	-0.232 ± 0.016	-0.238 ± 0.013
J4	-	2.043 ± 0.759	2.985 ± 0.683
C41	-	0.175 ± 0.203	-
S41	-	0.033 ± 0.250	-
C42	-	0.059 ± 0.080	-
S42	-	0.093 ± 0.058	-
C43	-	0.026 ± 0.015	-
S43	-	0.008 ± 0.020	-
C44	-	-0.007 ± 0.002	-
S44	-	-0.014 ± 0.002	-

Table 5.5: Titan's gravity field from different solutions

Any other constraint always results in large signatures in the residuals and therefore in large post-fit RMS values.

± 30 min	Sol1	Case 1	Case 2	Case 3	Case 4
T 11	2.15	2.30	6.31	6.03	2.43
T 22	1.84	1.88	8.15	7.11	2.28
T 33	2.05	2.20	11.5	5.70	2.39
T 45	8.67	8.93	9.93	19.5	13.3
T 68	3.68	3.55	11.0	7.47	5.87
T 74	6.78	7.20	8.21	13.6	8.11

Table 5.6: RMS value of the residuals (in mm/s x 100) at +/-30 min from closest approach when different constraints are applied to the solution

5.1.3 Interpretation

The analysis carried out has confirmed that Titan is in a relaxed shape. The moment of Inertia factor, that we derived using the Radau-Darwin equation is 0.3431±0.0004 in Sol1 and 0.3438±0.0005 in Sol2. These values are perfectly compatible with previous determinations (Iess et al., 2010). Moreover the inclusion of a variable gravity field (i.e. a non.zero value of k_2) did not modify in any statistically significant way the degree-3 gravity field previously determined. The degree-3 geoid (Fig. 5.4) shows in fact the same global features that were present in the one published in 2010 (Iess et al., 2010). The degree-4 geoid (Fig. 5.5) has more deep depression and a higher variability range but also in this case the main features are confirmed. The errors associated with the good heights (Fig. 5.6) give an important indication on the degree of confidence we have reached at this point. Since most of the flybys were nearly equatorial the geoid is more accurate in this region. Nonetheless, the error in the polar regions is less than 2.5 meters. This value will probably be improved thanks to the upcoming Titan's gravity flyby that will sample the polar region areas. All the solutions we have derived provide consistent values of k_2 and gravity harmonics at 3-sigma for quadrupole gravity coefficients and 1-sigma
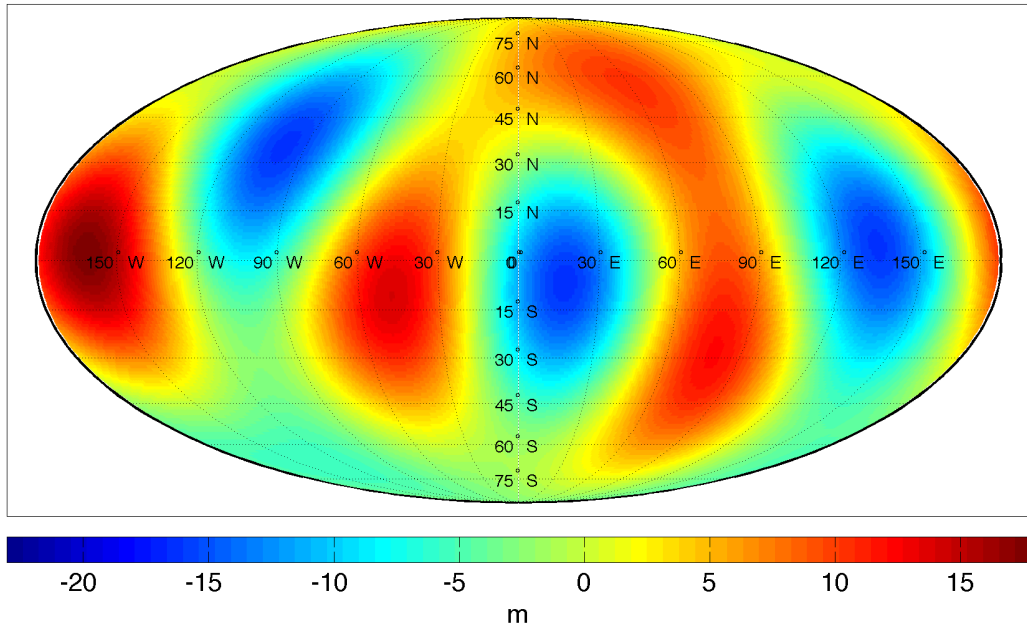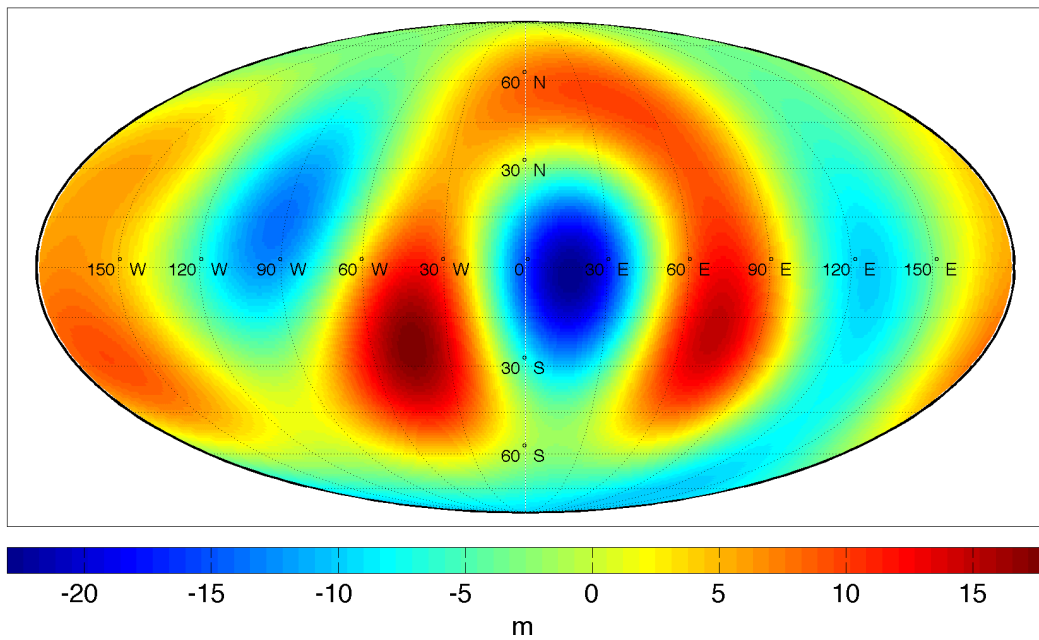
Figure 5.4: Titan's geoid heights for Sol1

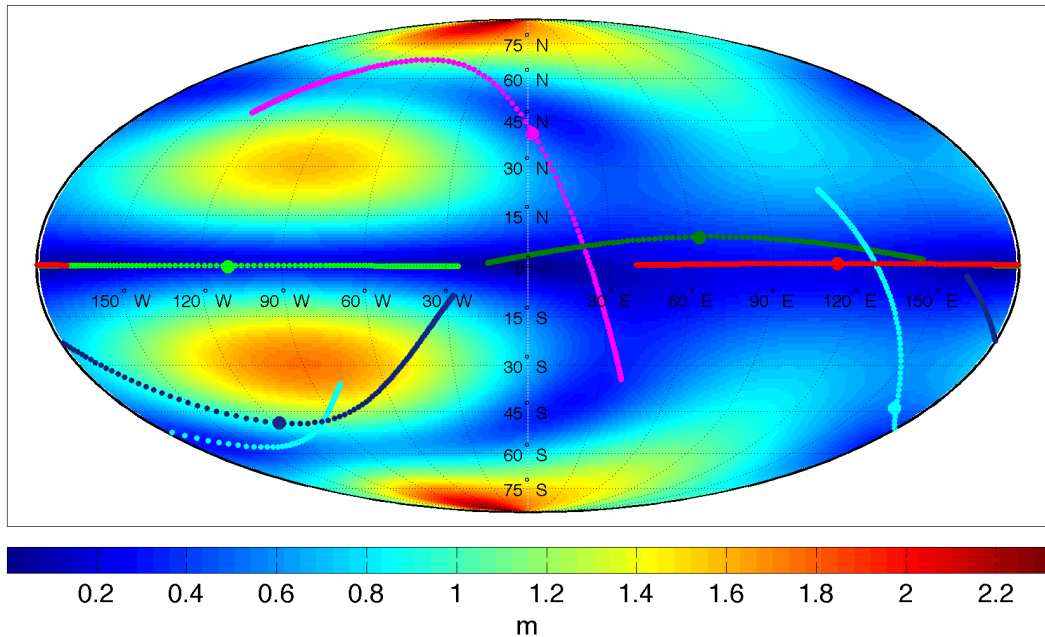**Figure 5.5:** Titan's geoid heights for Sol2

Figure 5.6: Titan's geoid heights error for Sol1

for k_2. A value of k_2 larger than 0.5 indicates that Titan is highly deformable over a time scale of the order of the orbital period. Previous analyses (Rappaport et al., 2008) expected a lower value for a silicate core and a subsurface ocean. The estimated value of k_2 lies within its physically likely range that for Titan goes from the purely elastic value (~ 0) to the perfectly hydrostatic value of about 1.0. According to our result the elastic value is clearly excluded since we are much closer to the hydrostatic one. This result is consistent with the presence of some global layer that deformates like a fluid under the stresses exerted by the tidal field on orbital timescales. This strongly suggest either the presence of a subsurface global ocean beneath the surface ice shell or the presence of a low viscosity deep interior. However, in order to explain the large value of k_2, a combination of the two effects have to be invoked.

5.2 Enceladus

The determination of Enceladus gravity plays a crucial role in the definition of its internal structure and can help in explaining the origin of the geysers that were observed at the South Pole. However, during the prime mission (2004-2008) Ence-

ladus was not selected as a primary objective for gravity observations and no flybys with tracking at closest approach, required for the determination of the quadrupole gravity field, were scheduled. The only data available were from the first Enceladus flyby in 2005 (named E0) when a small amount of range and Doppler X/X data were acquired before and after the encounter. These measurements led to the determination of Enceladus mass (Rappaport et al., 2007) with a significant improvement with respect to the results obtained by Voyager (Campbell and Anderson, 1989).

After the discovery, in 2006, (see section 1.4.1) of a plume ejecting vapor from fractures at the South Pole three flybys with tracking at C/A were scheduled for the equinox and solstice mission phases.

The first gravity flyby, E9, was specifically designed to detect the presence of gravity anomalies at the South Pole. Cassini, in fact, passed right under Enceladus South Pole at around 100 km altitude. The spacecraft was tracked in X- and Ka-band from the DSN stations with the closet approach over Madrid complex. The high Sun-Earth-Probe (SEP) angle along with the use of the Advanced Media Calibration System allowed obtaining low noise data that provided the first estimate of Enceladus quadrupole gravity field. However a single, highly inclined flyby did not allow a good determination of C22 and more data were required to obtain a better estimate.

Six months later the second gravity flyby, E12, was instead almost equatorial. In this case data quality was poorer due to the lower SEP angle. Moreover the C/A pass was tracked in 3-way mode from the DSN stations in Madrid and Goldstone. Despite of these limitations this low altitude flyby provided fundamental data to improve the gravity field estimation. The analysis of these data combined with data from E0 and E9 has revealed interesting characteristics of Enceladus gravity that will be discussed in the following sections. It is however important to underline that this analysis revealed a gravity field more complex than expected. A gravity model with at least a quadrupole field and a J_3 was in fact required to correctly fit the data of both flybys. In addition to the gravity flybys we also used data from other flybys not explicitly dedicated to gravity science. Among the 9 available flybys we selected those that had at least a tracking pass before and after Enceladus closest approach without having any maneuver between them that would be difficult to model. We therefore selected the flybys named E4, E5 and E7. Table 5.7 reports the main characteristic of the Enceladus flybys dedicated to gravity science.

	E0	E9	E12
Date	17-FEB-2005 03:31:33 ET	28-APR-2010 00:11:23 ET	30-NOV-2010 11:55:06 ET
SEP	142.8°	141.0°	53.7°
Altitude (km)	1176	100	48
Latitude	50.1°	-89.3°	61.8°
Longitude	119.2°	206.2°	307.3°
Inclination	50.1°	90.0°	-0.1°
N. of points	295	1494	831
Noise (mm/s)	0.031	0.032	0.044

Table 5.7: Geometric and orbital parameters of the three flybys used for Enceladus gravity determination

5.2.1 Model of Enceladus gravity field

Before the first flyby dedicated to gravity science in 2010 no information about Enceladus internal mass distribution was known. The presence of a geologically active region at the South Pole pointed towards the presence of some mass anomaly in that region, presumably a deposit of liquid water under the surface. Therefore a gravity field composed by at least a quadrupole component ad a north-south asymmetry (J_3) or a mass concentration (Mascon) under the South Pole was expected.

The quadrupole field of Enceladus is determined by the average tidal field exerted by Saturn and by the centrifugal field associated to the rotation about the polar axis (see section 2.2). The effects of these two perturbing fields on Enceladus are controlled by the tidal parameter q_t which is the ratio between Saturn tidal field and Enceladus surface gravity and the rotational parameter q_r which is the ratio between the centrifugal acceleration at the equator and surface gravity acceleration. For a satellite tidally locked like Enceladus these two parameters are related such that $q_t = -3q_r$. By assuming that the satellite is in hydrostatic equilibrium, in the principal axes frame J_2 and C_{22} (the only non-null quadrupole coefficients) are a function only of the fluid Love number k_f (cfr. eq. 2.12). The putative quadrupole

coefficients used as a priori values in the analysis are then computed by using a $k_f = 3/2$ (fluid body):

$$J_2 = \frac{5}{6}k_f q_r = 7.84 \times 10^{-3}$$
$$C_{22} = \frac{1}{4}k_f q_r = 2.35 \times 10^{-3}$$
(5.1)

Enceladus rotational state is defined according to the IAU reference frame definition for a synchronous rotating satellite. The spin axis is perpendicular to the orbital plane with the prime meridian defined by the eccentricity vector (i.e. by Saturn direction at pericenter). Right ascension and declination of the pole and longitude of the prime meridian are defined in table 5.8.

$$\alpha = 40.°577807 - 0.°0444741438T + 0.°000028\sin S1 - 0.°000001\sin S2$$
$$+0.°076554\sin S3 + 0.°037284\sin S4$$
$$\delta = 83.°537932 - 0.°0046159437T + 0.°000016\cos S1 + 0.°000001\cos S2$$
$$+0.°008612\cos S3 + 0.°004198\cos S4$$
$$W = 2.°266834 - 262.°7318982667d - 0.°249101\sin S1 - 0.°186661\sin S2$$
$$-0.°075831\sin S3 - 0.°037007\sin S4$$

Table 5.8: Enceladus rotational model adopted for the gravity solutions. T is given in Julian centuries (of 36525 days) past J2000 and d are days past J2000.

A priori uncertainties on the estimated parameters were set in order to avoid any constraint on the final solution that we wanted to be driven only by the data information content. However, due to the limited sensitivity to the pole and the prime meridian positions, coefficients C_{21} and S_{21} were constrained in order to allow a maximum obliquity of $1°$. The following equations were used to compute the a priori uncertainty on C_{21}, S_{21} and S_{22} given a maximum displacement angle σ_a from the position of the axes defined by the IAU reference frame.

$$\sigma_{C_{21}} = \sigma_a^2\sqrt{(C_{20} + 2C_{22})^2 + 16C_{22}^2} \tag{5.2}$$

$$\sigma_{S_{21}} = \sigma_a|C_{20} + 2C_{22}| \tag{5.3}$$

$$\sigma_{S_{22}} = \sigma_a(2\sqrt{2}C_{22}) \tag{5.4}$$

Different gravity models have been used depending on the number of flybys used for the analysis. In fact, when analyzing data from only one flyby, a gravity model composed by a pure quadrupole field was sufficient to correctly fit the data. When data from a second flyby were added, in order to obtain a good fit, a more complex model with at least a J_3 or a Mascon located at the South Pole was needed. Finally, when all flybys were used for the gravity estimation a model with a full degree-3 gravity field was required to fit coherently the whole data set. Table 5.9 shows all the a priori values and uncertainties used in the analysis.

In all the analyses we also estimated Enceladus GM and state vector. In fact, the limited amount of data available for the determination of its ephemerides and the perturbations exerted by Saturn and its rings during its 32 hours revolution, make Enceladus ephemerides quite uncertain. This uncertainty increase when propagating the ephemerides long time after the last observation. For this reason, in order to correctly fit the data, we had to update Enceladus ephemerides in the single arc analyses as well as in the multi arc ones.

5.2.2 Results

The data analysis of Enceladus flybys started soon after the first pass (E9) on April 2010. The first solution was then produced using only these data. When Cassini performed the other flyby (E12) these data were added to improve the estimated dynamical model. However, before producing a global solution, E12 was analyzed separately to obtain a first solution to use as a starting point in the combined one. The purpose of this work was to avoid the presence of un-modeled effects that, if not identified in the single arc solution, would be difficult to isolate in a global fit.

Single arc analyses

E9 and E12 were first analyzed separately to identify the best setup for the following multi arc analysis. In order to fit data from these flybys a gravity model made of a pure quadrupole was enough. Moreover, due to a lack of sensitivity, the coefficients C_{21} and S_{21} were not estimated and were considered always zero. The estimated parameters included also Cassini state vector and Enceladus' GM and state vector. The update of Enceladus' ephemerides was required to get a consistent solution. Data were weighted according to the scheme presented in section 4.4.3 on a pass-by-pass basis giving to each pass a weight that is proportional to

Parameter	Value ($\times 10^3$)	Uncertainty($\times 10^3$)
J_2	7.83	13.00
C_{22}	2.35	3.50
S_{22}	0.00	0.74
C_{21}	0.00	0.30
S_{21}	0.00	0.14
J_3	0.00	1.00
C_{31}	0.00	0.80
S_{31}	0.00	0.80
C_{32}	0.00	0.30
S_{32}	0.00	0.30
C_{33}	0.00	0.10
S_{33}	0.00	0.10
$GM_{Mascon}(km^3/s^2)$	0.00	0.10

Table 5.9: A priori values and uncertainties for Enceladus gravity model

the rms of the post-fit residuals of that pass. For the single arc estimation of E12 we used the updated Encleadus' ephemerides to exploit the information obtained from previous flybys.

Table 5.10 shows the results obtained for the different single arc analyses. For E9, J_2 is estimated with better accuracy than C_{22} due to the high inclination (almost polar) of the flyby. E12 confirmed the estimates of J_2 and significantly improved those of C_{22}.

Flyby	$J_2(\times 10^6)$	$C_{22}(\times 10^6)$	$S_{22}(\times 10^6)$	Correlation J_2/C_{22}
E9	5206.7 ± 111.9	919.9 ± 698.7	463.7 ± 259.0	-0.56
E12	5558.0 ± 134.7	1574.3 ± 56.6	-103.7 ± 38.2	-0.36

Table 5.10: Enceladus single arc gravity solutions

All the results are compatible at 2-sigma level (see figure 5.7) between each other and with the hydrostatic equilibrium condition represented by the red dashed line. Among the two gravity passes E12 has the best combination of geometry and data quality that allows a good sensitivity both to J_2 and C_{22}.

The post-fit residuals (Figures 5.8 and 5.9) do not show any signature at closest approach and the rms is compatible with the expected noise level given the SEP angle of each flyby.

The consistency of these results was further tested by combining all available data in a single global fit thus reducing the degree of freedom of the problem (see next section). In particular Enceladus was put on a coherent trajectory by estimating its state vector at the same epoch while in the single arc analyses its orbital elements vary from flyby to flyby. Nonetheless, the compatibility of the single arc solutions is a good indication of the appropriateness of the dynamical model used in the fit.

Multiarc analyses

Data from E9 and E12 were then combined along with data from E0 to retrieve a coherent gravity field capable of fitting all data at the same time. A first solution was produced using a gravity model made of a full-degree-2 and a J_3 (Sol1). A pure quadrupole gravity field was not adequate to obtain a good fit in a global solution and the addition of a J_3 was consistent from a geophysical point of view to model
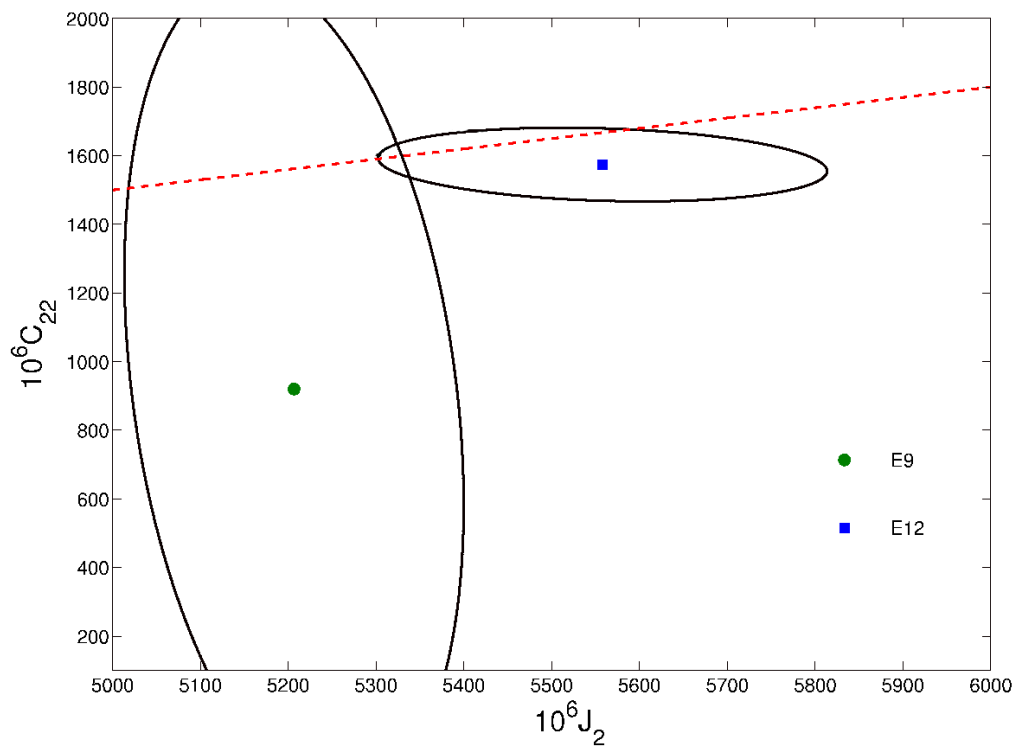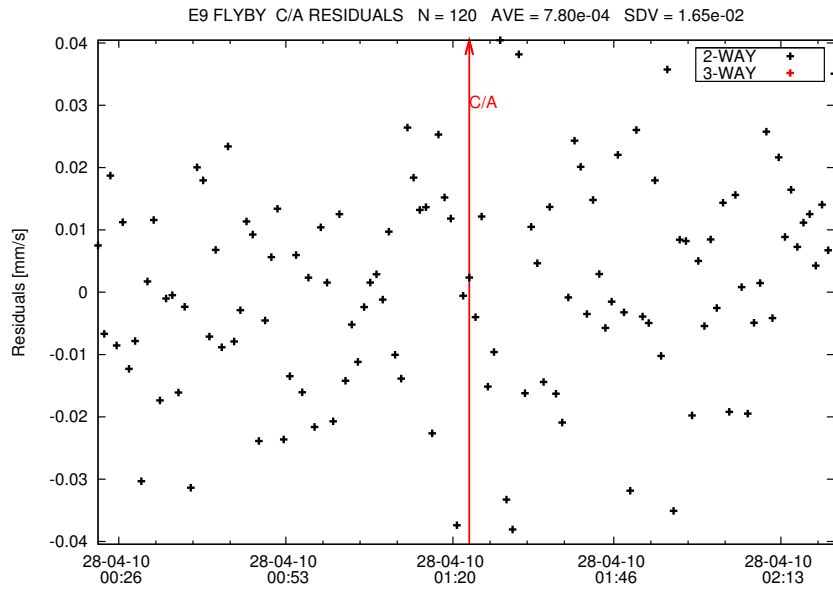
Figure 5.7: Enceladus J2-C22 2-sigma error ellipses

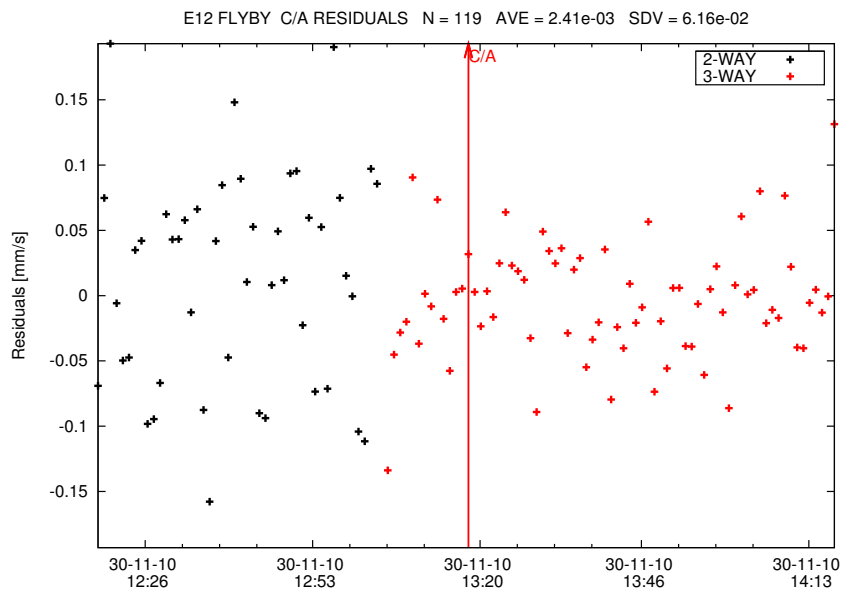**Figure 5.8:** X/Ka Doppler Post-fit Residuals for E9 single arc solution

Figure 5.9: X/Ka Doppler Post-fit Residuals for E12 single arc solution

the north-south asymmetry. Results are shown in table 5.11.

Degree	Order	Gravity coefficients	
n	m	$C_{nm}(\times 10^6)$	$S_{nm}(\times 10^6)$
2	0	-4887.7 $\pm$ 64.7	
2	1	-16.6 $\pm$ 7.2	256.5 $\pm$ 27.3
2	2	1430.6 $\pm$ 49.6	204.3 $\pm$ 9.7
3	0	404.3 $\pm$ 34.3	

Table 5.11: Enceladus multi arc gravity solutions based on E0, E9 and E12 data (Sol1)

In order to strengthen the results a second multi arc solution was produced (Sol2). In this case a full degree-3 gravity model was used for the global solution. Moreover data from three other flybys were added to better constraint Enceladus' trajectory from 2005 to 2010. These flyby are named E4, E5 and E7 and provided X/X-band data before and after their respective closest approaches with Enceladus.

In this solution, coefficients C_{21}, S_{21} and S_{22} are small compared with J_2 and C_{22} (Table 5.12). This is an indication that tidal and rotational forces dominate and that the adopted rotational model is substantially correct. The estimated value of the J_3 gravity coefficient is compatible at 1-sigma level for both Sol1 and Sol2, a clear indication of the presence of a north-south asymmetry in the gravity field. In both multi arc analyses the post-fit residuals do not show any systematic effect and their rms is compatible with the expected noise level. Figures 5.10 to 5.13 show the post-fit residuals for E9 and E12 for both Sol1 and Sol2.

Gravity from topography

The multi arc analysis has shown that a gravity model made of a full degree-3 field is necessary to fit correctly the data. However, the available data set is not enough to retrieve a reliable estimate of all degree-3 coefficients. They can absorb some dynamical effects leading to a better solution but their value may not be directly related to mass inhomogeneities in the interior of Enceladus. Therefore, in order to reduce the number of estimated parameters and to retrieve a degree-3 gravity related to the physical mass distribution of the satellite a gravity estimate

Figure 5.10: X/Ka Doppler Post-fit Residuals for E9 multi arc solution Sol1
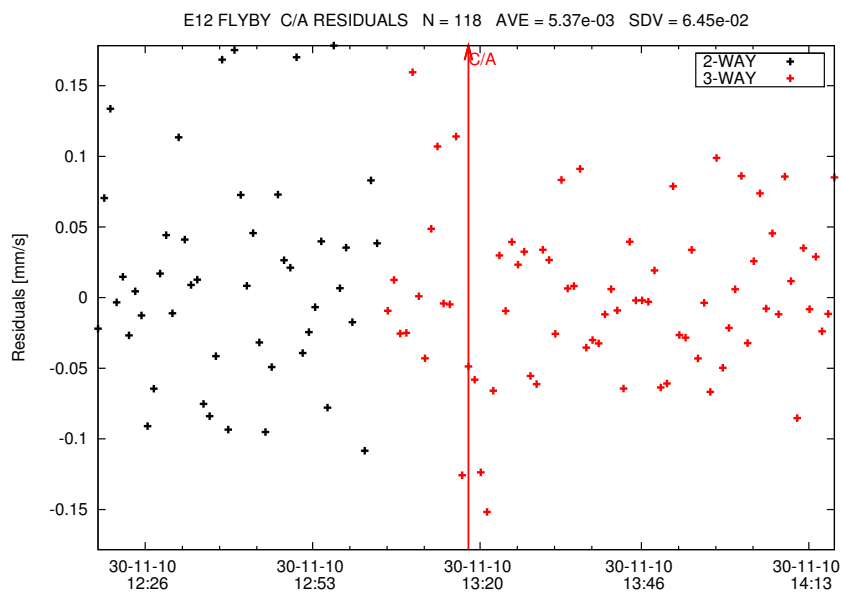
Figure 5.11: X/Ka Doppler Post-fit Residuals for E12 multi arc solution Sol1

Degree	Order	Gravity coefficients	
n	m	$C_{nm}(\times 10^6)$	$S_{nm}(\times 10^6)$
2	0	-4667.3 ± 112.0	
2	1	0.7 ± 7.5	0.4 ± 52.0
2	2	1449.2 ± 221.1	258.6 ± 55.8
3	0	443.7 ± 90.2	
3	1	-115.5 ± 56.0	280.4 ± 35.6
3	2	121.9 ± 81.0	-72.1 ± 37.9
3	3	-6.9 ± 14.8	-14.6 ± 30.0

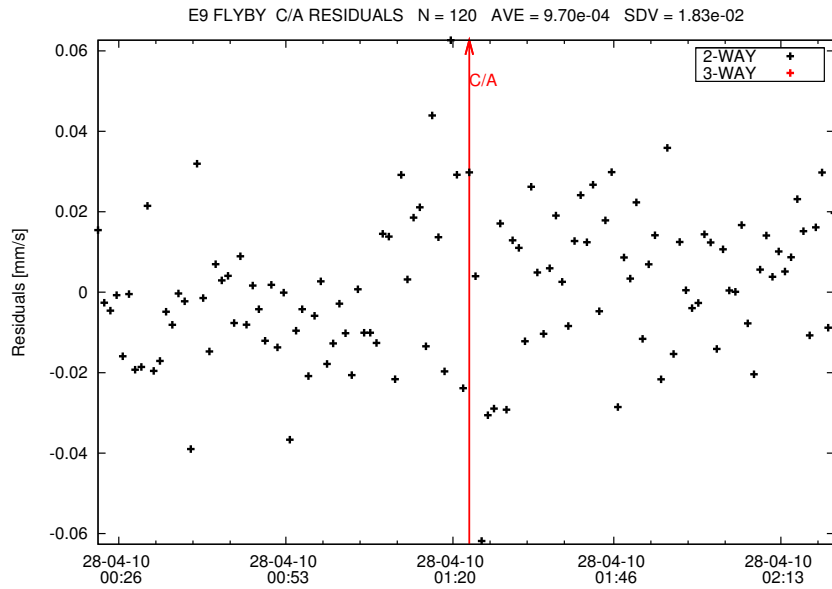**Table 5.12:** Enceladus multi arc gravity solutions based on E0, E4, E5, E7, E9 and E12 data (Sol2)
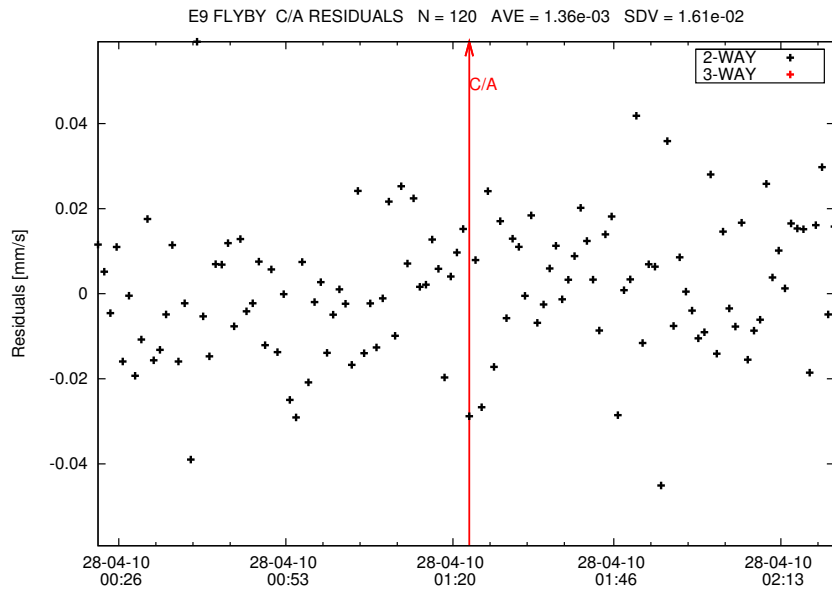
Figure 5.12: X/Ka Doppler Post-fit Residuals for E9 multi arc solution Sol2

Figure 5.13: X/Ka Doppler Post-fit Residuals for E12 multi arc solution Sol2

driven by information about Enceladus topography was carried out. This approach is also useful because topography of degree-3 and higher, if uncompensated and not properly accounted for may bias the estimates of Enceladus quadrupole gravity coefficients (Nimmo et al., 2011). In this way we therefore take into account another possible source of error in our previous solutions.
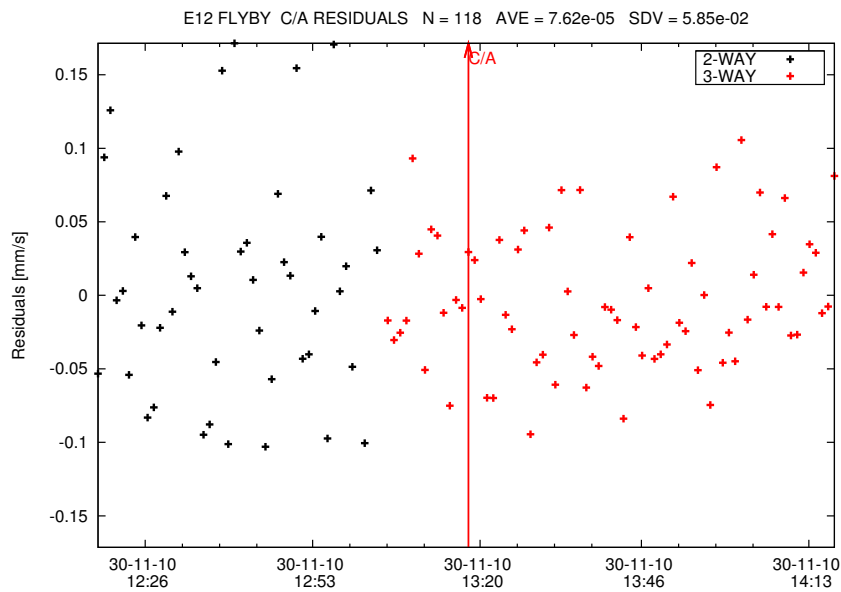
As described in section 2.5 there is an exact relation between gravity and topography. If a low-degree expansion of the topography in spherical harmonics is available it may be used to directly determine the gravity coefficients. The only unknown parameter in the process is the compensation factor C (see eq. 2.26). Following the scheme described in section 4.1.4 a dedicated code was developed to compute the partial derivatives of the observables with respect to the compensation factor. The total number of estimated gravity parameters was then reduced from 12 (5 degree-2 + 7 degree-3 coefficients) to 6 (5 degree-2 coefficients + 1 compensation factor). This approach allows retrieving a more accurate solution since the reduction of the number of the estimated parameters increases the sensitivity. Moreover the degree-3 gravity that is derived from the compensation factor is directly related to the topography of the satellite. The main limit of this method is that a global compensation factor may not be fully adequate to describe a body like Enceladus that has a great geological variability between the north and south hemispheres.

Despite of this it is worth trying this approach in a condition where the available data set is limited.

In our case we applied this technique starting from the degree-3 topography coefficients given in Nimmo et al. (2011). We determined a degree-2 gravity field and a compensation factor for Enceladus which are perfectly compatible with the results obtained by directly estimating the gravity field (see table 5.13).

| Degree	Order	Gravity coefficients	
n	m	$C_{nm}(\times 10^6)$	$S_{nm}(\times 10^6)$
2	0	-4858.5 ± 51.0	
2	1	-133.0 ± 18.5	406.8 ± 30.5
2	2	1421.0 ± 48.0	244.4 ± 10.2
Compensation factor		0.936 ± 0.020	

Table 5.13: Enceladus multi arc gravity solutions starting from topographic data

5.2.3 Interpretation

The estimated gravity field is dominated by large quadrupole terms as expected for a tidally-locked body. The different multi arc solutions are compatible at 2-sigma level between each other. The values of J_2 and C_{22} are fully compatible with those of a relaxed body in hydrostatic equilibrium (see figure 5.14). The small deviations from hydrostaticity are not so large to rule out the applicability of Radau-Darwin equation. Despite of the still rather large uncertainties the values of C/MR^2 derived both from C_{22} and J_2 show that Enceladus is a differentiated body (see table 5.14).

The geoid height determined from the multi arc solutions are shown in figures 5.15 to 5.17. The global features are essentially the same in every figure but there is a variability of the depth and height of depressions and elevations. However it is important to take into account that, given the small amount of data, these geoids are quite uncertain. As an example, figure 5.18 shows the errors associated with the geoid heights for the full degree-3 gravity field case. As expected, the geoid is more accurate in the areas sampled during E9 and E12 flybys where the associated error is between 10 and 20 meters. The uncertainty in the other areas can be up to 60
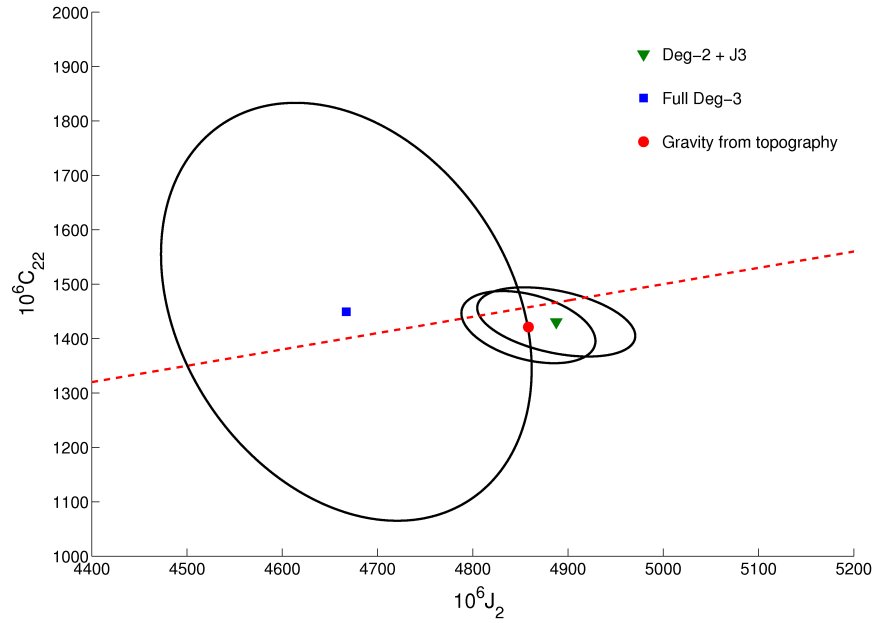
Figure 5.14: Enceladus J2-C22 2-sigma error ellipses for multi arc solutions

Solution	Hydrostatic ratio	C/MR^2 (from C22)	C/MR^2 (from J2)
Deg-2 + J3	3.417 ± 0.127	0.3272 ± 0.0045	0.3305 ± 0.0058
Full Deg-3	3.220 ± 0.497	0.3289 ± 0.0200	0.3245 ± 0.0104
Grav from topo	3.419 ± 0.121	0.3264 ± 0.0044	0.3297 ± 0.0046

Table 5.14: Enceladus' Moments of Inertia computed from multi arc solutions

meters thus making the degree-3 geoid fully compatible with the others. Of course, a more complete coverage would be desirable but the errors in the most interesting areas (i.e. the South Pole) are small enough to get some useful indications also at this stage.
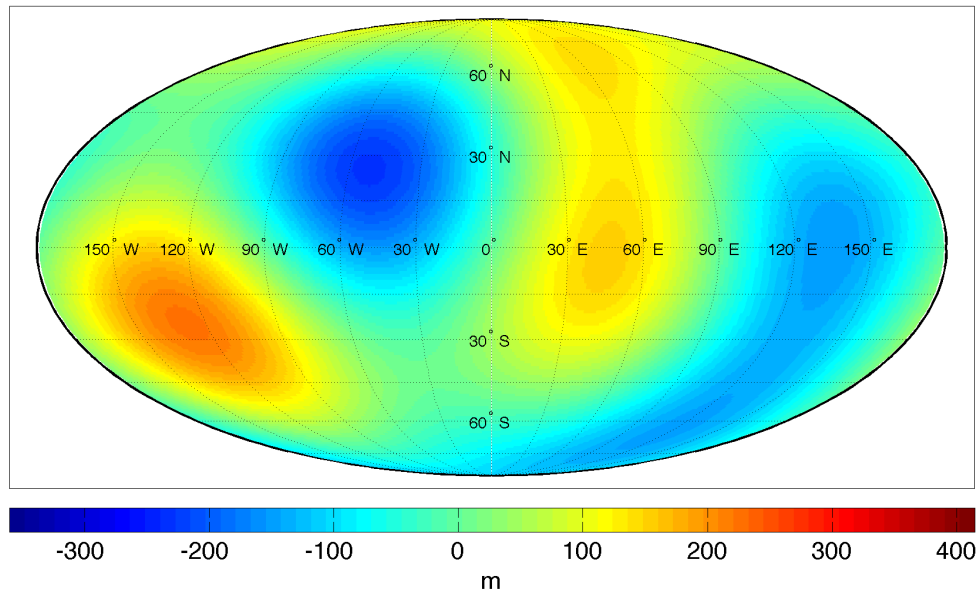
Figure 5.15: Enceladus' geoid heights for multi arc solution deg-2 + J3

The presence of a negative J_3 in all gravity solutions is consistent with a negative mass and gravity anomaly in the south polar region. The geoid heights show in fact the presence of a depression at the South Pole in the range between -50 and -200 meters that points towards the presence of a negative mass anomaly. A mass anomaly at the South Pole should in fact be negative since it necessary contributes to the moments of inertia tensor as well as to J_3. Where it positive it could not be at the South Pole and it would tend to move to the equator. A negative mass anomaly can be physically explained by the presence of a subsurface concentration of liquid water not isostatically compensated. This means that the mass increase in the south polar region due to the presence of liquid water (whose density is greater than the ice in the crust) is compensated by a surface depression in the same area in such a way that the overall effect is a negative mass anomaly. The gravity field estimate carried out using topographic data as starting point can help in confirming this hypothesis. The estimated compensation factor is in fact around one. This means that the topography is essentially uncompensated and that the estimated negative
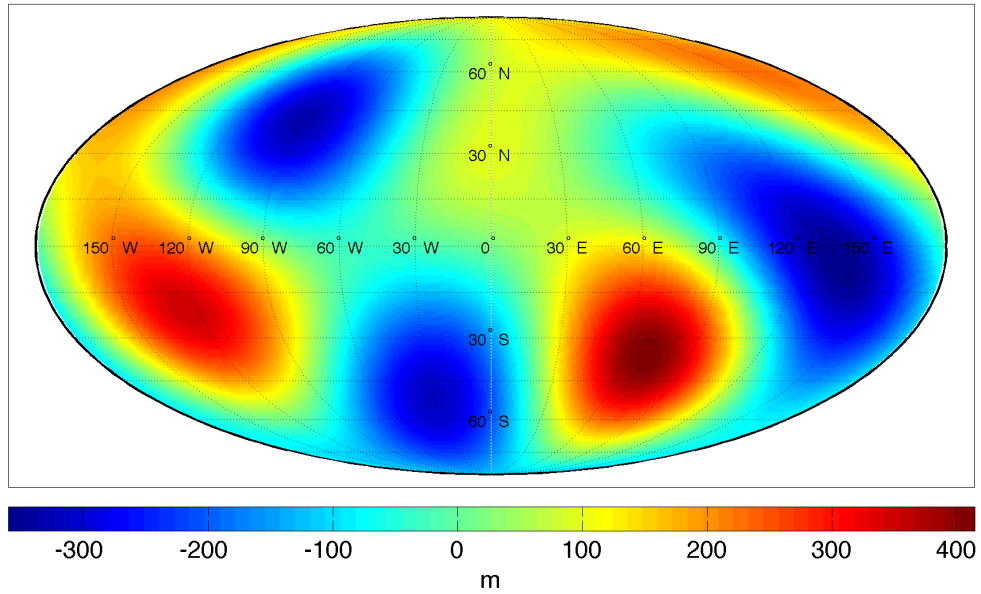
Figure 5.16: Enceladus' geoid heights for multi arc solution full deg-3
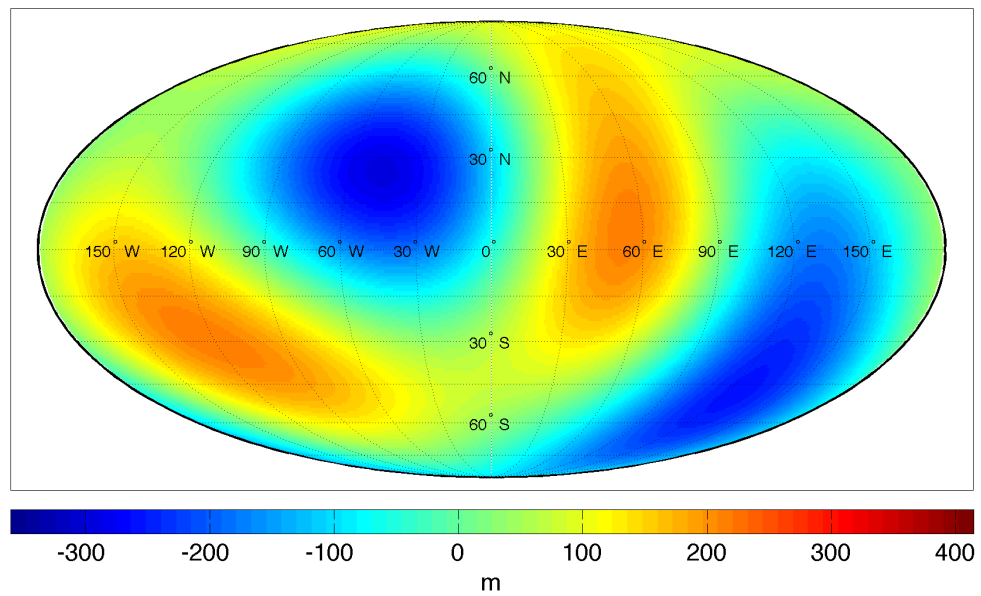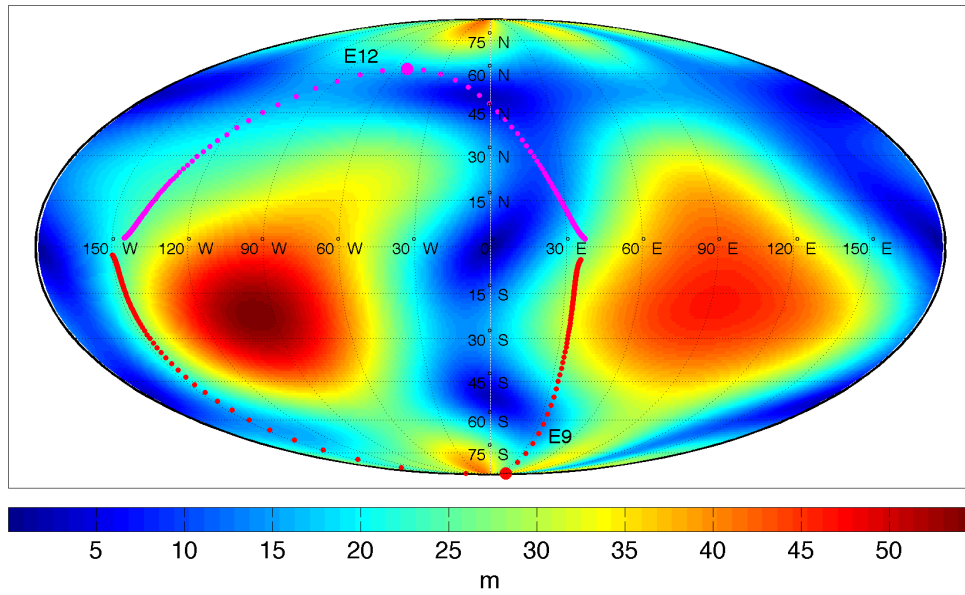

Figure 5.17: Enceladus' geoid heights for multi arc solution gravity from topography

Figure 5.18: Enceladus' geoid heights errors for multi arc solution full deg-3

J_3 can confirm the presence of a subsurface concentration of liquid water at the South Pole as the origin of the observed plumes.

5.3 Dione

The determination of Dione's gravity field was carried out using data from three Cassini flybys (see table 5.15). However, during only one of them, namely D3, Cassini was tracked throughout its closest approach to the satellite allowing the determination of the quadrupole gravity field. D1 flyby was performed in the early phases of the mission to determine the GM of Dione (Jacobson et al., 2006) in order to better characterize the dynamics of the Saturn system and its ephemerides for the definition of the tour trajectory. Range and Doppler measurements in X-band were acquired only before and after closest approach thus preventing the possibility of a first estimation of Dione's quadrupole gravity field. The December 2011 flyby provided instead the first opportunity to detect the signal of gravity field higher harmonics. With a closest approach altitude of about 100 km, D3 data allowed the first estimation of Dione's J_2 and C_{22}. This arc spanned roughly $\pm 24h$ from C/A during which the spacecraft was tracked in X- and Ka-band from Goldstone, Madrid and Canberra DSN stations. C/A occurred during tracking from Madrid at a sun elongation angle (SEP) of about $53°$. This condition is not particularly favorable because data are marred significantly by plasma noise. Nonetheless by using data from D3 only, or by combining them with the other flybys, we were able to obtain the first estimate of Dione's quadrupole gravity field.

5.3.1 Model of Dione gravity field

Before the arriving of Cassini at Saturn, the knowledge of Dione's gravity was limited to its mass whose most recent value had been determined by Jacobson (2004). In his work the estimation of the mass of the Saturn system bodies was carried out using a combination of data from the Voyager missions and data from Earth-based astrometric observations. After the first Dione's flyby an improved estimate of its mass was provided by Jacobson et al. (2006). However, no information on the quadrupole gravity field based on real data was available before the D3 flyby. The model of Dione gravity used for the analysis is then based on geophysical assumptions that come from reasonable hypothesis on its internal structure and composition. A useful reference for the gravity model definition can be found in Zharkov et al. (1985). Dione, which is synchronously rotating around Saturn, is supposed to be in hydrostatic equilibrium and two different interior models are proposed. Table 5.16 reports the proposed models whose only difference is the density of the ice-layer overlaying the hydrous silicate core (of radius R_c). The a priori

	D1	**D3**
Date	11-OCT-2005 17:53:04 ET	12-DEC-2011 09:40:29 ET
SEP	68.8°	53.2°
Altitude (km)	498	100
Latitude	-60.4°	4.8°
Longitude	91.9°	267.9°
Inclination	119.6°	175.2°
N. of points	373	1253
Noise (mm/s)	0.045	0.054

Table 5.15: Geometric and orbital parameters of the two flybys used for Dione gravity determination

gravity model used in our analysis is then set according to the "Dione B" two-layer model. Higher degree harmonics are not considered in the analysis because they would not be detectable using the available data set.

Model	**R (km)**	R_c/R	**Core density**	**Ice-layer desnsity**	J_2	C_{22}
Dione A	560	0.597	3.0 g/cm^3	1.0 g/cm^3	1.32	0.396
Dione B	560	0.597	3.0 g/cm^3	0.9 g/cm^3	1.20	0.361

Table 5.16: Dione interior structure and gravity model from Zharkov et al. (1985)

The rotational state of Dione comes from the IAU reference frame definition. The spin axis is perpendicular to the orbital plane and the prime meridian is aligned with the direction of Saturn at pericenter. Right ascension and declination of the pole and longitude of the prime meridian are defined in table 5.17. In this condition, given also the hypothesis of hydrostatic equilibrium, the gravity coefficients C_{21}, S_{21} are considered always zero and never estimated. Their estimation would be

α	$40.°660 - 0.°0360T$
δ	$83.°520 - 0.°0040T$
W	$357.°600 + 131.°3493160d$

Table 5.17: Dione rotational model adopted for the gravity solutions. T is given in Julian centuries (of 36525 days) past J2000 and d are days past J2000.

anyway very difficult given the limited amount of data available and the scarce sensitivity.

A priori uncertainties on the estimated parameters were set in order to avoid any constraint on the final solution (see table 5.18) that we wanted to be driven only by the data information content.

Parameter	Value ($\times 10^3$)	Uncertainty ($\times 10^3$)
J_2	1.20	1.00
C_{22}	0.361	1.00
S_{22}	0.0	0.10
C_{21}	0.0	-
S_{21}	0.0	-

Table 5.18: A priori values and uncertainties for Dione gravity model

5.3.2 Analysis methods

Data analysis was carried out using the approach described in section 4. For Dione the estimated parameters included the quadrupole gravity field harmonics and Cassini state vector and Dione's GM and state vector. A different state vector was estimated for Cassini in each arc while Dione state vector was estimated only once at a given reference epoch (21-SEP-2005 00:00:00 UTC) to grant the coherence of its trajectory during the different flybys. Saturn system ephemerides were then updated to take into account the new Dione's trajectory. Data were weighted ac-

cording to the scheme presented in section 4.4.3. AMC calibrations were available only for D3, while for the other flybys TSAC were applied.

Data count time was selected as a trade off between the need of sensitivity and the need to avoid numerical noise. To satisfy the sensitivity requirement a count time of 10 s or even lower would be desirable. In fact, during the D3 encounter, for example, the interaction time was about 130 s given a relative velocity of 8.7 km/s ($t \sim 2R_D/V_{rel}$). However, as described in section 3.2.3, numerical noise is higher at lower count times. For this reason a count time of 60 s was selected. Using a lower count time would in fact prevent the possibility of seeing remaining signatures in the fit bringing to the wrong conclusion that a reliable solution has been achieved.

A single flyby with tracking at C/A may not bear enough information to determine independently J_2 and C_{22} especially if the flyby is equatorial (higher sensitivity to C_{22}) or polar (higher sensitivity to J_2). Although an approach based exclusively on the data would be desirable as pointed out for Rhea (Mackenzie et al., 2008), the imposition of some constraint may be an alternative approach (Anderson and Schubert, 2007). In the case of Dione we produced two different solutions using both the possible approaches. In the first one we forced J_2 and C_{22} to satisfy the hydrostatic equilibrium ($J_2 = 10/3C_{22}$, see section 2.2), while in the second one we produced an unconstrained solution.

A first solution was produced using data from only D3. The inclusion of data from the other arcs, in fact, bears almost no information on the quadrupole gravity field while it can be useful to improve the estimation of Dione state vector thus constraining better its trajectory. As a consequence a general improvement in the solution (both central values and estimated uncertainties) may be expected but a single arc analysis is a better starting point to obtain a first reliable solution for the quadrupole gravity coefficients. Moreover D1 flyby was not designed for gravity observations and can have some criticalities to take into account such as maneuvers during the tracking passes. The following cases were analyzed and are presented here:

1. Single arc solution with data from D3 only. Hydrostatic equilibrium constraint applied.

2. Single arc solution with data from D3 only. No hydrostatic equilibrium constraint applied.

3. Multiarc solution with data from D1 and D3. No hydrostatic equilibrium constraint applied.

5.3.3 Results

The orbit determination process converged in all cases after four iterations. The post-fit Doppler residuals do not show any systematic effect and the overall rms is compatible with the expected noise level given the SEP angle of each flyby. Figures 5.19 to 5.21 report the post-fit residuals at $\pm$ 2h from C/A of the D3 flyby which should present signatures if the estimated gravity field was unreliable. The rms of the C/A pass is however almost constant in the cases analyzed suggesting that no solution can be preferred over the others in this phase.

As expected for an almost equatorial flyby, C_{22} is determined with much better accuracy than J_2. The good determination of C_{22} results from a combination of the D3 flyby favorable geometry and low Doppler noise (thanks to the Ka-band radio link and the high signal-to-noise ratio).

The addition of more data (Case 3) do not improve the estimated uncertainty of C_{22} which is fully determined by the most sensitive D3 data. However the addition of D1 data helps in constraining Dione's ephemerides leading to a more coherent solution.

Solution	$J_2(\times 10^6)$	$C_{22}(\times 10^6)$	$S_{22}(\times 10^6)$	J_2/C_{22}	Correlation J_2/C_{22}
Case 1	1269.8 ± 7.0	380.5 ± 2.1	-23.7 ± 3.0	3.337 ± 0.026	1.00
Case 2	1443.3 ± 17.3	361.0 ± 2.6	-24.2 ± 3.0	4.001 ± 0.056	-0.23
Case 3	1433.6 ± 9.5	364.9 ± 2.6	-23.5 ± 3.0	3.929 ± 0.038	-0.40

Table 5.19: Dione gravity solutions

5.3.4 Interpretation

Figure 5.22 shows the different solutions plotted in the plane J_2-C_{22} with their 1-sigma error ellipses. Solutions that are on the red dashed line or cross it are compatible with the hydrostatic equilibrium. For Case 1 the error ellipse is reduced to a line that lies on the hydrostatic line since this solution was strongly constrained to the hydrostatic equilibrium. Cases 2 and 3 are instead more than 3-sigma apart from the hydrostatic line suggesting that a significant departure from hydrostaticity cannot be excluded on the basis of the available data set.
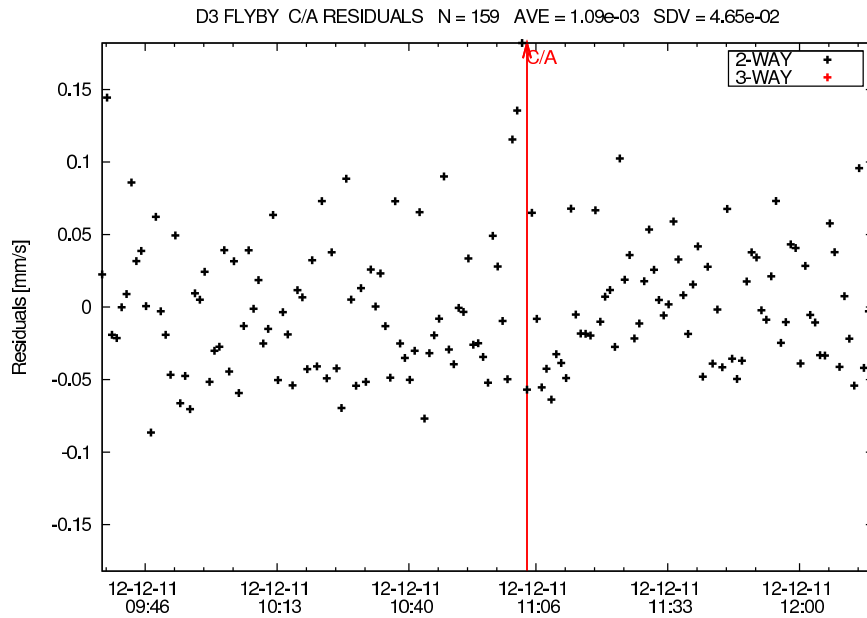
Figure 5.19: X/Ka Doppler Post-fit Residuals for Case 1 solution
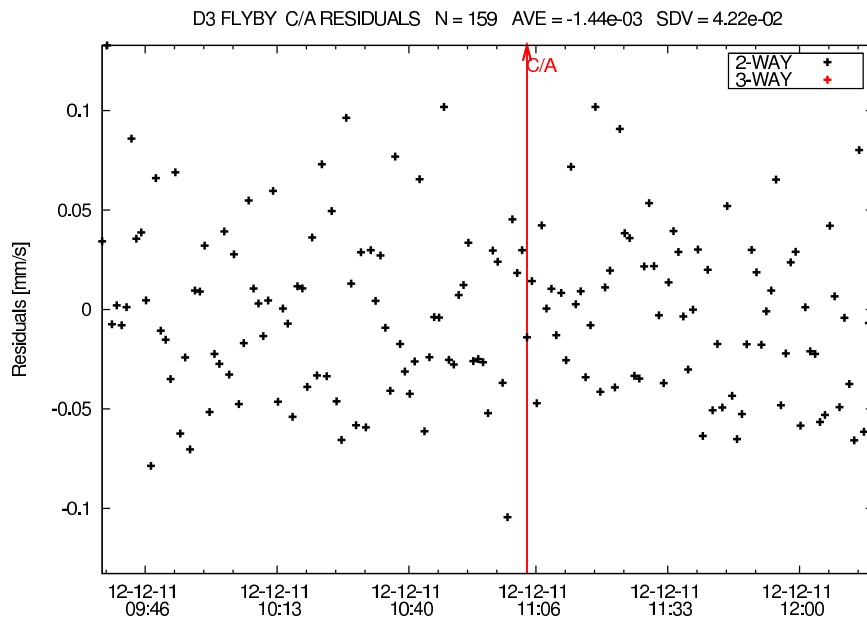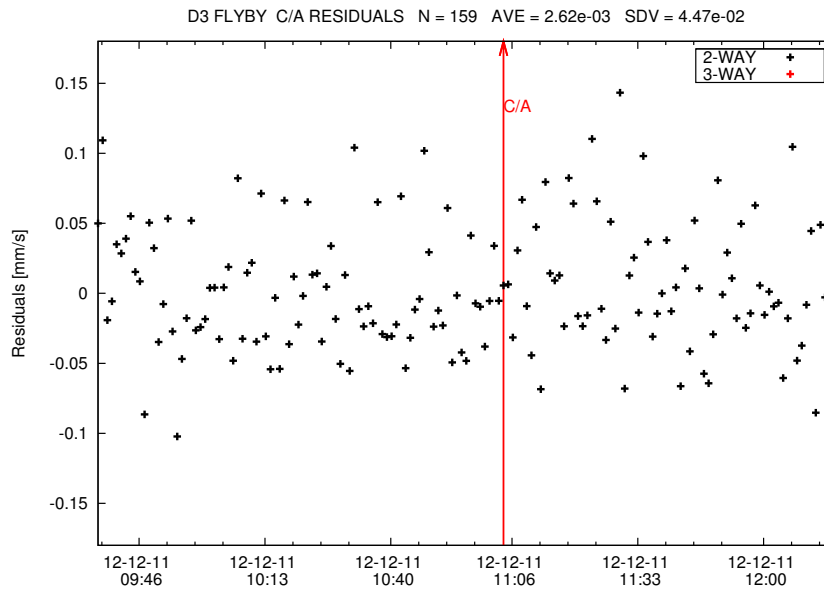

Figure 5.20: X/Ka Doppler Post-fit Residuals for Case 2 solution

Figure 5.21: X/Ka Doppler Post-fit Residuals for Case 3 solution

For the hydrostatic solutions the Radau-Darwin equation may be used to determine the moment of inertia factor C/MR^2. The same equation can be applied also to the non-hydrostatic solutions but in this case, since the 10/3 ratio between J_2 and C_{22} is not satisfied, one of the two coefficients has to be selected as starting point to compute the fluid Love number k_f and then the Moment of Inertia Factor (MoIF). C_{22} is the best choice because its determination is more accurate than J_2 given the flyby geometry. Recall, however, that the use of Radau-Darwin equation may led to significant errors in the determination of the MoIF if the body is not in hydrostatic equilibrium (Gao and Stevenson, 2012). Table 5.20 reports the MoIF computed for the different solutions.

Solution	C/MR^2
Case 1	0.3245 ± 0.0007
Case 2 (from C_{22})	0.3177 ± 0.0009
Case 3 (from C_{22})	0.3191 ± 0.0009

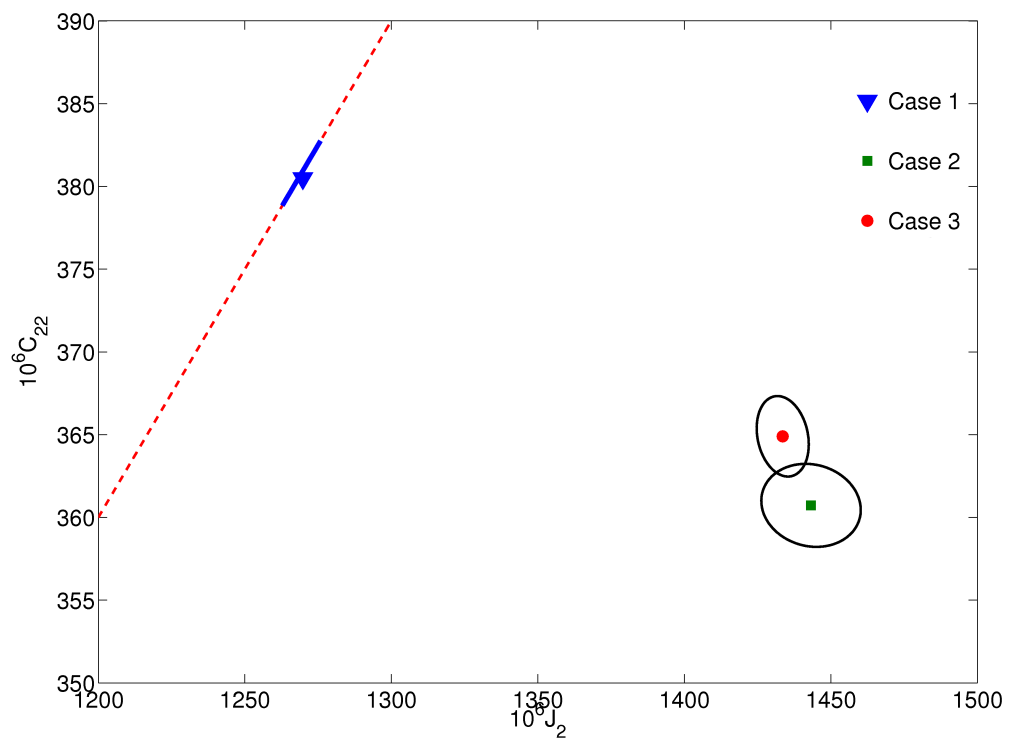**Table 5.20:** Dione's MOIF computed for the different solutions

Figure 5.22: J2-C22 1-sigma error ellipses

Given the current uncertainties and the fact that the hypothesis of hydrostatic equilibrium may be not fully consistent it is not possible to assess the degree of differentiation that is determining radius and density of the different layers. However, even though the value of the Moment of Inertia Factor (MoIF) can vary up to 20% if the hydrostatic hypothesis is not satisfied (Gao and Stevenson, 2012), the estimated value of ~ 0.32 indicates that Dione's internal structure is significantly differentiated. Variations of this value can bring to different conclusions about the degree of differentiation but it is already possible to exclude that Dione is homogeneous (MoIF = 0.4). This is an important point because it can give useful indications on the formation and accretion processes of Dione. As a useful example we suppose that the MoIF is 0.32 and compute the radii of the layers for a simple two-layers model. We consider an interior with density $3.0 g/cm^3$ composed of hydrated silicates and a mantle made of ice with two different levels of impurity. The results are reported in table 5.21

Model	$R_1(km)$	$R_2(km)$	$\rho_1(g/cm^3)$	$\rho_2(g/cm^3)$
Ice I	222	339	3.0	0.9
Ice II	232	329	3.0	1.0

Table 5.21: Two-layer Dione internal structure

The depth of the different layers varies of about 10 km depending on the density of the ice. A large core made of hydrous rocks is probably present on Dione given the estimated MoIF.

Although some conclusions can be drawn, there remain some open questions regarding Dione's gravity field. First of all the hypothesis of hydrostatic equilibrium has to be confirmed or disproved to guarantee that the inferred MoIF is correct. This will need an independent estimation of the quadrupole gravity field and in particular of J_2. Data from the next Dione flyby, scheduled for August 2015, will help to solve this issue and improve the current results.

Chapter 6

Conclusions and perspectives

The geodesy of the Saturnian satellites Titan, Enceladus and Dione has been inferred from the analysis of Cassini tracking data acquired during a series of fly-bys performed from 2004 to 2011. Thanks to the radio science instrumentation on board Cassini, very accurate range and range-rate data were available and used to estimate the gravity fields of the satellites under investigation. The definition of a dynamical model, that takes into account a variety of forces acting on the spacecraft, has been the fundamental premise for the solution of the orbit determination problem at hand. Every dynamical effect has been modeled deterministically according to the available models of the dynamics of the Saturn system and of the selected satellites. The analysis process involved also the determination and update of the ephemerides of the investigated satellites to produce a better characterization of the Saturn sistem dynamics. Range and Doppler data available were calibrated for the delays introduced by the transmission media (Earth's troposphere and ionosphere and interplanetary plasma) and weighted on a pass-by-pass basis to account for their intrinsic quality. From a data analysis point of view, all the solutions presented can be considered reliable. In fact, the orbit determination process always converges and, in every case analyzed, the post-fit residuals are always compatible with the expected noise level. However, from a geophysical point of view, the reliability of the various solutions needs to be analyzed in more detail for every satellite of Saturn to confirm their compatibility with the available models of their chemical composition and evolution processes.

On Titan, precise measurements of the acceleration of the Cassini spacecraft during six close flybys have revealed that the satellite responds to the variable tidal field exerted by Saturn with periodic changes of its quadrupole gravity field, at about 3-

4% of the static value. We have estimated the real part of the tidal Love number k_2 (Iess et al., 2012) which indicates how Titan is deformed due to the tidal stresses. The large estimated value (~ 0.6) is consistent with the presence of a subsurface ocean under the ice shell. However, to reconcile the estimated value with a reliable geophysical model a low viscosity interior has to be invoked. The estimation of the imaginary part of k_2, which measures the internal dissipation due to the tidal potential, can help in improving the interior model. However the limited amount of data prevented us to obtain a reliable estimate of the imaginary part whose uncertainty is still too high to draw any significative conclusion. The updated gravity field of Titan retrieved from the analysis of the six gravity flybys completed so far is compatible with the previous determinations (Iess et al., 2010). Apart from the standard degree-3 gravity solution we also produced a degree-4 field to assess the sensitivity to higher degree harmonics and to verify the Love number solution stability. The estimated Moment Of Inertia Factor of 0.3431±0.0004 confirms the previous estimates and the differentiated internal structure. However, the chemical and thermal properties of the different layers postulated in the geophysical models published so far, may have to be revised to take into account the implications of the estimated value of the Love number. The next three gravity flybys of Titan scheduled respectively in 2013, 2014 and 2016 will help in confirming the current result and estimate higher harmonics of the gravity field. Comparisons of gravity with topography to assess the degree of compensation will in fact require the degree-4 gravity which is not enough accurately estimated with the current data set. Moreover, these data will be valuable to improve the estimate of the imaginary part of k_2 to better understand the origin of the observed eccentricity in Titan's orbit.

The combined analysis of three Enceladus flybys has revealed a complex gravity field. In fact we detected the presence of degree-3 gravity anomalies that prevented us to obtain a reliable fit using a gravity model made up of a pure quadrupole. We determined that Enceladus' quadrupole gravity field is close to the hydrostatic equilibrium and its Moment of Inertia Factor derived from the Radau-Darwin equation suggests that its interior is differentiated. The presence of a hydrous rocky core overlaid bean ice layer was in fact expected given the endogenic active processes that take place on Enceladus. Moreover, the estimate of a negative J_3 suggests the presence of a mass anomaly at the south pole. This asymmetry in the gravity field is compatible with the presence of a subsurface concentration of liquid water which can be interpreted as the origin of the observed geysers in the south polar region. A gravity field estimation driven by topographic data has revealed that there is al-

most no isostatic compensation in that region. The geoid depression at the south pole (about 100 meters) is comparable with the topography depression in the same area. This is an important confirmation that the gravity anomaly we detected is due to a water deposit under the surface. Our results cannot rule out, however, the possibility that there is a global ocean under the surface and not only a concentration of water in the south polar region. Cassini performed the last Enceladus' flyby dedicated to gravity measurements on May 2, 2012. Data from this flyby are currently under analysis and will help in confirming the previous solutions and lower the current estimation uncertainties. No other gravity flybys of Enceladus are scheduled up to the end of the mission in 2017 but data retrieved so far have already given us important indications about Enceladus' internal structure and composition.

The determination of the quadrupole gravity field of Dione has given the first indications on its internal structure. Data from the only available flyby with tracking at closest approach are not sufficient to fully disentangle the estimates of the gravity coefficients J_2 and C_{22}. We therefore produced a first estimate by constraining J_2 and C_{22} to the hydrostatic equilibrium ($J_2 = 10/3C_{22}$) and a second one in which we left them independent. From a data analysis point of view the two solutions are equally reliable given that the post-fit residuals do not show systematic effects in both cases. However, the unconstrained solution shows a significant deviation from the hydrostatic equilibrium (more than 3-sigma). In this case the use of the Radau-Darwin equation to derive the Moment of Inertia Factor can lead to a wrong value if applied to the unconstrained solution. Nonetheless, even by accounting for this possible error, the Moment of Inertia Factor is in the range 0.316-0.325 indicating that Dione is significantly differentiated. We also derived a possible interior model made up of a hydrous silicate core of about 220 km radius surrounded by an ice layer. Next Dione's flyby dedicated to gravity measurements in 2015 will be crucial to confirm or disprove the hydrostatic equilibrium hypothesis. The more inclined flight path should allow a better estimation of J_2 with a significant improvement on the overall gravity field estimation.

In conclusion, the analysis carried out in this thesis has provided fundamental constraints about the geodesy of the main Saturnian satellites. The high quality Cassini data allowed for the first time the estimation of the tidal Love number k_2 for a major planetary satellite. The presence of a subsurface ocean on Titan, foreseen by many geophysical models, is now supported by experimental data. Similarly, the analysis of Enceladus gravity confirms the hypothesized presence of a water deposit under the south pole that supplies the ejecting geysers. Finally, the

inferred constraints on Dione's internal structure demonstrate that the major Saturnian satellites are all differentiated thus giving fundamental indications about the formation and accretion processes in the Saturn system. Data that will be collected up to the end of Cassini mission in 2017 will help in confirming the results derived here and in decreasing the uncertainties but we do not expect significant variations of the conclusions presented in this work.

Bibliography

Anderson, J. D., Schubert, G., 2007. Saturn's satellite Rhea is a homogeneous mix of rock and ice. Geophys. Res. Lett. 34 (L02202).

Arfken, G., 1985. The Addition Theorem for Spherical Harmonics. Vol. Mathematical Methods for Physicists. Academic Press, Orlando, FL.

Bar-Sever, Y. E., Jacobs, C. S., Keihm, S., Lanyi, G. E., Naudet, C. J., Rosenberger, H. W., Runge, T. F., Tanner, A. B., Vigue-Rodi, Y., 2007. Atmospheric Media Calibration for the Deep Space Network. In: Proceedings of the IEEE. No. 11. pp. 2180–2192.

Barnes, J. A., Chi, A. R., Cutler, L. S., Healey, D. J., Leeson, D. B., McGunigal, T. E., Mullen, J. A., Smith, W. L., Sydnor, R. L., Vessot, R. F. C., , Winkler, G. M. R., 1971. Characterization of Frequency Stability. In: IEEE Transaction on Instrumentation and Measurement. No. 2. pp. 105–120.

Baum, W., Kreidl, T., Westphal, J., Danielson, G., Seidelmann, P., Pascu, D., Currie, D., 1981. Saturn's E ring. Icarus 47, 84–96.

Bertotti, B., Comoretto, G., Iess, L., 1993. Doppler Tracking of Spacecraft with Multifrequency Links. Astronomy and Astrophysics 269 (1-2), 608–616.

Bertotti, B., Farinella, P., Vokrouhlicky, D., 2003. Physics of the solar system. Kluwer Academic Publishers.

Bills, B., Nimmo, F., 2008. Forced obliquity and moments of inertia of Titan. Icarus 196, 293–297.

Campbell, J. K., Anderson, J. D., 1989. Gravity field of the saturnian system from Pioneer and Voyager tracking data. Astron. J. 97, 1485–1495.

Castillo-Rogez, J. C., Lunine, J. I., 2010. Evolution of Titan's rocky core constrained by Cassini observations. Geophysical Research Letters 37 (L20205).

Clairaut, A. C., 1743. Théorie de la Figure de la Terre, Tireé des Principes de l'Hydrostatique. Durand, Paris.

Clark, S. C., 2008. Solar Absorptance of Cassini HGA Paint. Tech. rep., JPL.

Darwin, G. H., 1899. The theory of the figure of the Earth carried to the second order in small quantities. Mon. Not. R. Astron. Soc. 60, 82–124.

Ekelund, J. E., Esposito, P. B., Benson, R., 1996. DPTRAJ-DP User's Reference Manual. Jet Propulsion Laboratory Navigation Software Group, Tech. Rep. Vol. 1 Edition.

Elgered, G., 1992. Tropospheric Radio Path Delay From Ground-Based Microwave Radiometry. Atmospheric Remote Sensing by Microwave Radiometry, New York.

Fortes, A. D., 2011. Titan's internal structure and the evolutionary consequences. Planetary and Space Science 60 (1), 10–17.

Gao, P., Stevenson, D. J., 2012. How does nonhydrostaticity affect the determination of icy satellites' moment of inertia? Abstract 1701 - 43rd LPSC.

Grasset, O., Sotin, C., Deschamps, F., 2000. On the internal structure and dynamics of Titan. Planetary and Space Science 48, 617–636.

Hansen, C. J., L., E., Stewart, A., Colwell, J., Hendrix, A., Pryor, W., Shemansky, D., R., W., 2006. Enceladus' water vapor plume. Science 311, 1422–1425.

Henry, C. A., 2002. An introduction to the design of the Cassini spacecraft. Space Science Reviews (104), 129–153.

Iess, L., Jacobson, R. A., Ducci, M., Stevenson, D. J., Lunine, J. I., Armstrong, J. W., Asmar, S. W., Racioppa, P., Rappaport, N. J., Tortora, P., 2012. The Tides of Titan. Science.

Iess, L., Rappaport, N. J., Jacobson, R. A., Racioppa, P., Stevenson, D. J., Tortora, P., Armstrong, J. W., Asmar, S. W., 2010. Gravity Field, Shape, and Moment of Inertia of Titan. Science 327, 1367.

Jacobson, R., Antreasian, P., Bordi, J., Criddle, K., Ionasescu, R., Jones, J., MacKenzie, R., Meek, M., et al., December 2006. The Gravity Field of the Saturnian System from Satellite Observations and Spacecraft Tracking Data. The Astronomical Journal 132 (6), 2520–2526.

Jacobson, R. A., 2003. Satellite Software Users Guides. Tech. rep., JPL.

Jacobson, R. A., 2004. The Orbits of the major Saturnian Satellites and the gravity field of Saturn from spacecraft and Earth-based observations. The Astronomical Journal 128, 492–501.

Jeffreys, H., 1962. The Earth. Cambridge University Press, London.

Kalman, R. E., 1960. A New Approach to Linear Filtering and Prediction Theory. J. Basic Eng. 82 (1), 35–45.

Kaula, W. M., 1966. Theory of Satellite Geodesy. Blaisdell, Waltham, MA.

Kliore, A. J., Anderson, J. D., Armstrong, J. W., Asmar, S. W., Hamilton, C. L., Rappaport, N. J., Wahlquist, H. D., Ambrosini, R., Flasar, F. M., French, R. G., Iess, L., Marouf, E. A., Nagy, A. F., 2004. Cassini Radio Science. Space Science Reviews 115, 1–70.

Kuiper, G., 1944. Titan: a satellite with an atmosphere. Astrophys J 100, 378–383.

Langhans, M., Jaumann, R., Stephan, K., Brown, R., Buratti, B., Clark, R., Baines, K., Nicholson, P., Lorenz, R., Soderblom, L., Soderblom, J., Sotin, C., Barnes, J., Nelson, R., 2012. Titan's fluvial valleys: Morphology, distribution, and spectral properties. Planetary and Space Science 60 (1), 34–51.

Lawson, C. L., Hanson, L. J., 1974. Solving Least Squares Problems. Prentice-Hall.

Lorenz, R. D., Witasse, O., Lebreton, J.-P., Blancquaert, T., De Pater, I., Mazoue, F., Roe, H., Lemmon, M. T., Burratti, B. J., Holmes, S., Noll, K., 2006. Huygens entry emission: Observation campaign, results, and lessons learned. J Geophys Res 111.

Love, A. E. H., 1906. A Treatise on the Mathematical Theory of Elasticity. Cambridge Univ. Press, Cambridge, UK.

Mackenzie, R. A., Iess, L., Tortora, P., Rappaport, N. J., 2008. A non-hydrostatic Rhea. Geophys. Res. Lett. 35 (L05204).

Matson, D. L., Spilker, L. J., Lebreton, J., 2002. The Cassini/Huygens mission to the Saturnian System. Space Science Reviews 104, 1–58.

Milani, A., Gronchi, G., 2010. Theory of orbit determination. Cambridge University Press.

Moyer, T. D., May 15 1971. Mathematical Formulation of the Double-Precision Orbit Determination Program (DPODP). Tech. rep., JPL.

Moyer, T. D., 2000. Formulation for Observed and Computed Values of Deep Space Network Data Types for Navigation. Deep-Space Communications and Navigation Series 2. JPL, Pasadena, CA.

Nimmo, F., Bills, B., Thomas, P. C., 2011. Geophysical implications of the long-wavelength topography of the Saturnian satellites. Journal of Geophysical Research 116.

Nimmo, F., Spencer, J., Pappalardo, R., Mullen, M., 2007. Shear heating as the origin of the plumes and heat flux on Enceladus. Nature 447, 289–291.

Persi del Marmo, P., Iess, L., Picardi, G., Seu, R., Bertotti, B., 2007. The determination of Titan's rotational state from Cassini SAR images. In: AGU (Ed.), EOS Trans. Vol. 88(52).

Peters, C. F., December 1981. Numerical integration of the satellites of the outer planets. Astronomy and Astrophysics 104 (1), 37–41.

Porco, C. C., Helfenstein, P., Thomas, P. C., Ingersoll, A. P., Wisdom, J., West, R., Neukum, G., Denk, T., Wagner, R., Roatsch, T., Kieffer, S., Turtle, E., McEwen, A., Johnson, T. V., Rathbun, J., Veverka, J., Wilson, D., Perry, J., Spitale, J., Brahic, A., Burns, J. A., DelGenio, A. D., Dones, L., Murray, C. D., Squyres, S., 2006. Cassini Observes the Active South Pole of Enceladus. Science 311, 1393.

Postberg, F., Kempf, S., Schmidt, J., Brillantov, N., Beinsen, A., Abel, B., Buck, U., Srama, R., 2009. Sodium salts in E Ring ice grains from an ocean below Enceladus' surface. Nature 459, 1098–1101.

Racioppa, P., 2012. ORACLE Documentation. Html, DIMA - Università "La Sapienza".

Radau, R., 1885. Sur la loi des densités à l'intérieur de la Terre. C.R. Acad. Sci. Paris 100, 972–974.

Rappaport, N. J., Bertotti, B., Giampieri, G., Anderson, J. D., 1997. Doppler Measurements of the Quadrupole Moments of Titan. Icarus 126, 313–323.

Rappaport, N. J., Iess, L., Tortora, P., Anabtawi, A., Asmar, S. W., Somenzi, L., Zingoni, F., 2007. Mass and interior of Enceladus from Cassini data analysis. Icarus 190 (1), 175–178.

Rappaport, N. J., Iess, L., Wahr, J., Lunine, J. I., Armstrong, J. W., Asmar, S. W., Tortora, P., Benedetto, M. D., Racioppa, P., 2008. Can Cassini detect a subsurface ocean in Titan from gravity measurements? Icarus 194, 711–720.

Resch, G. M. e. a., 2002. The Media Calibration System for Cassini Radio Science: Part III. IPN Progress Report, 42-148, 1–12.

Schmidt, J., Brilliantov, N., Spahn, F., Kempf, S., 2008. Slow dust in Enceladus' plume from condensation and wall collisions in tiger stripe fractures. Nature 451, 685–688.

Smith, B. e. a., 1982. A new look at the Saturn system: The Voyager 2 images. Science 215, 504–537.

Solá, J. C., 1908. Observationes des Satellites Principaux de Jupiter et de Titan. Astron Nachr 179, 289–290.

Somenzi, L., 2006. Multi arc analysis and least-square fit. Tech. rep., DIMA - Università "La Sapienza".

Spencer, J., Pearl, J., Segura, M., Flasar, F., Mamoutkine, A., Romani, P., Buratti, B., Hendrix, A., Spilker, L., Lopes, R., 2006. Cassini Encounters Enceladus: Background and the discovery of a south polar hot spot. Science 311, 1401–1405.

Spencer, J. R., Barr, A. C., Esposito, L. W., Helfenstein, P., Ingersoll, A. P., Jaumann, R., McKay, C. P., Nimmo, F., Waite, J. H., 2009. Enceladus: An Active Cryovolcanic Satellite. Springer-Science, Ch. 21.

Stiles, B., Kirk, R., Lorenz, R., Hensley, S., Lee, E., Ostro, S., Allison, M., Callahan, P., Gim, Y., Iess, L., del Marmo, P. P., Hamilton, G., Johnson, W., West, R., Team, C. R., 2008. Determining Titan's spin state from Cassini RADAR images. Astron. J. 135, 1669–1680.

Tapley, B., Schutz, B. E., Born, G. H., 2004. Statistical Orbit Determination. Elsevier, Burlington, MA.

Thomas, P., Burns, J., Helfenstein, P., Squyres, S., 2007. Shapes of the saturnian icy satellites and their significance. Icarus 190, 573–584.

Thornton, C. L., Border, J. S., October 2000. Radiometric Tracking Techniques for Deep-Space Navigation. Deep-Space Communications and Navigation Series Monograph 1. JPL.

Tjoelker, R. L., 2010. 304, Rev. A Frequency and Timing. Tech. rep., DSN Telecommunications Link Design Handbook.

Tobie, G., Grasset, O., Lunine, J. I., Mocquet, A., Sotin, C., 2005. Titan's internal structure inferred from a coupled thermal-orbital model. Icarus 175, 496–502.

Tortora, P., Iess, L., Bordi, J. J., Ekelund, J. E., Roth, D. C., 2004. Precise Cassini Navigation During Solar Conjunctions through Multifrequency Plasma Calibrations. Journal of Guidance, Navigation, and Control 27 (2), 251–257.

Waite, J. H., Lunine, J. I., McKinnon, W. B., Glein, C., Mousis, O., Lewis, W. S., Magee, B., Westlake, J., Nguyen, N., Young, D. T., Brockwell, T., Teolis, B., 2009. Ammonia, radiogenic Ar, organics, and deuterium measured in the plume of Saturn's icy moon Enceladus. Nature 460, 487–490.

Wieczorek, M. A., Phillips, R. J., January 1998. Potential anomalies on a sphere: Applications to the thickness of the lunar crust. Journal of Geophysical Research 103 (E1), 1715–1724.

Wolf, A. A., 2002. Touring the Saturnian System. Space Science Reviews 104, 101–128.

Zannoni, M., Tortora, P., 2012. Numerical Error in interplanetary Orbit Determination Software. Journal of Guidance, Navigation, and Control (submitted).

Zharkov, V. N., Leontjev, V. V., Kozenko, A. V., 1985. Models, Figures, and Gravitational Moments of the Galilean Satellites of Jupiter and Icy Satellites of Saturn. Icarus 61, 92–100.